



Title	Study on the Structure and Composition of Electrochemically Prepared Li-Si Alloys in Organic Solvents
Author(s)	林, 惠文
Citation	北海道大学. 博士(理学) 甲第13365号
Issue Date	2018-09-25
DOI	10.14943/doctoral.k13365
Doc URL	http://hdl.handle.net/2115/75515
Type	theses (doctoral)
File Information	LIN_HUIWEN.pdf



[Instructions for use](#)

**Study on the Structure and Composition of Electrochemically
Prepared Li-Si Alloys in Organic Solvents**

(電気化学的に作製した Li-Si 合金の有機溶媒における構造と組成に関する研究)

Huiwen LIN

Graduate School of Chemical Sciences and Engineering

Hokkaido University



2018

Acknowledgement

At this moment after staying in Japan for four years, I am going to graduate and get my doctoral degree. This will be one of the most important and exciting moments in my life. To all the people who gave me help and guide, I would like to express my greatest thanks.

I would like to gratefully and sincerely thank my supervisors Prof. Kohei Uosaki and Prof. Hidenori Noguchi for their instruction, understanding and patience during my studies, and also for the help they gave me for my dissertation work. I am lucky to have this opportunity to do the PhD work in this group. During the PhD work period, Prof. Uosaki gave me lots of suggestions for scientific researches. Prof. Noguchi not only gave me important instructions in the research work and taught me how to be more skilled on experiment, but also offered a lot of help about my living in Japan. They all taught me how to think independently. Their enthusiasm in science will inspire me in my future work in science research.

I sincerely thank Prof. Toshihiro Kondo for his much suggestions on the Si anode study and on synchrotron XRD measurements. I would like to thank Prof. Kei Murakoshi, Prof. Kazunari Yamaura, Prof. Kazuki Sada, Prof. Shin Mukai and Dr. Akihiro Okamoto as examiners of my dissertation.

I express my grateful thank to Dr. Kentaro Tomita, Dr Nana Aoki and Ms. Makiko Oshida for their help on my experiment. I would like extend my gratitude to previous and present members in my research group: Dr. Takuya Masuda, Dr. Ganesan Elumalai, Dr. Shuo Yang, Dr. Ken Sakauchi, Dr. Kazuhisa Wada, Dr. Shengfu Tong, Dr. Yang Liu, Dr. Ya Zhang, Dr. Yu Sun, Mr. Lei Wang.

Finally, I would like to give my gratitude to my parents, my brothers and sisters for their love, encouragement and support, especially my wife, Yu Su, for her always understanding, encouragement and giving birth to a baby this year.

Huiwen LIN

Tsukuba

August 2018

Contents

Contents	I
Chapter 1 Introduction.....	1
1.1 General Introduction.....	1
1.2 Lithium Based secondary battery	3
1.2.1 Li ion secondary batteries	4
1.2.2 Li-O ₂ secondary batteries.....	6
1.2.3 Li-S secondary batteries.....	7
1.3 Anode Materials for Li Based Secondary Batteries	8
1.3.1 Li metal anode	9
1.3.2 Carbon anodes.....	10
1.3.3 Alloy anodes	11
1.4 Si Anode and Li-Si Alloys.....	13
1.4.1 Alloy phase of Li-Si.....	13
1.4.2 Electrochemistry of Si lithiation	18
1.4.3 Anisotropy expansion of Si lithiation	20
1.5 Electrolytes in Li based secondary batteries and electrolyte for Si Anode.....	21
1.5.1 Electrolyte for Si anode	24
1.6 Objectives and Outline of the Present Thesis	24
References	27
Chapter 2 Experimental.....	33
2.1 Chemicals.....	33
2.2 Electrochemical Measurements and Li-Si Alloys Preparation	33
2.2.1 Hydrogen-terminated Si(111) Electrode Preparation	33
2.2.2 Cyclic Voltammetry Measurements	33
2.2.3 Li-Si Alloys Preparation under Potentiostatic Lithiation	34
2.3 Scanning Electron Microscopy (SEM) Measurements	35
2.4 Energy Dispersive Spectroscopy (EDS) Measurements.....	37

2.4.1 Working Principle of EDS	37
2.4.2 Windowless EDS Measurements	41
2.5 Soft X-ray Emission Spectroscopy (SXES)	42
2.6 In-situ Synchrotron X-ray Diffraction (SXRD) Measurements	44
2.7 X-ray Photoelectron Spectroscopy (XPS) Measurements	46
2.8 Raman Spectroscopy Measurements	47
Reference.....	49
Chapter 3 Investigation of Li distribution in Li-Si alloys by windowless EDS.....	51
3.1 Introduction	51
3.2 Results and discussion.....	52
3.2.1 Electrochemistry of Si(111) lithiation.....	52
3.2.2 Layered Structures of Li-Si alloy.....	53
3.2.3 EDS spectra analysis for Li distribution	55
3.3 Conclusions	63
Reference.....	64
Chapter 4 Lithiation Process Study for Single Crystal Silicon	67
4.1 Introduction	67
4.2 Results and Discussion.....	69
4.2.1 Si(111) Lithiation Process under Potentiostatic Charging	69
4.2.2 In-situ Synchrotron XRD Study for Si Lithiation	75
4.2.3 Diffusion Controlled Instantaneous Nucleation and Growth of Si(111) Lithiation	80
4.3 Conclusions	83
Reference.....	84
Chapter 5 Effects of Hydrogen Fluoride on the Structures and Compositions of Li-Si alloys.....	85
5.1 Introduction	85
5.2 Results and Discussion.....	86
5.2.1 Compositions of Li-Si alloys Prepared in PC and FEC	86
5.2.2 The effects of HF on the structures and compositions of Li-Si alloys	88

5.3 Conclusions	99
Reference.....	100
Chapter 6 Solvent effects on Li distribution within Li-Si alloys.....	103
6.1 Introduction	103
6.2 Results and Discussion.....	104
6.2.1 Electrochemistry of Si(111) Lithiation in Different Solvents	104
6.2.2 Structures and Compositions of Li-Si alloys Prepared in Different Solvents	107
6.2.3 Discussion on the Factors of Solvents that Affect Si(111) lithiation	112
6.3 Conclusions	120
Reference.....	121
Chapter 7 General Conclusion and Future Prospects	123
7.1 General Conclusion	123
7.2 Future Prospects	125

Chapter 1

Introduction

1.1 General Introduction

Air pollution and global warming are two of the greatest threats to human and animal health and society stability.¹ Unrestricted use of traditional fossil fuels such as coal, fossil oil and natural gas is a main cause of air pollution and global warming. Meanwhile traditional fossil fuels are faced with problems such as falling reserves and rising prices and cannot meet the requirements of efficient and economical future society. Many alternatives have been proposed like solar radiation, wind, waves and nuclear power, which represent energy sources that are variable in time and diffused in space.² A big problem for these kinds of energy sources is how to storage energy since they are dependent on the time and space. The most convenient way is to transfer these energy sources to electrical power, and then transfer electrical power to portable chemical energy. Here, secondary batteries can provide the best solution to store portable chemical energy as stationary electricity storage. Once the energy sources are transferred into electrical power, it will be transferred then to portable chemical energy in the secondary batteries. In addition, sustainable development of society need use electric vehicles instead of cars driven by fossil fuels.² And the core power of the electric vehicles lies in the secondary batteries. Due to long term transport requirement, the secondary batteries must provide high energy density. Therefore, the development of the secondary batteries that can store sustainable energy with long term stability and supply enough energy for electric vehicles transport is an important challenge for modern electrochemistry.³

Compared with the several kinds of secondary batteries like Pb-acid and Ni-Cd secondary batteries, Li based secondary batteries play more and more important role in daily life because of their high specific energy density.⁴ It can provide the excellent solution to figure out the energy storage problem. Based on the material used in the anode and cathode, Li based secondary batteries can be Li ion, Li-air (referred to as Li-O₂ since O₂ is the fuel), and Li-S secondary batteries.

The motivation for using Li metal as anode in secondary batteries relied initially on the fact that Li is the most electropositive (-3.04 V versus standard hydrogen electrode) as well as the lightest (equivalent weight $M=6.94 \text{ g mol}^{-1}$, and specific gravity $\rho =0.53 \text{ g cm}^{-3}$) metal, thus facilitating the design of secondary batteries with high output voltage and energy density.⁴ The use of Li metal in a secondary battery was demonstrated in the 1970s.⁵ Over the same period, numerous inorganic compounds were shown to react with Li metal in a reversible way. The concept of electrochemical intercalation and its potential use were clearly defined. In 1972, Whittingham used TiS_2 as the cathode material, Li metal as the anode material to assemble a secondary battery.⁵ TiS_2 was the best cathode material at that time for Li intercalation. Although the cathode material was perfect, this kind of secondary battery didn't work well due to its low cycle life. It was found the Li dendrite formation led to short circuit inside the secondary batteries. Substituting Li metal by an alloy with Al solved the dendrite problem, but alloy electrodes suffered large volume change during the cycle.⁶ To overcome the safety issues brought by Li dendrite formation, several alternative materials were pursued. It was suggested to use a Li intercalation material to substitute the Li metal. Since Li remained its ionic rather than metallic state in Li intercalation material, the dendrite formation problem was solved. A kind of secondary battery was called Li ion secondary batteries by using the Li intercalation material as anode. The Li ion secondary battery had transformed portable electronic device since their introduction by SONY Company in 1991. They used carbonaceous material to substitute Li metal, and successfully built the Li ion secondary battery with long cycle life. The Li ion secondary battery plays more and more significant role in daily life. New generations of the Li ion secondary battery will electrify transport and find use in stationary electricity storage. However, the highest energy density of the Li ion secondary battery is still too low to meet the requirements of electrified transport in the long term.⁷ Advanced secondary batteries with higher energy density must be explored. For this consideration, Li- O_2 and Li-S secondary batteries had attracted more and more interest because of their higher energy density.⁷ The Li- O_2 secondary battery was initially proposed in the 1970s for automotive applications.⁸ Because of the problem of the Li dendrite formation, the Li- O_2 secondary

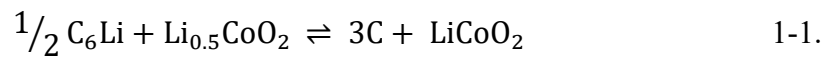
battery didn't attract so much research interest. Until the last few years, the interest in the Li-O₂ secondary battery has grown sharply since it has much higher energy density compared with other types of secondary batteries.^{7, 9-10} The higher energy density in the Li-O₂ secondary battery is pursued urgently to meet long term transport requirement for electrified transportation at this moment, although there remain many problems to figure out. As another type of Li based secondary battery, the Li-S secondary battery has been studied since 1960s.¹¹ There are many formidable problems in Li-S secondary battery to prevent its commercial application. The generation of various soluble polysulphide is the main issue that leads to fast capacity fading in the Li-S secondary battery.¹²⁻¹³ In addition, the insulating nature of S element makes the charge-discharge rate low for the Li-S secondary battery.¹⁴⁻¹⁵ Recently, many important advances have been made, but significant challenges still remain.

In general, the Li based secondary battery consists of Li-compound anode electrode, cathode electrode and Li-salt-containing electrolyte. The properties of each component often determine the ultimate performance of the batteries. Especially when consider the energy density, the capacity of anode and cathode material must be high. The capacity of material describes the ability to store Li. Usually Li metal is considered to be the anode material for the Li based secondary batteries, since it has the highest theoretical capacity. However, the problems for Li metal application still remain.¹⁶ Therefore, other anode materials are put on agenda for research in order to replace Li metal anode.¹⁷⁻²⁰ These anode candidates are expected to transfer into commercial application. In addition, the electrolyte as another significant component shows more and more important role since it determine the performance of the batteries in many cases. Especially in the Li-O₂ and Li-S secondary batteries, the electrolyte must be stable since there are many highly active species to attack the electrolyte salt or solvent during charging and discharging process. In this regard, suitable electrolytes for these secondary batteries must be explored.

1.2 Lithium Based secondary battery

Based on the material used in the anode and cathode, Li based secondary battery can be Li ion Li-O₂, and Li-S secondary batteries. When the anode and cathode electrode are

connected externally, the chemical reactions proceed at both electrodes, and drive the electrons to flow through the external circuit to generate current. The amount of electrical energy that a secondary battery is able to deliver, can be expressed either per unit of weight (Wh kg^{-1}) as specific energy or per unit of volume (Wh L^{-1}) as energy density. The specific energy is a function of the cell potential (V) and capacity (Ah kg^{-1}), both of which are linked directly to the chemistry of the system.⁴ For example for Li ion secondary battery, the specific energy is 387 Wh kg^{-1} when graphite is used as anode and LiCoO_2 is used as cathode. The reaction is⁷



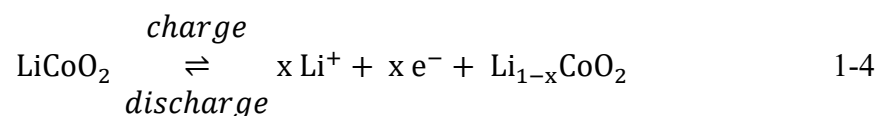
The cell potential is 3.8 V and the capacity is 99 Ah kg^{-1} (for 1 mol reaction 1-1, the charge it delivers is 13.37 Ah, and the mass of C and LiCoO_2 is 0.134 kg. The capacity is equal to the charge divided by the mass). Therefore, the specific energy of 387 Wh kg^{-1} for the Li ion secondary battery is the product of the cell potential of 3.8 V and the capacity of 99 Ah kg^{-1} . The energy density can be obtained in the similar way but per volume is used instead of per mass. The energy density is 1015 Wh L^{-1} for the Li ion secondary battery. In the same way, when consider the reaction 1-2 and 1-3 that happen in the Li- O_2 and Li-S secondary batteries, respectively,



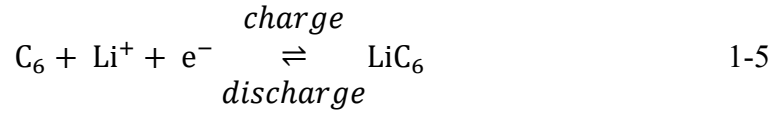
the specific energies of the Li- O_2 and Li-S secondary batteries are 3505 and 2567 Wh kg^{-1} .⁷ The energy densities of the Li- O_2 and Li-S secondary batteries are 3436 and 2199 Wh L^{-1} , respectively.⁷ It is clearly seen the Li- O_2 and Li-S secondary batteries have much higher energy density than Li ion secondary battery.

1.2.1 Li ion secondary batteries

Figure 1-1 illustrates the schematic of the configuration of the Li ion secondary battery. The main electrochemical reactions are reversible Li ion intercalation (lithiation) and de-intercalation (delithiation) between anode and cathode in the Li ion secondary battery. The reaction at the cathode is



During the charging process, LiCoO_2 is oxidized into $\text{Li}_{1-x}\text{CoO}_2$. During the discharging process, $\text{Li}_{1-x}\text{CoO}_2$ is reduced into LiCoO_2 . The redox potential for reaction 1-4 is approximately 4.2 V vs. Li/Li^+ . The reaction is mainly first-order phase transition between LiCoO_2 and $\text{Li}_{0.5}\text{CoO}_2$.²¹ The reaction at the anode is



Li ion will intercalate and de-intercalate into graphite reversibly during the charging and discharging process, respectively. The lithiation-delithiation potential of graphite is approximately 0.2 V vs. Li/Li^+ , which is close to Li deposition-stripping potential.²²

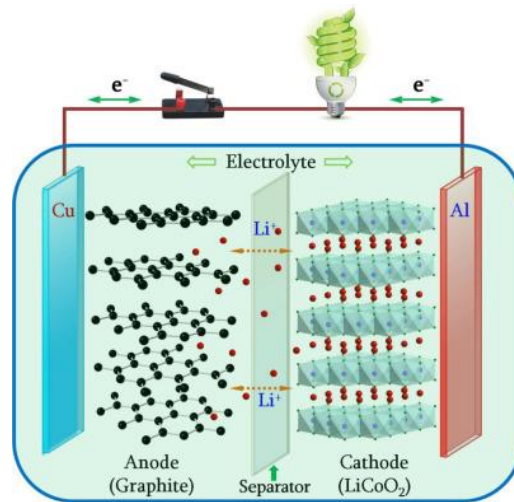


Figure 1-1 Schematic of the configuration of the Li ion secondary battery²³

Theoretically a Li ion secondary battery with an output voltage of approximately 4.0 V could be fabricated considering redox potential of reaction 1-4 and 1-5. In general, the first process in the Li ion secondary battery is always charging process, namely, the delithiation of LiCoO_2 in parallel to the lithiation of graphite. For electrolyte used in Li ion secondary battery, the most popular and conventional is that LiPF_6 solved in alkyl carbonates such as ethylene carbonate (EC) or dimethyl carbonate (DMC) solvents.²⁴ EC has high permittivity and dipole moment so that it can dissolve Li salt easily, but its melting temperature is higher than room temperature, which suggests it will be solid at room temperature and cannot be used as solvent. Since DMC has low melting temperature near 0 °C, it is usually mixed with EC to prepare electrolyte that contains

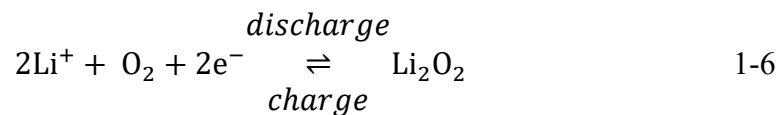
high permittivity of EC and low melting temperature of DMC.

Since the reduction potentials of solution species in polar aprotic Li salt solution are usually positive than graphite lithiation potential, the first charging process would lead to the reduction of solution species to consume irreversible charge.³ Although the reduction cannot be avoid, fortunately most of reduction of the solution species would form a solid-electrolyte-interphase (SEI) on the graphite surface.²⁵ This interphase can serve as a very effective passivation film, and kinetically prevent the further reduction of the solution species. This mechanism enable alkyl carbonate-based electrolyte can be used in Li ion batteries.

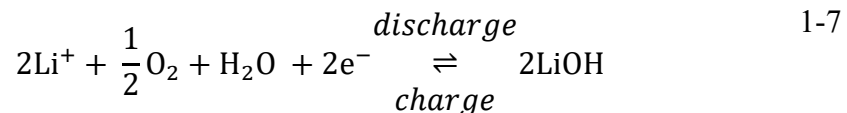
1.2.2 Li-O₂ secondary batteries

The Li-O₂ secondary battery based on non-aqueous and aqueous electrolytes are shown in Figure 1-2. Generally speaking, the Li-O₂ secondary battery based on aqueous electrolyte is more complicated than that based on non-aqueous electrolyte because of the strong reactivity of Li metal with water. For both cases, Li metal is used as the anode. It is stripped and oxidized to Li⁺ ion into electrolyte on discharging. This process is reversed on charging.⁹

In non-aqueous Li-O₂ batteries, O₂ is the cathode material and reduced to form Li₂O₂ along with Li⁺ ion from the electrolyte during discharging process, which is then decomposed during charging process.²⁶ The reaction is written



In aqueous Li-O₂ batteries, O₂ is reduced to form LiOH at the cathode during discharging process according to the reaction²⁷



Although both involve O₂ reduction on discharging for non-aqueous and aqueous system, there are important differences, especially relating to the reactions at the cathode and the role of the electrolyte.⁷

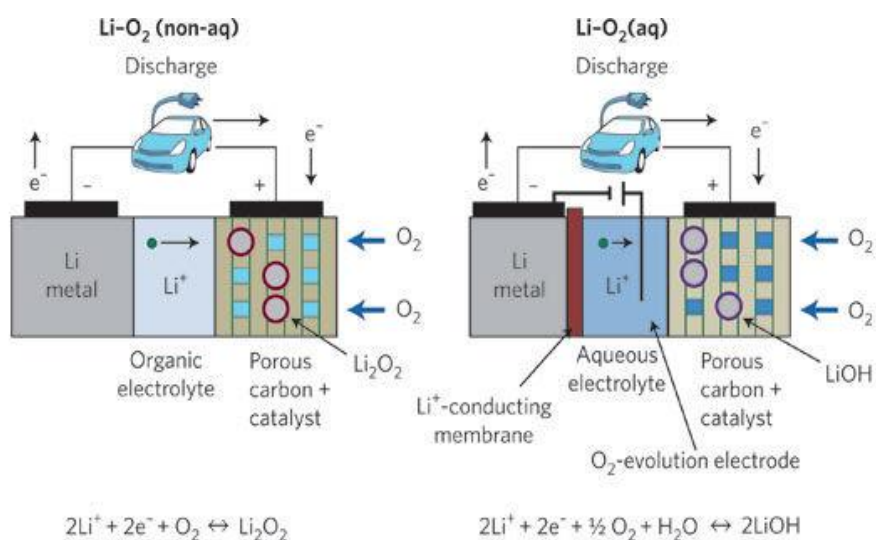
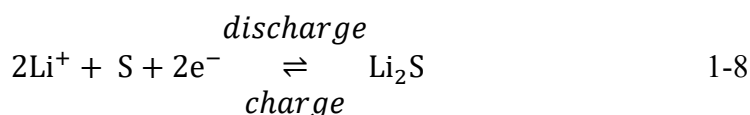


Figure 1-2 Schematic of the configuration of the non-aqueous and aqueous Li-O₂ secondary batteries⁷

The electrolyte for the Li-O₂ secondary batteries is a key component and one of the main challenges at present. Since the alkyl carbonate used commonly in the Li ion secondary battery is unstable and decomposed by the reduced species of oxygen like O₂^{•-}, it is not suitable to be applied in the Li-O₂ secondary batteries.²⁸ Therefore an outstanding electrolyte must be explored to be stable to the reduced species of O₂ and the discharging product of Li₂O₂ or LiOH. Other properties like ionic conductivity, O₂ solubility and diffusion need to be also satisfied for better battery performance.

1.2.3 Li-S secondary batteries

The Li-S secondary battery is shown in Figure 1-3. Similar with the Li-O₂ battery, the anode is Li metal which strips and deposits over discharging and charging process. But the cathode reaction is different. S is reduced at the cathode to form various polysulphide during discharging process. The ultimate discharging product is mainly Li₂S, for which the reaction is ²⁹



The Li-S secondary battery is attractive because of its high theoretical energy density. In addition, the element S is the naturally abundant and cheap. However, there are still several problems remained in the Li-S secondary battery even after decades of research.

One of the severe problems is fast capacity fading due to the generation of various soluble polysulphide, which gives rise to a shuttle mechanism.³⁰ The shuttle mechanism arises because the soluble polysulphide that are formed at the cathode are transported to the anode where they are reduced to lower polysulphide. The lower polysulphide are then transported back to the cathode, where they become re-oxidized and then return to the anode.

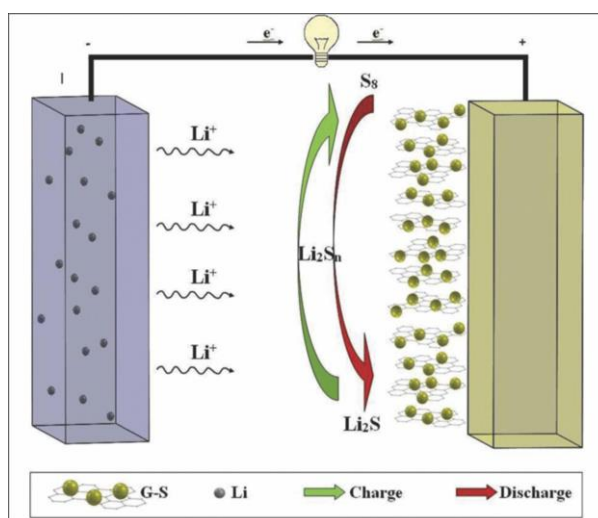


Figure 1-3 Schematic of the configuration of the Li-S secondary battery³¹

Even though Li based secondary battery could provide high energy density as described above for Li ion, Li-O₂ and Li-S systems, there remain many issues to figure out for each system. Most fundamentally, the research is needed to make clear the reaction mechanism on anode, cathode and also in electrolyte. And practically, the material synthesis and design should be put on agenda for a better battery performance to reach the theoretical limit of each battery system.

1.3 Anode Materials for Li Based Secondary Batteries

The anode is one of the most basic components of a secondary battery that the cathodic reaction happens during charging process. For the Li-O₂ and Li-S secondary batteries, the anode material is Li metal. For the Li ion secondary battery, the most conventional anode material is graphite. There are many other forms of anode materials such as alloys, metal oxides, metal sulfides and metal nitrides for Li based secondary batteries. Since their electrochemical properties are different, they possess specific

advantages and disadvantages.

As a superior anode material in the Li based secondary batteries, it must have high volumetric and specific energy capacities, superior reversibility and low charging and discharging potential near Li deposition and stripping potential. In addition to these basic battery property requirements, environment friendliness and safety issue must be always put on the agenda. As long as any of the above requirements does not fit, the application of the anode material will encounter many difficulties.³²

1.3.1 Li metal anode

Li metal is the primitive anode material applied in Li based secondary batteries. It is an ideal anode material due to its extremely high theoretical specific capacity (3860 mA h g⁻¹), and the lowest negative electrochemical potential of -3.04 V vs. standard hydrogen electrode,³³ thus facilitating the design of secondary batteries with high energy density and output voltage. However, it had been studied for several decades but has not yet been commercialized. There are two main barriers for the commercialization of the secondary batteries using Li metal as anode material.³² One is the Li metal dendrite formation and growth after long repeated charging and discharging processes. The formation of Li metal dendrite might impale the separator and reach the cathode, leading to internal short circuits to cause safety hazards. Another is the short cycle life due to its low columbic efficiency, which is defined as the ratio of charge amount of discharging and charging processes in one cycle. Li exposes to the electrolyte repeatedly during the charging and discharging process, and cause more severe electrolyte decomposition. These two barriers consequently prevent the commercialization of Li anode.

Since high energy density secondary batteries such as the Li-S and Li-O₂ secondary batteries are pursued urgently for next generation secondary batteries for electrical vehicles, Li metal anode has attracted significant research interest again in recent year to be used in these batteries.³² Most of studies remain on Li dendrite formation mechanism. Various efforts focus on the strategies to prevent the dendrite formation. Basically there is solid electrolyte interphase (SEI) formation on Li surface during Li deposition process, since reduction potentials for most electrolyte components based on organic solvents are more positive than Li deposition potential.³⁴ This SEI layer could

prevent the further electrolyte decomposition kinetically. However, it is difficult to achieve effective SEI layer since big change of Li metal morphology during repeated deposition and stripping. Some valid ways are fabricating artificial SEI layer on Li surface or a separator to suppress Li dendrite formation and penetration.³⁵ But these approaches are unable to prevent Li dendrite growth after long term cycle. Li dendrite can be cracked to lose the contact with the electrode and will not act as active material again. For the future research and development, the Li stripping and deposition mechanism should be studied more deeply for the dendrite formation.³² The commercialization of Li metal anode still takes a long time to achieve.

1.3.2 Carbon anodes

Carbon materials can be classified into soft carbon (graphitic carbon), hard carbon (disordered carbon) and nanostructured carbon.³⁶ Among these different kinds of carbon, natural or artificial graphite has obvious advantages as anode material for Li intercalation because of its layer structure. It has high specific and volumetric capacity, low lithiation and delithiation potential near Li stripping and depositing potential.²² It also has good rate capability, low irreversible capacity, good electronic conductivity and long cycle life for battery performance. The commercialization of the Li ion secondary battery started from 1990s when SONY Company announced the application of graphite anode to replace Li metal anode. As mentioned above, Li metal anode has severe dendrite formation, which leads to safety hazards. The graphite used as anode material improves the cycle life and safety of Li based secondary battery. The volume expansion is only about 10% after the graphite was lithiated to LiC_6 . Because of the small structure change with low expansion after lithiation, the reversibility is very high so that the Li ion secondary battery has very good cycle life. Basically, similar to Li metal anode case, there is also SEI formation due to the reduction of electrolyte components because the lithiation of graphite is near 0.2 V vs. Li/Li^+ . Since graphite has small structure change, the SEI layer can keep stable even after lithiation. The stability of a SEI layer is significant for the battery performance. And this is also one of the reasons why the Li ion battery could have a long cycle life.

Using disordered carbon like single graphene sheets to replace graphite has been

considered to increase the anode capacity, since single graphene sheets are expected to adsorb Li ion on their both sheet sides. Matsumura et al.³⁷ proposed that in disordered carbon, Li ion are not only intercalated between graphitic layers but also adsorbed at the edge and onto the surface of the graphene layer. Therefore, the capacity of disordered carbon materials can go beyond the theoretical capacity of graphite (378 mAh g^{-1}) up to about 450 mAh g^{-1} .³⁶ In addition to the higher capacity compared to the graphite, the high specific surface and good electronic conductivity of graphene make it has good rate capability, that is, high current density can be obtained. However, the fabrication cost for graphene is higher than that for graphite. The easy and cheap fabrication method for graphene must be explored in the future.

Carbon nanostructures such as nanotubes, nanoparticles and nanosheets have been proposed as potential substitute for traditional graphite for intercalation. They could have higher capacity than graphite. For example, the nanotubes have interstitial sites including inter shell van der Waals spaces, inter tube channel and inner cores for Li intercalation.³⁸⁻³⁹ In other words, there are more sites for Li intercalation in carbon nanostructures. However, although the higher capacity could be obtained, the excessive irreversible charges and the technological limits towards industrialization have to be solved. The excessive irreversible charges are due to the high surface area of the nanostructures, which will cause more electrolyte decomposition to form SEI on the surface. To figure out these problems, development of new electrolytes seems to be necessary to reduce the irreversible capacity by reduce the possibility of electrolyte decomposition or form effective SEI on the surface.

Besides the advantage of carbon used as anode materials for the Li ion secondary battery, there still remain some issues for graphite anode to figure out. One is the limited theoretical capacity. As the urgent need of next generation secondary batteries with higher energy density, other types of anode such as alloy anode need to be explored as soon as possible, including the primitive anode material Li metal currently.

1.3.3 Alloy anodes

Alloy anode could provide higher specific and volumetric capacities compared with carbon anode.⁴⁰ Since the energy density of carbon anode based Li ion secondary

batteries almost reach their theoretical limit with little space to improve, people show more interest to find an anode with higher energy density like alloy anode.⁴¹

The elements, that can alloy with Li and be used as potential anode materials, include the alkaline earth metals such as Mg and Ca, the transition metals such as Zn and Ag, p-block elements such as Al and Si. For practical consideration, the elements must be lowly toxic, cheap and have alloying potential close to Li deposition and stripping potential. The properties of lowly toxic and cheap are based on the environmental consideration, since one of the main purposes of the secondary batteries is to reduce the air pollution. The alloying potential close to Li deposition and stripping potential is beneficial for the fabrication of a secondary battery with high output voltage.

Figure 1-4 shows the elements that can be used as alloy anode candidates along with graphite anode. Figure 1-4a shows the volumetric capacities of the elements calculated at their state of full lithiation. Figure 1-4b shows the gravimetric capacity.⁴⁰ Obviously, most of alloy anode could provide double the volumetric capacity of graphite shown in Figure 1-4a. And most of the alloy anodes have higher gravimetric capacity than graphite shown in Figure 1-4b. It is expected the energy density will increase significantly for Li based secondary batteries if alloy anodes are applied. In addition, most of these alloy materials are abundant in production like Si and Al, industrial production of which is quite mature.

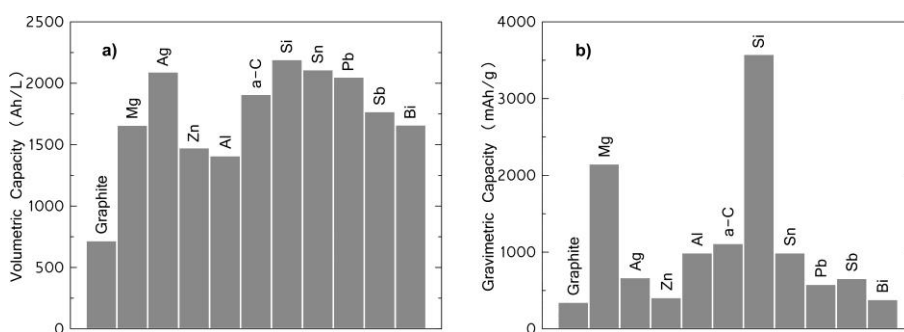


Figure 1-4 (a) Volumetric capacities calculated at the state of full lithiation and (b) gravimetric capacities of selected elements.⁴⁰

However, the secondary batteries using alloy as anode can have very high irreversible capacities because of the large volume expansion and shrinkage during the

lithiation and delithiation.¹⁷ This big volume change will cause the fracture of active material and disconnection between active material and current collector. Much effort needs to be made to figure out volume expansion problem.

1.4 Si Anode and Li-Si Alloys

Among the large number of investigated high specific capacity anode materials, alloy anode electrodes have significant potential.⁴⁰ As is shown in Figure 1-4, Si is a promising candidate with the highest volumetric and gravimetric capacity (2200 Ah/L and 3600 mAh/g) when alloying with lithium to form $\text{Li}_{15}\text{Si}_4$. Meanwhile it possesses a lower discharge platform (ca. 0.4 V vs. Li/Li^+). On the other hand, it is non-toxic and has rich natural abundance. These advantages impel people to study Si anode as next generation anode material. However, Si is accompanied by a very large volume expansion (280% for $\text{Li}_{15}\text{Si}_4$ alloy phase) during lithium intercalation. Cyclic volume expansion and shrinkage during lithiation and delithiation lead to pulverization of Si particles and electrical disconnection from the current collector, which is one of the main factors decreasing the cycle life of Si anode based secondary battery. In addition to the issue of volume expansion, the alloy structure, components and lithiation mechanism are also important to study for their significance to the battery performance like battery capacity, cycle life and safety.

1.4.1 Alloy phase of Li-Si

Figure 1-5 shows the phase diagram of Li alloying with Si.⁴² Theoretically, Si alloying with lithium will produce various forms of alloy (LiSi , $\text{Li}_{12}\text{Si}_7$, Li_7Si_3 , $\text{Li}_{13}\text{Si}_4$, and $\text{Li}_{22}\text{Si}_5$). This is also expected to occur during the electrochemical deposition process. Li-Si alloy are understood to be zintl-like phases,⁴³ in which if the Si atom octet is not fully filled by electron transfer from Li, there still exist Si-Si bonds. However, in most of the Li-Si alloy phase the Si atoms do not completely strip all the electron of the Li atoms, in other words, electrons is partially transferred to Si atoms from Li atoms.⁴⁴ Only in the LiSi phase, each Si atom can fill the octet by stripping one electron from the Li atom.

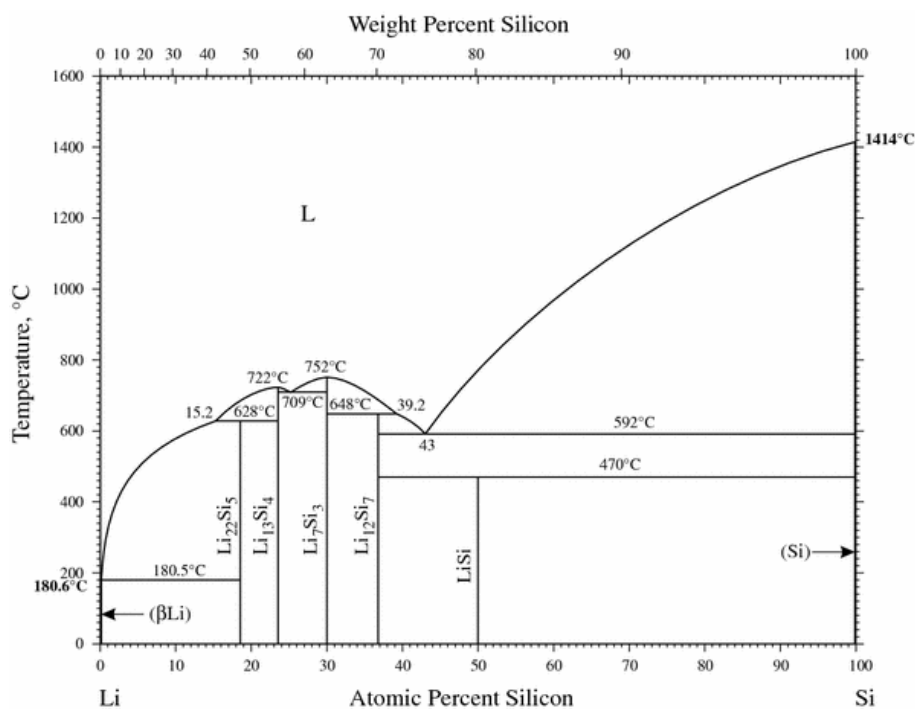


Figure 1-5 Phase diagram of Li-Si⁴²

The Li-Si alloy phase diagram in Figure 1-5 contains most alloying phases; however Obrovac et al⁴¹ found a new Li-Si alloy phase at full lithiation state, Li₁₅Si₄, which is most likely to be the most lithiated phase existing after Si lithiation during electrochemical process at room temperature.⁴¹ Thus the family of Li-Si alloys are determined more completely.

⁴⁴Figure 1-6 shows the primitive cells of each alloy phase with cells of Si and Li.⁴⁴ Basically it is clear that the interatomic distance between Si-Si increases as the degree of lithium alloying progresses because of more Li atom insertion. The structure of Si-Si bonds shows gradual collapse as the lithium alloying degree progress. The Li₁₂Si₇ alloy phase has striking five-member rings, whereas the Li₇Si₃ alloy phase has only Si dumbbells. In the Li₁₃Si₄ alloy phase, half of the Si atoms are Si dumbbells and the other half is isolated by Li atoms. The Li₁₅Si₄ phase is the first alloy phase in which all Si atoms are surrounded by Li atoms. Table 1-1 lists the crystalline parameters for all the Li-Si alloys. As is seen, the density of Si-Li alloys decreased as lithium alloying degree increase resulting in big volume expansion.

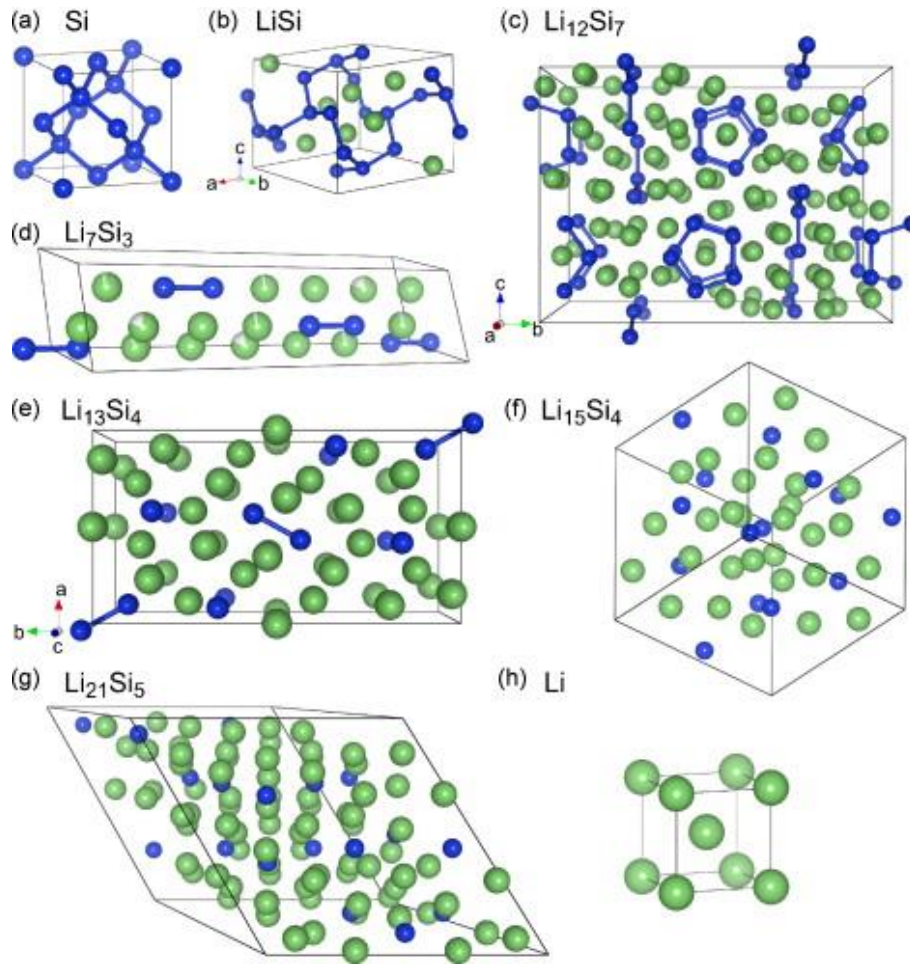


Figure 1-6 The primitive cells of the crystalline Li-Si structures⁴⁴

Table1-1 Crystalline parameter for all the Li-Si alloys

Phase	x in Li_xSi	Space group	Cell	Lattice constant(\AA)	Density (g/cm ³)
⁴⁵ Si	0	Fd $\bar{3}$ m	Cubic	a=b=c=5.43	2.33
⁴⁶ LiSi	1	I41/a	Tetragonal	a=b=9.34 c=5.76	1.85
⁴⁷ Li ₁₂ Si ₇	1.71	Pnma	Orthorhombic	a=8.56 b=19.70 c=14.30	1.53
⁴⁴ Li ₇ Si ₃	2.33	P3 ₂ 12	Trigonal	a=7.63 c=18.01	1.35
⁴⁴ Li ₁₃ Si ₄	3.25	Pbam	Orthorhombic	a=7.97 b=15.14 c=4.44	1.25
⁴⁸ Li ₁₅ Si ₄	3.75	I43D	Cubic	a=b=c=10.6	1.21

⁴⁹ Li ₂₂ Si ₅	4.4	F23	Cubic	a=b=c=18.75	1.18
⁵⁰ Li	-	Im3m	Cubic	a=b=c=3.51	0.54

The Li-Si alloy structures and compositions have been widely studied because of their significance with respect to battery characteristics such as energy density and cycle life. X-ray diffraction (XRD) is the most applied method to identify the structure and composition of Li-Si alloys. Obrovac studied structural changes in Si electrochemically lithiated process at room temperature by XRD, and determined that the Li₁₅Si₄ phase crystallized from highly lithiated amorphous Si.⁴¹ Thereafter, several groups reported crystalline Li₁₅Si₄ formation from amorphous highly lithiated Si.⁵¹⁻⁵⁸ However there are still some controversies about if there is crystalline Li₁₅Si₄ formation as others have reported only amorphous phases.⁵⁹⁻⁶⁰ The controversies mainly stem from experimental procedure such lithiation potential setup and lithiation degree control, which may lead to no Li₁₅Si₄ crystalline phase formation. In some cases, the amounts of Li₁₅Si₄ crystalline phase is not enough to be detected by normal XRD since the reflect intensity is not enough high. Synchrotron X-ray diffraction (SXR) is a powerful method to detect very weak diffraction peaks with high sensitivity. Therefore, the observation of crystalline Li-Si alloy phases is dependent on the experimental conditions, the instrument sensitivity, and the amount of crystalline phase.

In addition to the powerful structural analysis for electrochemically formed Li-Si alloy by XRD and SXR, in-situ transmission electron microscopy (TEM) also shows better structure and composition analysis with atomic resolution. In situ TEM allows real-time studies of lithiation and delithiation behavior of individual Si nanowires or nanoparticles.^{52, 56, 61-62} In most works it is demonstrated that there exists a sharp phase between the crystalline Si and amorphous Si-Li alloy, and finally the crystalline Li₁₅Si₄ phase would form after the lithium concentration of amorphous Li_xSi reach a x value of 3.75 determined by electron diffraction pattern.

Besides XRD and TEM for structural and composition analysis, X-ray photoelectron spectroscopy (XPS), nuclear magnetic resonance (NMR) spectroscopy

and Raman spectrum are applied to analyze the electronic state of electrochemically formed Li-Si alloy. XPS can determine Si electronic state by observing the energy shift of Si 2p peak after lithiation. Especially, this technique is powerful to investigate the solid electrolyte interface (SEI) formed by decomposition of electrolyte which is well known to affect the battery performance.⁶³⁻⁶⁹ Key⁷⁰ apply real time NMR to investigate the structure of the amorphous phase, in which the lithiation of Si form Si-Si clusters at first and then broken apart at the end of the first discharge to form isolated Si ions and eventually the crystalline phase. It is also found the crystalline phase can accommodate a small excess of Li to become extremely reactive in the electrolyte which might cause self-discharge leading to the loss of the battery capacity. In addition, Raman spectrum analysis clearly shows the Si-Si bond cleavage during the lithiation according to the observation of Raman scattering intensity decrease at the Raman shift of Si-Si vibration mode.

In addition to above technique to determine the structure and composition of Li-Si alloy, soft X-ray emission spectroscopy (SXES) is also a powerful method for investigating Li-Si alloys. A combination of SXES and scanning electron microscopy (SEM) can reveal the valence band (VB) structure of Li-Si alloys by excitation of inner shell electrons and emission of soft X-rays when electrons are transferred from the VB to the inner orbital.⁷¹⁻⁷² SXES has been successfully applied by Aoki et al. to investigate the composition and electronic states of Li_xSi alloys by comparison of the experimental SXES results and the calculated density of states (DOS).⁷³ The results revealed a Li-Si alloy layer structure for electrochemically lithiated Si(111) single crystals.

However, it is difficult for SXES to identify nanostructures due to its low spatial resolution, because the electron beam size is approximately one micron. Windowless energy dispersive spectroscopy (EDS) can be used to determine nanostructures with high spatial resolution near 10 nm and sensitivity to light elements including Li.⁷⁴ Conventional EDS has Be metal window to prevent the detection of soft X-rays below 150 eV because of the absorption of Be metal window. Windowless operation with a very short working distance and new electronic devices provide improved sensitivity for the detection of low energy X-rays, including Li K_α and Si $\text{L}_{2,3}$ emission. These features

enable measurement of Li K_{α} , Si $L_{2,3}$ and Si K_{α} lines simultaneously, while capturing information on the composition and electronic states. A combination of high energy resolution analysis by SXES and high spatial resolution analysis by windowless EDS could be used to examine the structure, composition and electronic state changes during lithiation of single crystal Si, and thereby reveal the mechanism of Si lithiation.

1.4.2 Electrochemistry of Si lithiation

There should be several charge-discharge platforms for Si electrochemical lithiation process because of the existence of its alloy phases theoretically according to the equilibrium phase diagram. However, this is not the case when Si electrochemical lithiation is conducted at room temperature. It is found that these kind of charge-discharge platforms only exist at high temperature such as 450 °C which is shown in Figure 1-7.⁷⁵ The lithiation and delithiation process at high temperature presents four stable voltage platforms, corresponding to each individual phase transition process among Si, $Li_{12}Si_7$, Li_7Si_3 , $Li_{13}Si_4$ and $Li_{22}Si_5$. It must be reminded that there is no $Li_{15}Si_4$ alloy phase electrochemical formation at high temperature. However, at room temperature the first lithiation curve of Si does not show multiple voltage platforms, but instead exhibits a lower long plateau which corresponds to the crystalline silicon transformation into an amorphous form of Li-Si alloy. A metastable crystalline $Li_{15}Si_4$ phase has been determined when the lithiation progress deeply at room temperature^{52, 52}. The crystalline $Li_{15}Si_4$ phase can only be obtained by Si electrochemical lithiation at room temperature because it is unstable above 250 °C and will disproportionate into other crystalline phases,⁷⁶ which is one reason that why there is no crystalline $Li_{15}Si_4$ alloy phase at high temperature. Therefore, it is not generally shown in the equilibrium phase diagram in Figure 1-5. The study of crystalline $Li_{15}Si_4$ alloy is of significance since it is relative to the properties of Si anode based secondary batteries like capacity and cycle life at room temperature. On the other hand, crystalline phases are generally considered to be detrimental to battery performance in alloy negative electrodes, and should therefore be attempted to avoid their formation.⁷⁷

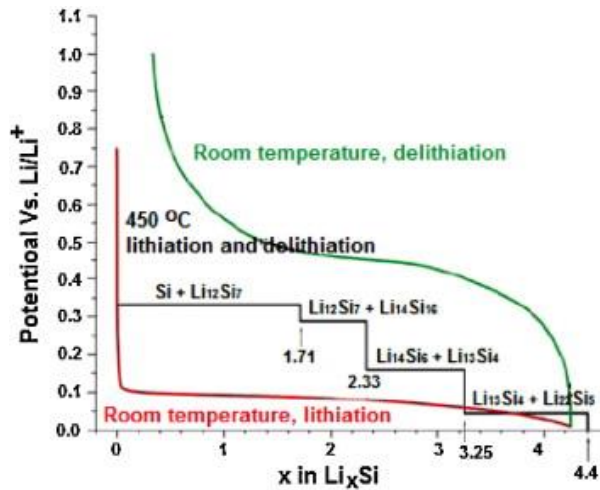


Figure 1-7 Si electrochemical lithiation and delithiation curve at room temperature (red and green line) and high temperature of 450 °C (black line)⁷⁵

The formation of $\text{Li}_{21}\text{Si}_5$ and $\text{Li}_{22}\text{Si}_5$ alloy phases also show difference at room temperature and high temperature. The Si electrochemical lithiation experiments at high temperature showed the presence of a precisely composed phase of $\text{Li}_{22}\text{Si}_5$.⁷⁸ It is speculated that the stability of $\text{Li}_{21}\text{Si}_5$ and $\text{Li}_{22}\text{Si}_5$ phase may be temperature dependent.⁴⁴ Figure 1-8 shows the $\text{Li}_{21}\text{Si}_5$ phase is more stable than $\text{Li}_{22}\text{Si}_5$ phase at room temperature. And basically, crystalline $\text{Li}_{15}\text{Si}_4$ has similar formation energy compare with $\text{Li}_{21}\text{Si}_5$ phase, which indicates the experimental observation that crystalline $\text{Li}_{15}\text{Si}_4$ will form after lithiation is reasonable according to the calculation results.

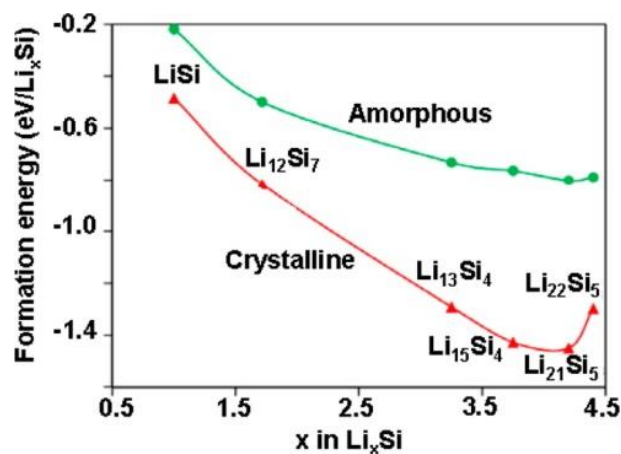


Figure 1-8 Calculated formation energy of Li_xSi in crystalline and amorphous forms at room temperature⁵²

1.4.3 Anisotropy expansion of Si lithiation

The anisotropic volume expansion behavior and dynamics of Si lithiation have been investigated experimentally and theoretically.^{53, 79-84} As described above, the electrochemical lithiation of Si at room temperature results in an amorphous phase at first and finally transfer into $c\text{-Li}_{15}\text{Si}_4$, which suggested that Si lithiation is a two-phase reaction in which there exist a reaction front between crystalline Si and amorphous Li-Si alloy. Goldman et al. showed clear anisotropic volume expansion along the Si $\langle 110 \rangle$ crystalline orientation.⁸⁰ In addition, Lee et al. used etched Si wafer with nano-pillars and reported that the anisotropic volume expansion occurs preferentially along the crystalline facet (110) which is shown clearly in Figure 1-9.⁸¹ The circular cross sections of nanopillars with different axial orientations expand into different shape by a main expansion direction $\langle 110 \rangle$. It is suggested that Li inserted the crystalline Si through $\langle 110 \rangle$ ion channels which causes the preferential volume expansion along this direction and induces the collapse of (111) planes by breaking Si-Si bonds. If lithiation is controlled by the anisotropic ion insertion rate as opposed to the diffusion through the lithiated phase, anisotropic expansion may occur.⁸⁵⁻⁸⁶ Anisotropic Li insertion rate will cause the anisotropic stress inside the electrodes and finally lead to bad cracks. It is suggested to decrease the internal stress caused by anisotropic expansion by designing Si film with preferred crystal orientation. It is of significance to study the Li insertion anisotropy in Si single crystal to make clear how Li insert Si to form Li-Si alloys.

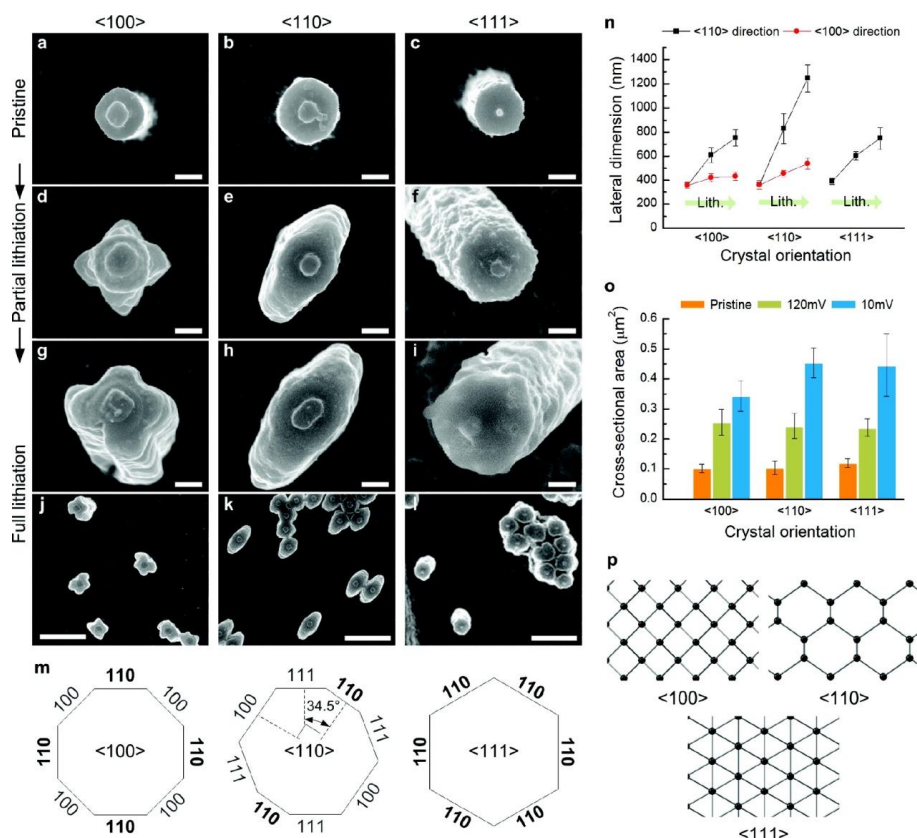


Figure 1-9 Anisotropic lateral expansions of crystalline Si nanopillars with three different axial orientations ($\langle 100 \rangle$, $\langle 110 \rangle$ and $\langle 111 \rangle$) upon lithiation⁸¹

1.5 Electrolytes in Li based secondary batteries and electrolyte for Si Anode

The great volume expansion hinders the further commercial application of Si anode because it makes the stable battery cycling very difficult to achieve.⁸² And those severe capacity fading mechanisms are most relative to electrolyte. First, the continuous expansion and shrinkage of the Si electrode material makes the electrolyte decomposition film thicker, decreasing the electrical conductivity of Si electrode and increasing the irreversible capacity.⁸⁷⁻⁸⁸ Commercial electrolytes in Li ion batteries are commonly alkyl carbonate solvent, when the potential is below 1.3 V vs Li/Li⁺ the electrolyte decomposition will occur to form a layer of poor electron conductivity while good ion conductivity of the surface film. This film is well known as the solid electrolyte interface (SEI). By isolating the anode and electrolyte, SEI can prevent the further decomposition of the electrolyte kinetically. However, because of expansion and shrinkage of Si in the charge and discharge process, SEI film can be broken and the surface of Si electrode exposes to the electrolyte again, leading the further electrolyte

decomposition to reduce the battery capacity. Second, the volume expansion and shrinkage of Si can cause breakage and pulverization of Si particles, which is particularly pronounced for larger size Si particles.⁶¹ Cracks can cause Si new surfaces to contact the electrolyte resulting in further electrolyte decomposition and loss of electrical contact between the particles and the ability to conduct electrons. Generally speaking, it is expected to have better performance for Si anode based secondary battery if the electrolyte is stable with little decomposition or to form a stable SEI on Si surface.

Electrolytes were generally considered as a key element that affects or even determines the battery performance in terms of electrochemical reversibility, cycle life, rate capability and columbic efficiency. Since electrolytes are different for the Li ion, Li-O₂ and Li-S secondary batteries, the electrolyte effects on Si lithiation should be studied more deeply.⁸⁹⁻⁹² Especially the use of Si anode in Li-O₂ and Li-S secondary batteries can play the high capacity of Si since the cathode is O₂ and S that can have very high capacity. The increasing interest engages people to study more about fundamental of Si lithiation in Li-O₂ and Li-S secondary batteries when the electrolytes are changed.

The electrolyte used in the Li ion secondary batteries contains Li salt, solvent and some solved addition. Li salt is dissolved in nonaqueous solvent through ion-solvent interaction. Electrolyte solvents must be enough polar to dissolve the Li salt. In the Li ion secondary battery, the electrolyte solvents were mainly selected from the organic carbonate, among which ethylene carbonate (EC) became the indispensable for a number of properties such as high dielectric coefficient. Dimethyl carbonate (DMC) and propylene carbonate (PC) are also used as co-solvent. Carbonate ester were used as electrolyte solvents due to their stability to anodic decomposition, but their cathodic stability is low and make them decompose on anode during the anode lithiation process. However, a SEI layer forms between anode surface and the electrolyte. This SEI layer prevent the further decomposition of carbonate ester and make carbonate ester suitable used in the Li ion secondary battery. And right now, the most of the efforts are focusing on achieving a better electrochemical performance of this layer, such as more Li conductivity, less electron conductivity and uniform formation on anode surface.

An ideal electrolyte for Li-O₂ secondary batteries is expected to possess high O₂

solubility and mobility, high chemical stability toward LiO_2 and Li_2O_2 , tolerance against Li metal anode growth or Si anode expansion. The most studies recently focused on the suitability of aprotic solvent used as nonaqueous electrolyte solvent because they may react with the peroxide or superoxide. The commercially used electrolyte in the Li ion secondary battery is based on alkyl carbonate solvents such as DMC, EC and PC. And this is also tested as the default solvent in Li- O_2 secondary batteries. However, they can be decomposed by the highly reactive intermediates of reduced O_2 , such as superoxide radical O_2^- . O_2^- would attack carbonate molecules as a strong nucleophile, initiating their reductive breakdown into semi carbonates via a carbonate peroxide intermediate.²⁸ This makes carbonate not suitable to be used in Li- O_2 secondary batteries. Compared with the instability of carbonate solvents, linear ethers such as tetraethyl glycol dimethyl ether (TEGDME) or triglyme can serve as better solvents than carbonates.⁹³ One of the most important reason is that they favor the formation of Li_2O_2 as the main discharged product. However, they still can react with O_2^- during the long-term cycling. For a nonconventional electrolyte solvent, dimethyl sulfoxide (DMSO) was the most reported to be stable in Li- O_2 secondary batteries.⁹⁴ The formation of Li_2O_2 was favored in DMSO, while the kinetics of its reoxidation was much facilitated. High capacity can remain even after long term charge-discharge cycle. And this is attributed to the stabilization of superoxide radical species O_2^- by solvated Li^+ in DMSO. Since the conventional electrolyte carbonate is unstable in Li- O_2 secondary batteries, the effect of solvents on Si lithiation need to be considered further when Si anode is used.

In Li-S secondary battery, a series of intermediates (S_8^{2-} , S_6^{2-} , S_4^{2-} , S_3^{2-} , and S_2^{2-}) often form corresponding to varying stages of incomplete reductions of S. These intermediates were not of particularly high reactivity toward solvent molecular unlike that in the Li- O_2 secondary battery, partially due to the better charge-delocalization in these polyatomic as well as their higher solubility in organic media.⁹⁵ However, these intermediates still can attack alkyl carbonate solvents, and their solubility in organic solvent induced a shuttling mechanism, leading severe capacity decrease or battery failure. ⁹⁵Ethers were preferred over carbonates as electrolyte solvents for the Li-S secondary battery.²⁹ The parasitic reactions occur seriously between polysulfide species

and carbonates. However, acyclic and cyclic ether like dimethyl ether (DME) or tetraethyl glycol dimethyl ether (TEGDME), can be more stable for these intermediates.

As described above, the electrolyte performance based on different solvents are dependent on the type of Li based secondary batteries. For example, in Li-O₂ secondary batteries, the solvents DMSO was stable than TEGDME and alkyl carbonate. And TEGDME shows better performance than alkyl carbonate. If Si anode was used in these Li based secondary batteries, the electrolyte effects on Si lithiation should be determined. Further study need to be conducted for a better choice of electrolyte, especially the solvent choice such as more stable solvent.

1.5.1 Electrolyte for Si anode

When Si anode is used as anode, the conventional electrolyte using EC or DMC as solvent seemed have bad performance on cycle life and capacity. Some reports had determined the fluoroethylene carbonate (FEC) and vinyl carbonate (VC) can improve the Si anode performance like cycle life and capacity significantly. Usually FEC and VC were used as co solvent or addition, which can suppress the continuous SEI formation by forming -Si-F and LiF species which have strong binding energy. Moreover, FEC forms polymeric species by generating HF to form VC and polymerizes to form a passivation film. However, the beneficial effects of FEC or VC need to be understood further. Since FEC or VC is expensive solvents and not the ultimate choice, these studies will help to explore more solvent system to be used.

1.6 Objectives and Outline of the Present Thesis

The objective of this thesis is to determine the structures and compositions of Li-Si alloys prepared in different solvents using scanning electron microscopy (SEM), windowless energy dispersive spectroscopy (EDS) and soft X-ray emission spectroscopy (SXES). The application of windowless EDS to determine the Li distribution in Li-Si alloys was declared. And it was used to study the Si lithiation process. The structures and compositions of the Li-Si alloys prepared in different solvents were mainly studied and discussed. By using these techniques, the solvent effects on the Si lithiation were discussed and understood.

In Chapter 1, the background of the Li based secondary batteries, the anode

materials and the Si anode are given. The structures and compositions of Li-Si alloys after Si electrochemical lithiation are briefly reviewed. The electrolytes used in Li based secondary battery are also reviewed for Si anode.

In Chapter 2, the experimental details are given, including the materials, electrochemical measurements, and Li-Si alloys preparation and characterization techniques.

In Chapter 3, the composition of the Li-Si alloy was studied using the high-energy resolution analysis of SXES and high spatial resolution analysis of windowless EDS. The Li K_{α} , Si $L_{2,3}$ and Si K_{α} intensity changes determined by windowless EDS were analyzed to obtain the specific thicknesses and composition for the Li-Si alloy layers. The Li-Si alloy prepared after a charge density of $1000 \text{ mC}\cdot\text{cm}^{-2}$ consist of an approximately $1.0 \mu\text{m}$ thick crystalline $\text{Li}_{15}\text{Si}_4$ alloy layer, a $1.5 \mu\text{m}$ thick amorphous $\text{Li}_{13}\text{Si}_4$ alloy layer, and a $2.2 \mu\text{m}$ thick Li diffused Li_xSi alloy layer. The Li distribution in diffused Li_xSi alloy layer was determined for the first time by windowless EDS measurements.

In Chapter 4, the Si lithiation was studied. Five Li-Si alloys were prepared under potentiostatic charging at $10 \text{ mV vs. Li/Li}^+$. The charge densities were 20, 50, 120, 500 and $1000 \text{ mC}\cdot\text{cm}^{-2}$. The structures and compositions of the five Li-Si alloys were determined by using SEM, SXES and windowless EDS to study the Si lithiation process. Under potentiostatic charging, the cathodic current due to lithiation increased to a peak, and then decreased to a constant value. The crystalline $\text{Li}_{15}\text{Si}_4$ layer started to grow along with the Li diffused Li_xSi layer until the lithiation current reached its peak. Thereafter the amorphous $\text{Li}_{13}\text{Si}_4$ alloy started to grow. On the other hand, in situ synchrotron XRD was used to study the Si lithiation. Crystalline $\text{Li}_{15}\text{Si}_4$ layer formed after the lithiation and disappeared after the delithiation.

In Chapter 5, the effects of FEC and HF on the structures and compositions of the Li-Si alloys were studied. The HF were found to be adsorbed on the Si surface. F adsorption made the surface potential more negative and was expected to increase the Li^+ ion concentration on the surface, resulting in more pyramid nuclei formation on the surface. More pyramid nuclei formation resulted in smaller pyramid that covered the Si

surface, i.e., thinner crystalline $\text{Li}_{15}\text{Si}_4$ alloy layer. This explained the reason of FEC to improve the battery performance, since FEC can decompose to generate large amount of HF which can make the pyramid smaller.

In Chapter 6, the solvent effects on the structures and compositions of the Li-Si alloys were studied. The solvents (DMSO, TMS, TEGDME, EA, DMC, PC and FEC) were used to prepare the electrolytes of 1.0 M LiPF_6 in different solvents. It already determined the Li-Si alloys consist of crystalline $\text{Li}_{15}\text{Si}_4$, amorphous $\text{Li}_{13}\text{Si}_4$ and Li diffused Li_xSi alloy phases. The thickness of crystalline $\text{Li}_{15}\text{Si}_4$ alloy layer in the Li-Si alloy decreased by the solvent order $\text{DMSO} > \text{TMS} > \text{EA} > \text{TEGDME} > \text{DMC} > \text{PC} > \text{FEC}$. However, the amorphous $\text{Li}_{13}\text{Si}_4$ alloy layer increased by the above solvent order. It was considered the weaker solvation ability of the solvents to Li^+ ion makes Li^+ ion dis-solvation easier to form more pyramid nuclei on the Si surface. More pyramid nuclei formation resulted in smaller pyramid that covered the Si surface, i.e., thinner crystalline $\text{Li}_{15}\text{Si}_4$ alloy layer.

In Chapter 7, the general conclusion of this thesis and future prospects are given.

References

1. Jacobson, M. Z., Review of solutions to global warming, air pollution, and energy security. *Energy & Environmental Science* **2009**, *2* (2), 148-173.
2. Goodenough, J. B.; Kim, Y., Challenges for Rechargeable Li Batteries. *Chemistry of Materials* **2010**, *22* (3), 587-603.
3. Etacheri, V.; Marom, R.; Elazari, R.; Salitra, G.; Aurbach, D., Challenges in the development of advanced Li-ion batteries: a review. *Energy & Environmental Science* **2011**, *4* (9), 3243-3262.
4. Tarascon, J. M.; Armand, M., Issues and challenges facing rechargeable lithium batteries. *Nature* **2001**, *414* (6861), 359-367.
5. WHITTINGHAM, M. S., Electrical Energy Storage and Intercalation Chemistry. *Science* **1976**, *192* (4244), 1126-1127.
6. Rao, B. M. L.; Francis, R. W.; Christopher, H. A., Lithium-Aluminum Electrode. *J. Electrochem. Soc.* **1977**, *124* (10), 1490-1492.
7. Bruce, P. G.; Freunberger, S. A.; Hardwick, L. J.; Tarascon, J. M., Li-O₂ and Li-S batteries with high energy storage. *Nat. Mater.* **2012**, *11* (1), 19-29.
8. Kinoshita, K., *Metal/Air Batteries*. In *Electrochemical Oxygen Technology*. John Wiley & Sons ed.; 1992.
9. Girishkumar, G.; McCloskey, B.; Luntz, A. C.; Swanson, S.; Wilcke, W., Lithium - Air Battery: Promise and Challenges. *J Phys Chem Lett* **2010**, *1* (14), 2193-2203.
10. Christensen, J.; Albertus, P.; Sanchez-Carrera, R. S.; Lohmann, T.; Kozinsky, B.; Liedtke, R.; Ahmed, J.; Kojic, A., A Critical Review of Li/Air Batteries. *J. Electrochem. Soc.* **2012**, *159* (2), R1-R30.
11. Herbert, D.; Ulam, J. Electric dry cells and storage batteries. 3043896, 1962.
12. Yamin, H.; Penciner, J.; Gorenshain, A.; Elam, M.; Peled, E., THE ELECTROCHEMICAL-BEHAVIOR OF POLYSULFIDES IN TETRAHYDROFURAN. *J Power Sources* **1985**, *14* (1-3), 129-134.
13. Ryu, H. S.; Guo, Z.; Ahn, H. J.; Cho, G. B.; Liu, H., Investigation of discharge reaction mechanism of lithium vertical bar liquid electrolyte vertical bar sulfur battery. *J Power Sources* **2009**, *189* (2), 1179-1183.
14. Choi, Y. J.; Jung, B. S.; Lee, D. J.; Jeong, J. H.; Kim, K. W.; Ahn, H. J.; Cho, K. K.; Gu, H. B., Electrochemical properties of sulfur electrode containing nano Al₂O₃ for lithium/sulfur cell. *Phys Scripta* **2007**, *T129*, 62-65.
15. Cheon, S. E.; Ko, K. S.; Cho, J. H.; Kim, S. W.; Chin, E. Y.; Kim, H. T., Rechargeable lithium sulfur battery - II. Rate capability and cycle characteristics. *J. Electrochem. Soc.* **2003**, *150* (6), A800-A805.
16. Lin, D. C.; Liu, Y. Y.; Cui, Y., Reviving the lithium metal anode for high-energy batteries. *Nature Nanotechnology* **2017**, *12* (3), 194-206.
17. Park, C. M.; Kim, J. H.; Kim, H.; Sohn, H. J., Li-alloy based anode materials for Li secondary batteries. *Chem Soc Rev* **2010**, *39* (8), 3115-3141.
18. Ji, L. W.; Lin, Z.; Alcoutlabi, M.; Zhang, X. W., Recent developments in nanostructured anode materials for rechargeable lithium-ion batteries. *Energy & Environmental Science* **2011**, *4* (8), 2682-2699.
19. Zhu, G. N.; Wang, Y. G.; Xia, Y. Y., Ti-based compounds as anode materials for Li-ion batteries. *Energy & Environmental Science* **2012**, *5* (5), 6652-6667.
20. Goriparti, S.; Miele, E.; De Angelis, F.; Di Fabrizio, E.; Zaccaria, R. P.; Capiglia, C., Review on recent progress of nanostructured anode materials for Li-ion batteries. *J Power Sources* **2014**, *257*, 421-443.

21. Whittingham, M. S., Lithium batteries and cathode materials. *Chem Rev* **2004**, *104* (10), 4271-4301.
22. Flandrois, S.; Simon, B., Carbon materials for lithium-ion rechargeable batteries. *Carbon* **1999**, *37* (2), 165-180.
23. Liu, C.; Neale, Z. G.; Cao, G., Understanding electrochemical potentials of cathode materials in rechargeable batteries. *Mater Today* **2016**, *19* (2), 109-123.
24. Xu, K., Electrolytes and Interphases in Li-Ion Batteries and Beyond. *Chem Rev* **2014**, *114* (23), 11503-11618.
25. Verma, P.; Maire, P.; Novak, P., A review of the features and analyses of the solid electrolyte interphase in Li-ion batteries. *Electrochim Acta* **2010**, *55* (22), 6332-6341.
26. Abraham, K. M.; Jiang, Z., A polymer electrolyte-based rechargeable lithium/oxygen battery. *J. Electrochem. Soc.* **1996**, *143* (1), 1-5.
27. Littauer, E. L.; Tsai, K. C., ANODIC BEHAVIOR OF LITHIUM IN AQUEOUS-ELECTROLYTES .1. TRANSIENT PASSIVATION. *J. Electrochem. Soc.* **1976**, *123* (6), 771-776.
28. Freunberger, S. A.; Chen, Y. H.; Peng, Z. Q.; Griffin, J. M.; Hardwick, L. J.; Barde, F.; Novak, P.; Bruce, P. G., Reactions in the Rechargeable Lithium-O₂ Battery with Alkyl Carbonate Electrolytes. *J Am Chem Soc* **2011**, *133* (20), 8040-8047.
29. Manthiram, A.; Fu, Y. Z.; Chung, S. H.; Zu, C. X.; Su, Y. S., Rechargeable Lithium-Sulfur Batteries. *Chem Rev* **2014**, *114* (23), 11751-11787.
30. Mikhaylik, Y. V.; Akridge, J. R., Polysulfide shuttle study in the Li/S battery system. *J. Electrochem. Soc.* **2004**, *151* (11), A1969-A1976.
31. Barghamadi, M.; Kapoor, A.; Wen, C., A Review on Li-S Batteries as a High Efficiency Rechargeable Lithium Battery. *J. Electrochem. Soc.* **2013**, *160* (8), A1256-A1263.
32. Xu, W.; Wang, J.; Ding, F.; Chen, X.; Nasybulin, E.; Zhang, Y.; Zhang, J.-G., Lithium metal anodes for rechargeable batteries. *Energy & Environmental Science* **2014**, *7* (2), 513-537.
33. Scrosati, B.; Garche, J., Lithium batteries: Status, prospects and future. *J Power Sources* **2010**, *195* (9), 2419-2430.
34. Peled, E., The Electrochemical Behavior of Alkali and Alkaline Earth Metals in Nonaqueous Battery Systems—The Solid Electrolyte Interphase Model. *J. Electrochem. Soc.* **1979**, *126* (12), 2047-2051.
35. Quartarone, E.; Mustarelli, P., Electrolytes for solid-state lithium rechargeable batteries: recent advances and perspectives. *Chem Soc Rev* **2011**, *40* (5), 2525-2540.
36. Kamali, A. R.; Fray, D. J., Review on Carbon and Silicon Based Materials as Anode Materials for Lithium Ion Batteries. *J New Mat Electr Sys* **2010**, *13* (2), 147-160.
37. Matsumura, Y.; Wang, S.; Mondori, J., INTERACTIONS BETWEEN DISORDERED CARBON AND LITHIUM IN LITHIUM ION RECHARGEABLE BATTERIES. *Carbon* **1995**, *33* (10), 1457-1462.
38. Gao, B.; Bower, C.; Lorentzen, J. D.; Fleming, L.; Kleinhammes, A.; Tang, X. P.; McNeil, L. E.; Wu, Y.; Zhou, O., Enhanced saturation lithium composition in ball-milled single-walled carbon nanotubes. *Chem Phys Lett* **2000**, *327* (1-2), 69-75.
39. Gao, B.; Kleinhammes, A.; Tang, X. P.; Bower, C.; Fleming, L.; Wu, Y.; Zhou, O., Electrochemical intercalation of single-walled carbon nanotubes with lithium. *Chem Phys Lett* **1999**, *307* (3-4), 153-157.
40. Obrovac, M. N.; Chevrier, V. L., Alloy Negative Electrodes for Li-Ion Batteries. *Chem Rev* **2014**, *114* (23), 11444-11502.
41. Obrovac, M. N.; Christensen, L., Structural Changes in Silicon Anodes during Lithium Insertion/Extraction. *Electrochemical and Solid-State Letters* **2004**, *7* (5), A93-A96.
42. Okamoto, H., Li-Si (Lithium-Silicon). *Journal of Phase Equilibria and Diffusion* **2009**, *30* (1), 118-

119.

43. Nesper, R., Structure and chemical bonding in zintl-phases containing lithium. *Progress in Solid State Chemistry* **1990**, *20* (1), 1-45.
44. Chevrier, V. L.; Zwanziger, J. W.; Dahn, J. R., First principles study of Li-Si crystalline phases: Charge transfer, electronic structure, and lattice vibrations. *J Alloy Compd* **2010**, *496* (1-2), 25-36.
45. Bond, W. L.; Kaiser, W., INTERSTITIAL VERSUS SUBSTITUTIONAL OXYGEN IN SILICON. *J Phys Chem Solids* **1960**, *16* (1-2), 44-45.
46. Kubota, Y.; Escaño, M. C. S.; Nakanishi, H.; Kasai, H., Electronic structure of LiSi. *J Alloy Compd* **2008**, *458* (1-2), 151-157.
47. Nesper, R.; Vonschering, H. G.; Curda, J., LI₁₂SI₇, A COMPOUND WITH TRIGONAL PLANAR SI₄ CLUSTERS AND ISOMETRIC SI₅ RINGS. *Chem. Ber.-Recl.* **1986**, *119* (12), 3576-3590.
48. Kubota, Y.; Escano, M. C. S.; Nakanishi, H.; Kasai, H., Crystal and electronic structure of Li₁₅Si₄. *J Appl Phys* **2007**, *102* (5).
49. Axel, H.; Schafer, H.; Weiss, A., ZUR KENNTNIS DER PHASE LI₂₂SI₅. *Zeitschrift Fur Naturforschung Part B-Chemie Biochemie Biophysik Biologie Und Verwandten Gebiete* **1966**, *B 21* (2), 115-&.
50. Nadler, M. R.; Kempter, C. P., CRYSTALLOGRAPHIC DATA .186. LITHIUM. *Anal Chem* **1959**, *31* (12), 2109-2109.
51. Son, S.-B.; Trevey, J. E.; Roh, H.; Kim, S.-H.; Kim, K.-B.; Cho, J. S.; Moon, J.-T.; DeLuca, C. M.; Maute, K. K.; Dunn, M. L.; Han, H. N.; Oh, K. H.; Lee, S.-H., Microstructure Study of Electrochemically Driven Li_xSi. *Advanced Energy Materials* **2011**, *1* (6), 1199-1204.
52. Gu, M.; Wang, Z. G.; Connell, J. G.; Perea, D. E.; Lauhon, L. J.; Gao, F.; Wang, C. M., Electronic Origin for the Phase Transition from Amorphous Li_xSi to Crystalline Li₁₅Si₄. *Acs Nano* **2013**, *7* (7), 6303-6309.
53. Choi, Y. S.; Pharr, M.; Kang, C. S.; Son, S.-B.; Kim, S. C.; Kim, K.-B.; Roh, H.; Lee, S.-H.; Oh, K. H.; Vlassak, J. J., Microstructural evolution induced by micro-cracking during fast lithiation of single-crystalline silicon. *J Power Sources* **2014**, *265*, 160-165.
54. Zeng, Z.; Liu, N.; Zeng, Q.; Ding, Y.; Qu, S.; Cui, Y.; Mao, W. L., Elastic moduli of polycrystalline Li₁₅Si₄ produced in lithium ion batteries. *J Power Sources* **2013**, *242*, 732-735.
55. Misra, S.; Liu, N.; Nelson, J.; Hong, S. S.; Cui, Y.; Toney, M. F., In Situ X-ray Diffraction Studies of (De)lithiation Mechanism in Silicon Nanowire Anodes. *Acs Nano* **2012**, *6* (6), 5465-5473.
56. Liu, X. H.; Zhang, L. Q.; Zhong, L.; Liu, Y.; Zheng, H.; Wang, J. W.; Cho, J.-H.; Dayeh, S. A.; Picraux, S. T.; Sullivan, J. P.; Mao, S. X.; Ye, Z. Z.; Huang, J. Y., Ultrafast Electrochemical Lithiation of Individual Si Nanowire Anodes. *Nano Lett* **2011**, *11* (6), 2251-2258.
57. Li, J.; Dahn, J. R., An in situ X-ray diffraction study of the reaction of Li with crystalline Si. *J Electrochem. Soc.* **2007**, *154* (3), A156-A161.
58. Laik, B.; Ung, D.; Caillard, A.; Cojocaru, C. S.; Pribat, D.; Pereira-Ramos, J. P., An electrochemical and structural investigation of silicon nanowires as negative electrode for Li-ion batteries. *Journal of Solid State Electrochemistry* **2010**, *14* (10), 1835-1839.
59. Chan, C. K.; Ruffo, R.; Hong, S. S.; Huggins, R. A.; Cui, Y., Structural and electrochemical study of the reaction of lithium with silicon nanowires. *J Power Sources* **2009**, *189* (1), 34-39.
60. Liu, X. H.; Wang, J. W.; Huang, S.; Fan, F. F.; Huang, X.; Liu, Y.; Krylyuk, S.; Yoo, J.; Dayeh, S. A.; Davydov, A. V.; Mao, S. X.; Picraux, S. T.; Zhang, S. L.; Li, J.; Zhu, T.; Huang, J. Y., In situ atomic-scale imaging of electrochemical lithiation in silicon. *Nature Nanotechnology* **2012**, *7* (11), 749-756.

61. Liu, X. H.; Zhong, L.; Huang, S.; Mao, S. X.; Zhu, T.; Huang, J. Y., Size-Dependent Fracture of Silicon Nanoparticles During Lithiation. *Acs Nano* **2012**, *6* (2), 1522-1531.
62. McDowell, M. T.; Lee, S. W.; Harris, J. T.; Korgel, B. A.; Wang, C. M.; Nix, W. D.; Cui, Y., In Situ TEM of Two-Phase Lithiation of Amorphous Silicon Nanospheres. *Nano Lett* **2013**, *13* (2), 758-764.
63. Etacheri, V.; Haik, O.; Goffer, Y.; Roberts, G. A.; Stefan, I. C.; Fasching, R.; Aurbach, D., Effect of Fluoroethylene Carbonate (FEC) on the Performance and Surface Chemistry of Si-Nanowire Li-Ion Battery Anodes. *Langmuir* **2012**, *28* (1), 965-976.
64. Kohandehghan, A.; Kalisvaart, P.; Cui, K.; Kupsta, M.; Memarzadeh, E.; Mitlin, D., Silicon nanowire lithium-ion battery anodes with ALD deposited TiN coatings demonstrate a major improvement in cycling performance. *J Mater Chem A* **2013**, *1* (41), 12850-12861.
65. Lee, Y. M.; Lee, J. Y.; Shim, H.-T.; Lee, J. K.; Park, J.-K., SEI layer formation on amorphous si thin electrode during precycling. *J. Electrochem. Soc.* **2007**, *154* (6), A515-A519.
66. Pereira-Nabais, C.; Swiatowska, J.; Chagnes, A.; Ozanam, F.; Gohier, A.; Tran-Van, P.; Cojocar, C.-S.; Cassir, M.; Marcus, P., Interphase chemistry of Si electrodes used as anodes in Li-ion batteries. *Appl Surf Sci* **2013**, *266*, 5-16.
67. Philippe, B.; Dedryvere, R.; Allouche, J.; Lindgren, F.; Gorgoi, M.; Rensmo, H.; Gonbeau, D.; Edstrom, K., Nanosilicon Electrodes for Lithium-Ion Batteries: Interfacial Mechanisms Studied by Hard and Soft X-ray Photoelectron Spectroscopy. *Chemistry of Materials* **2012**, *24* (6), 1107-1115.
68. Schroder, K. W.; Celio, H.; Webb, L. J.; Stevenson, K. J., Examining Solid Electrolyte Interphase Formation on Crystalline Silicon Electrodes: Influence of Electrochemical Preparation and Ambient Exposure Conditions. *J. Phys. Chem. C* **2012**, *116* (37), 19737-19747.
69. Arreaga-Salas, D. E.; Sra, A. K.; Roodenko, K.; Chabal, Y. J.; Hinkle, C. L., Progression of Solid Electrolyte Interphase Formation on Hydrogenated Amorphous Silicon Anodes for Lithium-Ion Batteries. *J. Phys. Chem. C* **2012**, *116* (16), 9072-9077.
70. Key, B.; Bhattacharyya, R.; Morcrette, M.; Seznec, V.; Tarascon, J.-M.; Grey, C. P., Real-Time NMR Investigations of Structural Changes in Silicon Electrodes for Lithium-Ion Batteries. *J Am Chem Soc* **2009**, *131* (26), 9239-9249.
71. An, Z. L.; Kamezawa, C.; Hirai, M.; Kusaka, M.; Iwami, M., Valence band density of states of Cu₃Si studied by soft X-ray emission spectroscopy and a first-principle molecular orbital calculation. *Journal of the Physical Society of Japan* **2002**, *71* (12), 2948-2952.
72. Terauchi, M.; Koshiya, S.; Satoh, F.; Takahashi, H.; Handa, N.; Murano, T.; Koike, M.; Imazono, T.; Koeda, M.; Nagano, T.; Sasai, H.; Oue, Y.; Yonezawa, Z.; Kuramoto, S., Chemical State Information of Bulk Specimens Obtained by SEM-Based Soft-X-Ray Emission Spectrometry. *Microscopy and Microanalysis* **2014**, *20* (3), 692-697.
73. Aoki, N.; Omachi, A.; Uosaki, K.; Kondo, T., Structural Study of Electrochemically Lithiated Si(111) by using Soft X-ray Emission Spectroscopy Combined with Scanning Electron Microscopy and through X-ray Diffraction Measurements. *Chemelectrochem* **2016**, *3* (6), 959-965.
74. Hovington, P.; Timoshevskii, V.; Burgess, S.; Demers, H.; Statham, P.; Gauvin, R.; Zaghbi, K., Can we detect Li K X-ray in lithium compounds using energy dispersive spectroscopy? *Scanning* **2016**, *38* (6), 571-578.
75. Wu, H.; Cui, Y., Designing nanostructured Si anodes for high energy lithium ion batteries. *Nano Today* **2012**, *7* (5), 414-429.
76. Wang, Y. D.; Dahn, J., Phase changes in electrochemically lithiated silicon at elevated temperature. *J. Electrochem. Soc.* **2006**, *153* (12), A2314-A2318.

77. Beaulieu, L. Y.; Hatchard, T. D.; Bonakdarpour, A.; Fleischauer, M. D.; Dahn, J. R., Reaction of Li with Alloy Thin Films Studied by In Situ AFM. *J. Electrochem. Soc.* **2003**, *150* (11), A1457-A1464.
78. Wen, C. J.; Huggins, R. A., CHEMICAL DIFFUSION IN INTERMEDIATE PHASES IN THE LITHIUM-SILICON SYSTEM. *J Solid State Chem* **1981**, *37* (3), 271-278.
79. Kang, C. S.; Son, S. B.; Kim, J. W.; Kim, S. C.; Choi, Y. S.; Heo, J. Y.; Suh, S. S.; Kim, Y. U.; Chu, Y. Y.; Cho, J. S.; Lee, S. H.; Oh, K. H., Electrochemically induced and orientation dependent crack propagation in single crystal silicon. *J Power Sources* **2014**, *267*, 739-743.
80. Goldman, J. L.; Long, B. R.; Gewirth, A. A.; Nuzzo, R. G., Strain Anisotropies and Self-Limiting Capacities in Single-Crystalline 3D Silicon Microstructures: Models for High Energy Density Lithium-Ion Battery Anodes. *Advanced Functional Materials* **2011**, *21* (13), 2412-2422.
81. Lee, S. W.; McDowell, M. T.; Choi, J. W.; Cui, Y., Anomalous Shape Changes of Silicon Nanopillars by Electrochemical Lithiation. *Nano Lett* **2011**, *11* (7), 3034-3039.
82. Chan, M. K. Y.; Wolverton, C.; Greeley, J. P., First Principles Simulations of the Electrochemical Lithiation and Delithiation of Faceted Crystalline Silicon. *J Am Chem Soc* **2012**, *134* (35), 14362-14374.
83. Jung, S. C.; Choi, J. W.; Han, Y. K., Anisotropic Volume Expansion of Crystalline Silicon during Electrochemical Lithium Insertion: An Atomic Level Rationale. *Nano Lett* **2012**, *12* (10), 5342-5347.
84. Carvalho, A.; Rayson, M. J.; Briddon, P. R.; Manzhos, S., Effect of the adsorption of ethylene carbonate on Si surfaces on the Li insertion behavior. *Chem Phys Lett* **2013**, *585*, 157-161.
85. Pharr, M.; Zhao, K.; Wang, X.; Suo, Z.; Vlassak, J. J., Kinetics of Initial Lithiation of Crystalline Silicon Electrodes of Lithium-Ion Batteries. *Nano Lett* **2012**, *12* (9), 5039-5047.
86. Zhao, K.; Pharr, M.; Wan, Q.; Wang, W. L.; Kaxiras, E.; Vlassak, J. J.; Suo, Z., Concurrent Reaction and Plasticity during Initial Lithiation of Crystalline Silicon in Lithium-Ion Batteries. *J. Electrochem. Soc.* **2012**, *159* (3), A238-A243.
87. Nie, M. Y.; Abraham, D. P.; Chen, Y. J.; Bose, A.; Lucht, B. L., Silicon Solid Electrolyte Interphase (SEI) of Lithium Ion Battery Characterized by Microscopy and Spectroscopy. *J. Phys. Chem. C* **2013**, *117* (26), 13403-13412.
88. Ruffo, R.; Hong, S. S.; Chan, C. K.; Huggins, R. A.; Cui, Y., Impedance Analysis of Silicon Nanowire Lithium Ion Battery Anodes. *J. Phys. Chem. C* **2009**, *113* (26), 11390-11398.
89. Yang, Y.; McDowell, M. T.; Jackson, A.; Cha, J. J.; Hong, S. S.; Cui, Y., New Nanostructured Li₂S/Silicon Rechargeable Battery with High Specific Energy. *Nano Lett* **2010**, *10* (4), 1486-1491.
90. Hassoun, J.; Jung, H. G.; Lee, D. J.; Park, J. B.; Amine, K.; Sun, Y. K.; Scrosati, B., A Metal-Free, Lithium-Ion Oxygen Battery: A Step Forward to Safety in Lithium-Air Batteries. *Nano Lett* **2012**, *12* (11), 5775-5779.
91. Elazari, R.; Salitra, G.; Gershinshy, G.; Garsuch, A.; Panchenko, A.; Aurbach, D., Rechargeable lithiated silicon-sulfur (SLS) battery prototypes. *Electrochem Commun* **2012**, *14* (1), 21-24.
92. Hassoun, J.; Kim, J.; Lee, D. J.; Jung, H. G.; Lee, S. M.; Sun, Y. K.; Scrosati, B., A contribution to the progress of high energy batteries: A metal-free, lithium-ion, silicon-sulfur battery. *J Power Sources* **2012**, *202*, 308-313.
93. Freunberger, S. A.; Chen, Y. H.; Drewett, N. E.; Hardwick, L. J.; Barde, F.; Bruce, P. G., The Lithium-Oxygen Battery with Ether-Based Electrolytes. *Angew Chem Int Edit* **2011**, *50* (37), 8609-8613.
94. Xu, D.; Wang, Z. L.; Xu, J. J.; Zhang, L. L.; Zhang, X. B., Novel DMSO-based electrolyte for high performance rechargeable Li-O₂ batteries. *Chem Commun* **2012**, *48* (55), 6948-6950.
95. Zhang, S. S., Liquid electrolyte lithium/sulfur battery: Fundamental chemistry, problems, and solutions. *J Power Sources* **2013**, *231*, 153-162.

Chapter 2

Experimental

2.1 Chemicals

H₂SO₄ (96~98%), H₂O₂ (30~35%), HCl (35%), and HF (46%) were purchased from Wako Pure Chemicals. 40% NH₄F aqueous solution (semiconductor grade) was purchased from Morita Chemical Industry. LiPF₆ salt (99.9%) and Li wire (99%) were purchased from Kishida Chemical and Sigma-Aldrich, respectively, and stored in a glove box (moisture < 0.5 ppm, oxygen < 0.5 ppm). Dimethyl carbonate (DMC, 99%, battery grade), dimethyl sulfoxide (DMSO, 99%), tetraethylene glycol dimethyl ether (TEGDME, 98%), and fluoro ethylene carbonate (FEC, 99.5%) solvents were purchased from Kishida Chemical. Propylene carbonate (PC, 99.7%), ethyl acetate (EA, 99.5%) and tetramethylene sulfone (TMS, 99%) solvents were purchased from Sigma-Aldrich. All the solvents were dried with 3A molecular sieve for at least 3 days, and finally used after filtering with a nylon filter in the glove box. Si(111) single-crystal wafers (thickness: 500 μm, resistivity: 1–10 Ω cm⁻¹, n-type: phosphorous-doped) were purchased from Shin-Etsu Semiconductor. Mill-Q water and 99.999% Ar gas were used throughout the experiments.

2.2 Electrochemical Measurements and Li-Si Alloys Preparation

2.2.1 Hydrogen-terminated Si(111) Electrode Preparation

The Si(111) wafer was cut into 1.0×1.0 cm² pieces. The hydrogen-terminated Si(111) was prepared through chemical etching as reported.¹ The Si pieces were cleaned in piranha solution (H₂SO₄/H₂O₂ = 2:1) for 30 min to remove organic contaminants, etched in 0.5% HF solution to remove the native oxide from the surface, re-oxidized in HCl/H₂O₂/H₂O (1:1:4) solution for 20 min at 85 °C, and then etched for 5 min in 40% NH₄F solution that was degassed with Ar gas for 30 min.

2.2.2 Cyclic Voltammetry Measurements

The hydrogen-terminated Si(111) was then transferred to an Ar-filled glove box and installed in a Teflon type three-electrode cell by connecting the backside to a stainless

steel current collector with InGa alloy, and the side touching the electrolyte was connected with an O-ring with an area of about 0.4 cm². Lithium wire was used as both reference and counter electrodes. The schematic of the electrochemical cell configuration is shown in Figure 2-1. The electrolytes were prepared by dissolving 1.0 M LiPF₆ in DMC, DMSO, TEGDME, EA, PC, TMS and FEC solvents. Cyclic voltammetry was conducted between 2.7 and 0.01 V vs. Li/Li⁺ with a scan rate of 1 mV·s⁻¹ using a potentiostat (Hokuto Denko, HZ-5000) to control the electrode potential.

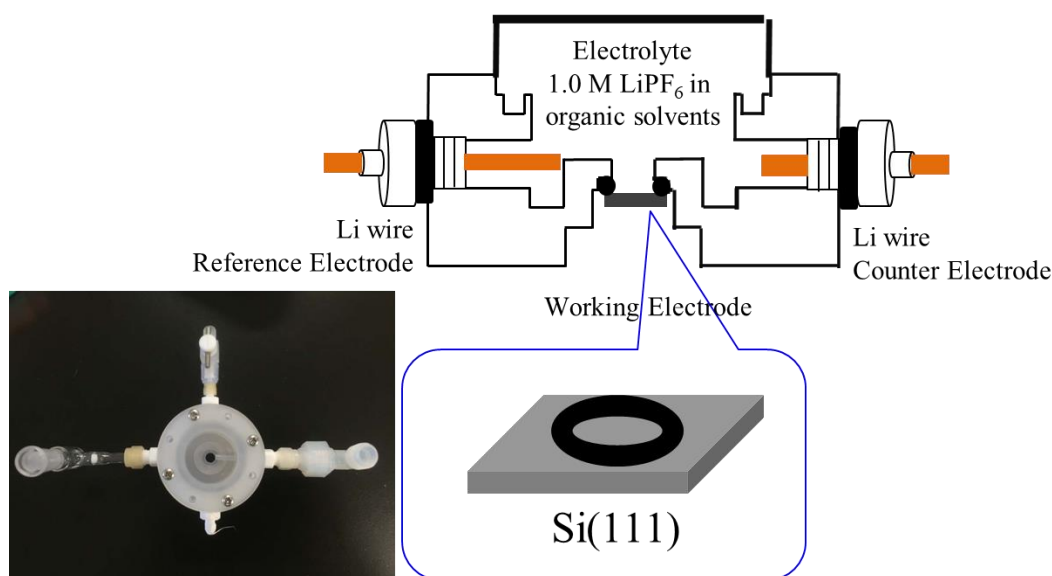


Figure 2-1 Schematic and photo (lower left) of the electrochemical cell

2.2.3 Li-Si Alloys Preparation under Potentiostatic Lithiation

Potentiostatic measurements were conducted by stepping the potential from 0.5 to 0.01 V vs. Li/Li⁺ to obtain the current as a function of time for electrochemical analysis. In Chapter 3, a Li-Si alloy was prepared by potentiostatically charging at 10 mV in 1.0 M LiPF₆ in DMC. The lithiation charge was 400 mC (charge density: 1000 mC·cm⁻², working electrode surface area: 0.4 cm²). After preparation, the sample was washed with DMC solvent and broken into half with a diamond pen along the Si <110> direction to show up the cross section, and then transferred without air exposure for SXES and windowless EDS measurements by an transfer vessel. In Chapter 4, five Li-Si alloys were prepared by potentiostatically charging at 10 mV in 1.0 M LiPF₆ in DMC using holding times of 30 s (20 mC·cm⁻²), 60 s (50 mC·cm⁻²), 150 s (120 mC·cm⁻²), 1000 s

(500 $\text{mC}\cdot\text{cm}^{-2}$) and 2500 s (1000 $\text{mC}\cdot\text{cm}^{-2}$) after stepping the potential to 10 mV. In Chapter 5, different Li-Si alloys were prepared by potentiostatically charging at 10 mV in 1.0 M LiPF_6 in PC with an addition of 0, 0.5, 1, 2, 4 mM HF aqueous solution. The Li-Si alloy was also prepared in 1.0 M LiPF_6 in FEC to compare with PC. In Chapter 6, different Li-Si alloys were prepared by potentiostatically charging at 10 mV in 1.0 M LiPF_6 in DMC, DMSO, EA, TEGDME, PC, TMS and FEC. The lithiation charge density is 1000 $\text{mC}\cdot\text{cm}^{-2}$ for all of the Li-Si alloys prepared in both chapter 5 and 6. After electrochemical preparation, the samples were washed with DMC solvent and broken into half with a diamond pen along the Si $\langle 110 \rangle$ direction, and then transferred by transfer vessel without air exposure for windowless EDS, SXES measurements.

2.3 Scanning Electron Microscopy (SEM) Measurements

SEM measurements were carried out by using a scanning electron microscope (JEOL, JSM-7800F, Figure 2-2) under an ambient pressure of less than 10^{-4} Pa. The incident electron energy was employed to be 5.0 keV. The SEM images were obtained by detecting both secondary and backscattered electrons with a spatial resolution of 8 nm. The Li-Si alloy specimens were measured for both surface and cross-section. The specimen was broken into half with a diamond pen along the Si $\langle 110 \rangle$ direction to show up the cross section for cross-section measurements. All the Li-Si alloys prepared in Chapter 3, 4, 5 and 6 were measured in the same SEM condition.

Electrons can be extracted from various sources like tungsten or lanthanum hexaboride (LaB_6) single crystal filament and driven by an electrical potential along an evacuated column. Electrons generated in this way are called primary electrons (PE), and they can be formed into a finely focused beam and systematically scanned across a specimen surface of interest.² The primary electrons accelerated onto a material result in a number of interactions with the atoms of the target specimen as shown in Figure 2-2, emitting typical signals used for imaging include secondary electrons (SE), backscattered electrons (BSE), cathodoluminescence (CL), auger electrons and characteristic X-rays. The elastic and inelastic scattering result in a number of signals that are used for imaging, quantitative and semiquantitative information of the target specimen.

Secondary electron (SE) and Backscattered electron (BSE) are the most important signals for SEM image recording. Conventionally, electrons with energies less than 50 eV are called SE and those bigger than 50 eV are called BSE.³ The differences in specimen composition and surface topography affect the generation, transport and escape of BSEs and SEs.

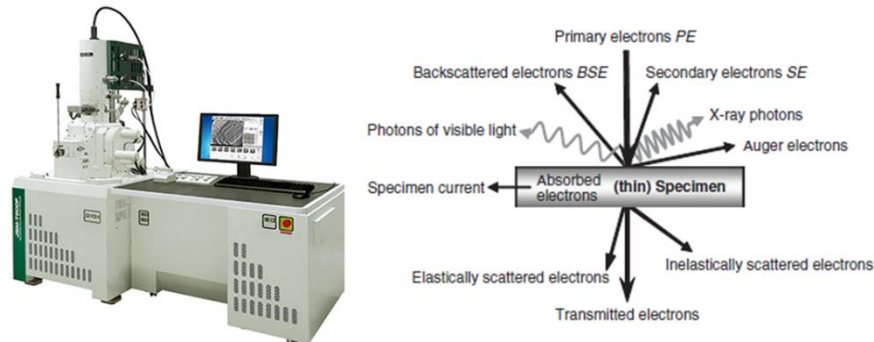


Figure 2-2 Photo of JSM-7800F SEM instrument, and useful signals from the interactions between electrons and a specimen²

The collection of SEs and BSEs by an effective detector is important to show a distinct image for the specimen surface. Everhart-Thornley detector is the most effective detection systems for these signals. The work principle is shown in Figure 2-3. The emitted electrons are collected by a positively biased grid of collector in front of a scintillator biased at 10 kV. The accelerated electrons then strike the scintillator and emit light through the light pipe. Then the light emission is recorded by a photomultiplier tube and electronic amplifier to produce output electronic signal. The BSEs were also collected and recorded by increasing solid angle of collection. The recording process was similar to that of SEs recording, which excites scintillator to generator light to be recorded by photomultiplier tube and electronic amplifier.

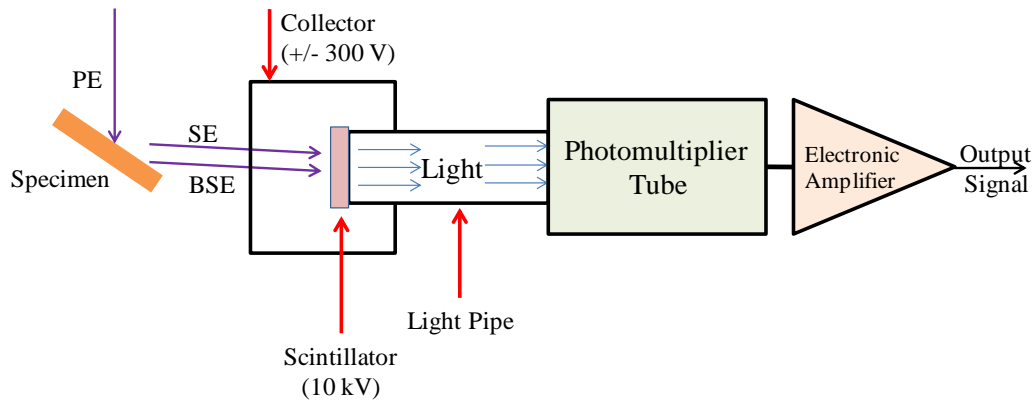


Figure 2-3 Schematic for Everhart-Thornley detector using scintillator-photomultiplier combination

2.4 Energy Dispersive Spectroscopy (EDS) Measurements

Windowless EDS measurements were conducted via windowless silicon drift detector (SDD) system (Oxford Instruments, X-Max Extreme) with high spatial resolution and sensitivity. Spectra were acquired under an ambient pressure of less than 10^{-4} Pa and an accelerating voltage of 5.0 kV. The samples were divided in half to show up the cross section to measure the cross-sectional depth dependent composition. The line scan method of windowless EDS measurements from the surface of the Si substrate was conducted point by point. Every point accumulation time was 15 s. All Li-Si alloys prepared in Chapter 3, 4, 5 and 6 were transferred to the SEM chamber without air exposure by transfer vessel.

2.4.1 Working Principle of EDS

As shown in Figure 2-2, the interaction between electrons and matter will generate X-ray photons including continuous and characteristic X-rays. During inelastic scattering of the primary electrons with atoms, X-rays can be formed by two distinctly different processes.⁴⁻⁵ A process is described that the primary electrons can undergo deceleration in the coulombic field of the atoms and produce continuum X-rays because of the energy loss of the primary electrons. This continuous X-ray component is nonspecific and forms a background in EDS at all energies. The other process is described that a strongly bound electron in inner orbital is excited by primary electrons and result in electron transitions between energetic states to generate characteristic X-

rays. The characteristic X-ray were basically determined by the atomic number and the number and distributions of the electrons according to the different possible quantum states.⁴ This feature will serve as basis for EDS analysis.

The emission processes of characteristic X-ray of atoms can be illustrated clearly in Figure 2-4 for the emission of Si K_{α} as examples. The primary electrons can bombard and eject the tightly bound inner K shell electron, leaving a vacancy in the K shell; the Si atom being excited by the primary electrons is under an unstable energy state. When an atomic electron from an outer shell such as L-shell electron fills the K-shell vacancy, the characteristic X-ray photon will be emitted during this de-excitation process, for example in Si atom, Si K_{α} will be emitted.

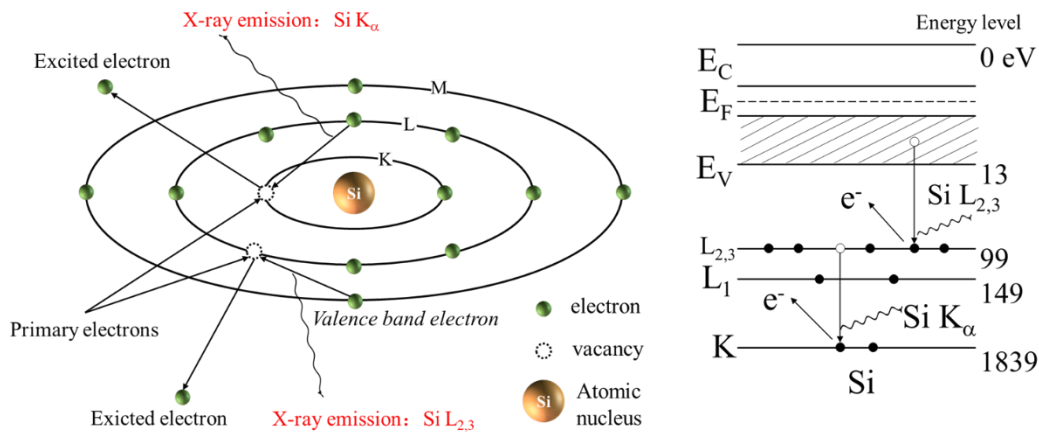


Figure 2-4 Schematic illustration of the process of inner-shell ionization and subsequent de-excitation by electron transitions for the emission of Si K_{α} and $L_{2,3}$ X-ray emissions

First, the X-ray photon energy can be used to determine the element species. It is equal to the difference between the energies of the initial and final states. Since the energies of the electrons in each shell are precisely defined, the energy difference of the electron transition is therefore a characteristic value. Here Si K_{α} has characteristic energy of 1.74 keV (the value is obtained by subtracting 0.099 from 1.839 keV as shown in Figure 2-4) to determine Si atom. Similarly, each atom has its characteristic X-ray emission, and in general the characteristic X-ray energy of a series satisfies Moseley's law of equation 2-1:⁵

$$E_x \propto (Z - \sigma)^2 \quad 2-1$$

where σ is the screening constant of the corresponding shell. Basically, the characteristic X-ray emissions set the basis for elemental analysis since the inner shell energies of atom are not affected by the chemical environment. If the X-ray photon emits by electron transfer from the valence band to the inner shell, the chemical environment will have effects on the X-ray emission energy and intensity since the emission are involved in chemical bond type. For example, for Si the X-ray emission from valence band is illustrated in Figure 2-4 for Si L_{2,3}, which is produced by the electron transition from the valence band to Si L₂ and L₃ shell. The change of chemical bond for Si will change the shape and intensity of Si L_{2,3} X-ray emission. Therefore, the type of X-ray emission used for quantitative elemental analysis is usually chosen to be the X-ray emission not from the valence band electron transition, i.e., Si K_α is more suitable for quantitative analysis than Si L_{2,3} X-ray emission.

Second, the concentration of the element in the specimen can be calculated according to the intensity ratio of X-rays in characteristic energy produced in the specimen and in a pure element standard as reference for quantitative X-ray analysis. Although there exist many factors such as atomic number, X-ray absorption and fluorescence need to be considered, the chemical composition measurements can be obtained within an accuracy approaching 1% according to the measured X-rays intensities with the proper experimental setup and data-reduction procedures.⁵

The technique to efficiently detect the characteristic X-ray emissions for elemental analysis is energy dispersive spectroscopy (EDS). Because of the ease of operation, lithium-drifted silicon (Si(Li)) solid-state x-ray detector is often the choice for both EDS qualitative and quantitative analysis as shown in Figure 2-5.

Usually there is a thin window like Be metal or polymer to isolate the specimen to the detector in case of contamination. As shown in Figure 2-5, the X-ray emits from the specimen under the electron beam excitation, and pass through the thin window to the detector. When the X-ray photon is captured, electrons are promoted into the conduction, leaving holes in the valence band. The absorption of each individual X-ray photon by

the detector will make the formation of electron-hole pairs. Under the applied bias, the electron-hole pairs will be swept away to form a charge pulse, which is then converted to a voltage pulse by an amplifier and recorded by a computer.

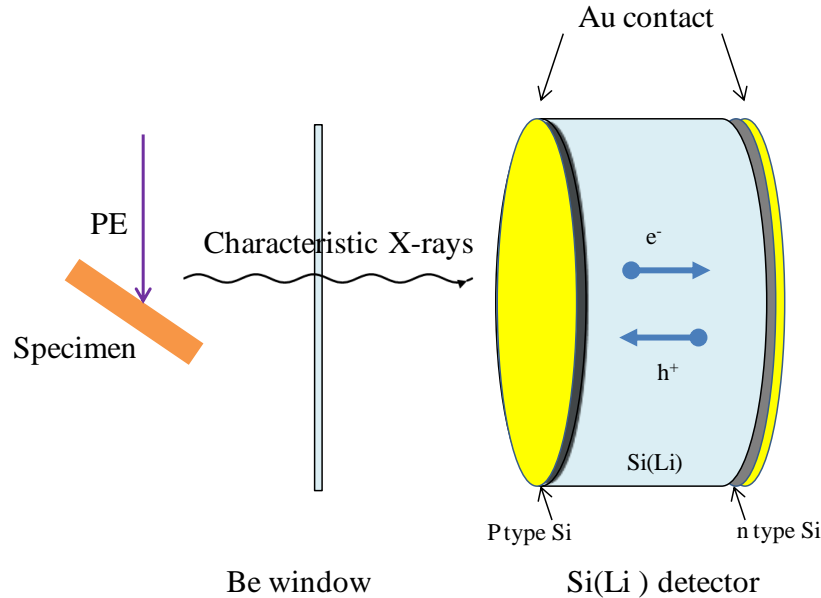


Figure 2-5 Schematic illustration of typical Si(Li) detector

Amplitude of each voltage pulse is relative to the number of electron-hole pairs, and proportional to the energy of the incoming X-ray photon, which can be described by the following equation under ideal condition that all the energy of X-ray photon is absorbed to generate electron-hole pairs,

$$n = \frac{E}{\varepsilon} \quad 2-2$$

where $\varepsilon = 3.8$ eV for Si, E is the energy of the incoming X-ray photon. This is the principle that an EDS works in. The height of each absorption process to convert into voltage is a few millivolts and occurs over a period of about 150 ns.⁵

In addition to Si(Li), there is another type of detector named silicon drift detector (SDD), which is more efficient than Si(Li) detector. The SDD is similar to Si(Li) detector in that electron-hole pairs are generated, but the physical design is radically different. Especially SDD use high purity Si with a very low leakage current because liquid nitrogen cooling is not needed for SDD, but instead a simple Peltier cooler is used. Meanwhile there is a lower capacitance because SDD integrate the FET directly into the chip. In Si(Li) detector, FET is located as an external circuit to convert the current into

a voltage. As a result, the capacitance between FET and detector is not low enough. But in SDD design, the integration of FET into the chip reduces the capacitance strongly, therefore reduce the electronic noise. Thus, compared with Si(Li) detector, SDD has many advantages including high intensities and low noise.

2.4.2 Windowless EDS Measurements

Since the window exists in conventional EDS to isolate the specimen to the detector as shown in Figure 2-5, the ultra-soft X-ray region below 150 eV cannot be detected because of the adsorption of X-ray by Be metal window. If there is no window between the specimen and the detector, the adsorption of X-ray below 150 eV will be avoided. Therefore, windowless EDS is advanced design to detect the X-ray region such as Li K_{α} (54 eV) or Si $L_{2,3}$ (90 eV) emissions.⁶⁻⁷ As is known, lithium is the key element for the development of lithium based secondary battery. It is important to quantitatively determine the Li element distribution among the battery material relative to the battery performance such as cycle life and energy density. The ability of windowless EDS measurement for a metallic Li film to detect the Li is shown in Figure 2-6, which observe a very high Li K_{α} emission peak.⁷

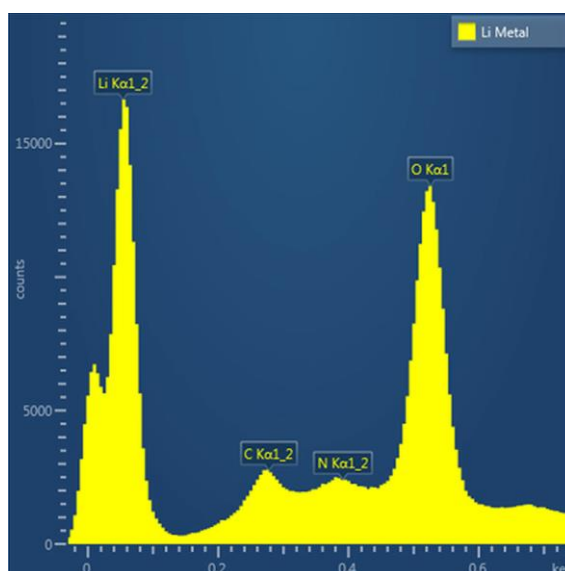


Figure 2-6 X-ray spectrum of metallic Li film taken at 5 kV with a beam current of 1.1 nA⁷

Since windowless EDS has the ability to detect all X-rays over greatly wide energy range including ultra-soft X-ray regions, it provides the possibility to detect Li

distribution according to Li K_{α} emission intensity and other characteristic X-ray emission from other elements. For example, characteristic X-ray emissions of Li K_{α} , Si K_{α} and Si $L_{2,3}$ for Li-Si alloy are expected to be detected simultaneously to elucidate the Li distribution among Li-Si alloys. In addition, windowless operation can make the working distance of the detector to be shorter, increasing the efficiency of X-ray photon collection, so the lower beam current and accelerating voltage can be used to the benefit of not destroying the specimen, especially for the electron beam sensitive Li-host materials. However, low energy resolution is problem of windowless EDS measurement to detect ultra-soft X-ray region. If there are many X-ray emissions components around 0.1 keV, it will bring the signal overlap problem. Therefore, separation and assignment of these signals will be important for analyzing the element distribution, such as Li element.

2.5 Soft X-ray Emission Spectroscopy (SXES)

SXES measurements were conducted via a SXES system (JEOL, SS-9400SXES). Spectra were acquired under an ambient pressure of less than 10^{-4} Pa and an accelerating voltage of 5.0 kV. The incident electron spot size for SXES was approximately $1.0 \mu\text{m}$ and a varied line-space grating (JEOL, JS50XL) was applied with a resolution of approximately 0.15 eV. The probe current and acquisition time were 50 nA and 200 s, respectively. The samples were divided in half to show the cross section to measure the cross-sectional depth dependent spectra. All Li-Si alloys prepared in Chapter 3, 4, 5 and 6 were transferred to the SEM chamber without air exposure by transfer vessel. The principle of SXES is introduced as follows.

The X-ray emissions can be detected by using another type of detector called wavelength dispersive spectroscopy (WDS). According to Bragg's law,

$$n\lambda = 2d \sin \theta \quad 2-3$$

where n is an integer, λ is the X-ray wavelength, d is the interplanar spacing of a crystal, and θ is the angle of incidence of the X-ray, only the X-rays of a single wavelength can be reflected by the crystal when the wavelength coincides with this equation. This principle becomes the base for wavelength dispersive spectroscopy

analysis. In conventional WDS, a spectrum can be scanned by rotating the crystal through an annular range and rotating the detector at twice the angular speed.³ By changing the incidence angle, the X-rays photon with specific λ is selectively detected, and its intensity is recorded by a proportional counter as shown in Figure 2-7.

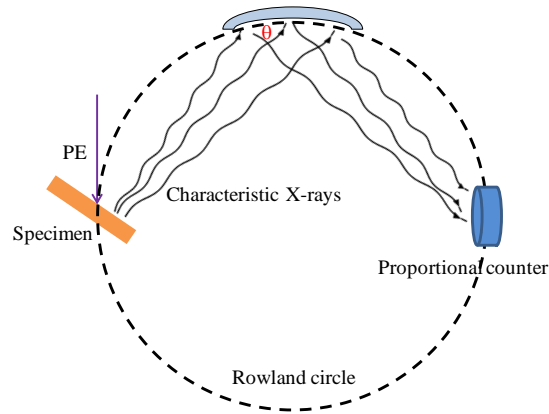


Figure 2-7 Schematic illustration of typical WDS detector

The X-ray photon can be also selectively reflected by using a varied-line-spacing (VLS) grating instead of analyzer crystal for ultra-soft X-rays range below 1 keV. In conventional WDS, the analyzer crystal needs to move along the Rowland circle to change the incidence angle θ , and obtain a spectrum in a certain energy range with an energy resolution of about 10 eV. This energy resolution is still not enough for soft X-rays below 1 keV, especially the X-rays emitted by transition from the valence band to inner vacancy, which can reveal the density of states of the valence band. The VLS grating has a series of etching lines with varied spacing. According to Equation 2-3, the light can be monochromatic by changing the spacing d while fixing the incident angle θ .⁸⁻⁹ The VLS grating obtains a spectrum on a flat plane but not on a Rowland circle for a certain energy range. Coupled with an X-ray photon detector called charge-coupled-device (CCD), a soft X-ray emission spectroscopy (SXES) is able to be constructed without a moving mechanism as shown in Figure 2-8.¹⁰⁻¹¹

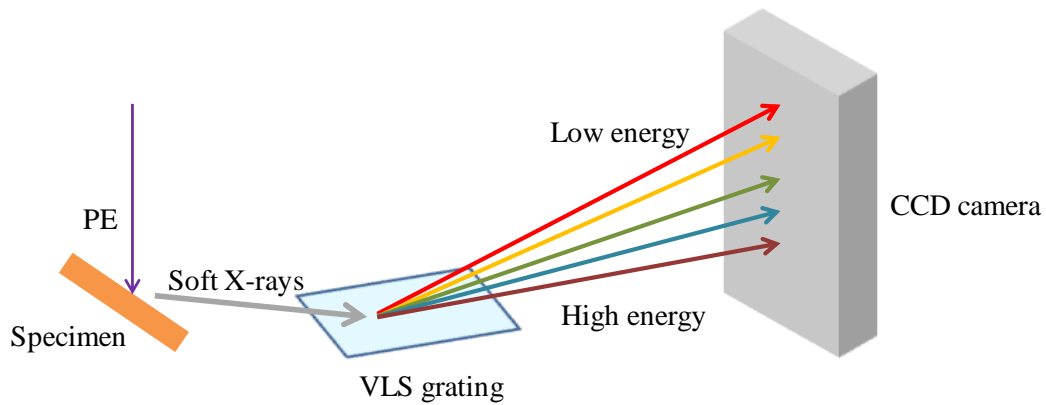


Figure 2-8 Schematic illustration of SXES devices

The SXES enables simultaneous measurement of spectra with different energies, without moving the diffraction grating and detector. It provides high spectral resolution close to 0.15 eV, and also the ability to detect light element including Li. In addition, it is able to obtain the chemical state analysis of elements. For example, as shown in Figure 2-9, Si L_{2,3} emission can be obtained by SXES to reveal the DOS of crystalline Si. The Si L_{2,3} emission peaks were considered to be associated with low-lying Si 3s-3s bonding state at 89.6 eV, and the main peak at 92.0 eV and the shoulder at 96.0 eV originate from p components of sp³ hybridization.¹²⁻¹³

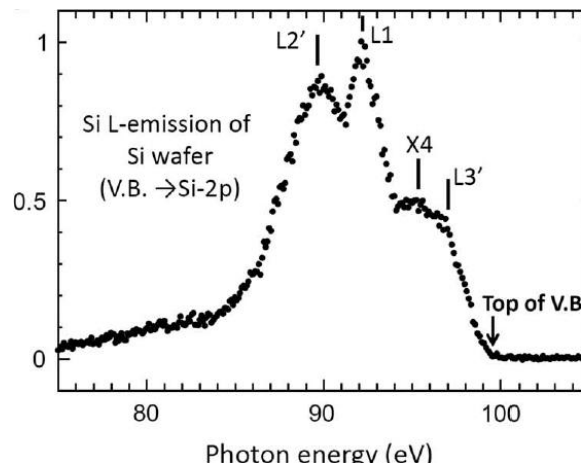


Figure 2-9 Si L_{2,3} emission spectrum¹⁴

2.6 In-situ Synchrotron X-ray Diffraction (SXRD) Measurements

In-situ SXRD measurements were conducted using the BL15XU beamline at SPring-8 without air exposure through the use of Kapton polyimide film as a window in an in-house-built sample holder. The incident X-ray energy used was 19 keV ($\lambda=0.653$

Å).

Synchrotron X-ray Diffraction (SXRD) is a very useful technique to analyze unknown materials efficiently. Consisting of narrow, powerful beams of electromagnetic radiation, synchrotron radiation is produced when electron beams, accelerated to nearly the speed of light, are forced to travel in a curved path by a magnetic field. A simplified sketch of a storage ring is shown in Figure 2-10. It is worthy noted that synchrotron sources are very large scale national facilities. The diameter of the storage ring may be hundreds of meters. The synchrotron XRD instrument at BL15XU in Spring-8 was shown in Figure 2-10.

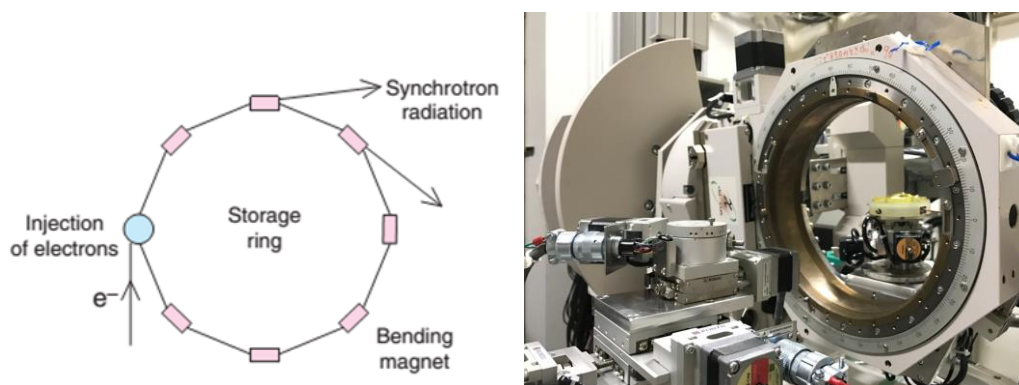


Figure 2-10 Schematic diagram of a synchrotron storage ring and a picture of BL15XU in Spring-8.

The in-situ measurement of Li-Si alloy growth was conducted in 1 M LiPF₆ in TEGDME. The electrochemical cell for in-situ measurement is shown in Figure 2-11a. The working electrode Si(111) was connected to a tungsten wire, and Li wire was used as both reference and counter electrode. Kapton film was used to seal the electrolyte. The peak intensity changes at $\theta = 24.6$ was monitored, which is corresponding to the crystalline Li₁₅Si₄(111) diffraction peak, during the electrochemical lithiation of Si(111) as shown in Figure 2-11b. The potential was stepped to 10 mV to conduct electrochemical lithiation for 10 hour, and then stepped to 2.0 V to conduct electrochemical delithiation for 4 hours.

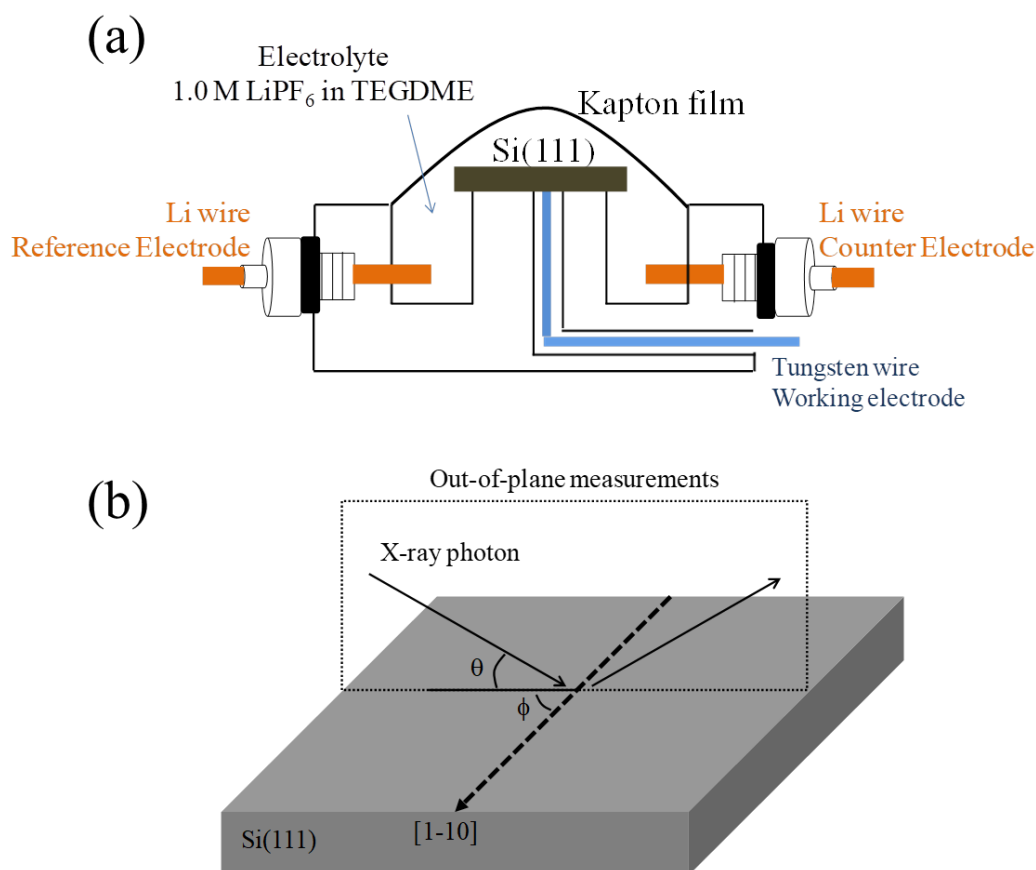


Figure 2-11 (a) schematic of an electrochemical cell for in-situ measurement and (b) schematic for the in-situ out-of-plan XRD measurement

SXRD works according to Bragg diffraction principle of Equation 2-3. The planar spacing d can be determined by the title angle θ when the wavelength λ of incident light is fixed. And the structures and components of materials can be determined according to XRD pattern. SXRD was conducted using a Debye-Scherrer camera installed on BL15XU beamline at SPring-8 at room temperature, which is located in Harima Science Park City, Hyogo Prefecture, Japan. The name “Spring-8” is derived from super photon ring-8GeV. It is the world’s largest third-generation synchrotron radiation facility which delivers the most powerful synchrotron radiation currently available. The synchrotron radiation X-rays were monochromatized to the wavelength of 0.65298 Å and used in this thesis work.

2.7 X-ray Photoelectron Spectroscopy (XPS) Measurements

The surface species on Si(111) wafers were investigated with a 1×10^{-9} Torr base

pressure XPS spectrometer (ULVAC-PHI, VersaProbe II) equipped with an Al K_{α} source operating at 150 W. The high-resolution scans were observed in constant energy modes at 46.95 eV pass energy. The size of an analyzed area on all the specimens was set at 220 μm x 220 μm . The Si wafer specimens for XPS measurements were prepared by immersing them in the electrolytes which had increased HF concentration and then washing them by DMC to remove the electrolytes.

2.8 Raman Spectroscopy Measurements

Raman spectroscopy measurements were conducted via a laser Raman microscope system (Nanophoton, Raman Touch-VIS-NIR). The exciting laser light wavelength was 532 nm. Raman spectra were recorded for a series of mixed electrolyte under 50 mW. The accumulation time is 2 s but repeated by 8 times. The grating line parameter is 1200 cm^{-1} and the wavenumber center is 1000 cm^{-1} . The mixed electrolytes were prepared by mixing 1 M LiPF_6 in DMC, EA, TEGDME, PC, FEC and TMS into 1 M LiPF_6 in DMSO with equal volume, i.e., 1 M LiPF_6 in DMC: DMSO (1:1 v: v), EA: DMSO (1:1 v: v), TEGDME:DMSO (1:1 v:v), PC:DMSO (1:1 v:v), FEC:DMSO (1:1 v:v), TMS:DMSO (1:1 v:v). The measurements were conducted in a super dry room with moisture less than 0.1 ppm.

Raman spectroscopy is employed to detect vibrations in molecules. It is widely used to provide the information on chemical structures and physical properties. When incident photons interact with matter, it can undergo elastic and inelastic scattering processes. Figure 2-12 is the energy diagram for the Raman process. Most molecules are present at “m” ground vibration state. When the incident photons interact with the electrons and polarize the molecules, it can make the vibration states of the molecular to some virtual states. Thereafter, the photons can be scattered with no frequency changes in elastic scattering process. This process is called Rayleigh scattering. It is the dominant process in the interaction of photons with matter. However, if the nuclear motion is induced, energy will be transferred either from the incident photons to the molecules or from the molecule to the scattered photons.¹⁵ These processes are inelastic and the energies of the scattered and incident photons are different. The energy difference of the scattered and incident photon is equal to one vibration unit. These processes are Raman scattering.

When the Raman scattering process promotes the molecules a higher energy vibration state (“m” to “n” in Figure 2-12), it is called Stokes scattering. However, if it makes the molecules shift to a lower energy state (“n” to “m” in Figure 2-12), it is anti-Stokes process.

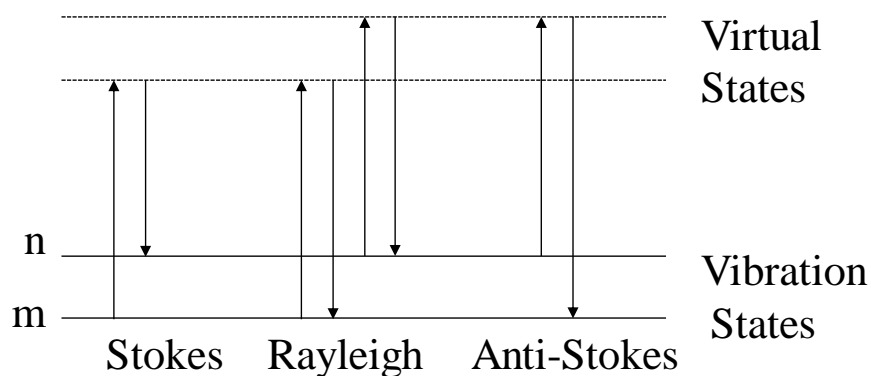


Figure 2-12 Schematic of the Rayleigh and Raman scattering processes.¹⁵

The intensities of Stokes and anti-Stokes depend on the population of the energy states of the molecules. Usually anti-Stokes scattering is weaker than Stokes scattering since the population of the energy states accord with Boltzmann distribution. Raman scattering is usually recorded only on the Stokes scattering side which has lower energy than incident photons. The Stokes scattering signal is also recorded in this thesis work.

Reference

1. Nihonyanagi, S.; Miyamoto, D.; Idojiri, S.; Uosaki, K., Evidence for epitaxial arrangement and high conformational order of an organic monolayer on Si(111) by sum frequency generation spectroscopy. *J Am Chem Soc* **2004**, *126* (22), 7034-7040.
2. Stokes, D. J., Principles of SEM. In *Principles and Practice of Variable Pressure/Environmental Scanning Electron Microscopy (VP-ESEM)*, John Wiley & Sons, Ltd: 2008; pp 17-62.
3. Reimer, L., Emission of Backscattered and Secondary Electrons. In *Scanning electron microscopy: physics of image formation and microanalysis*, Springer: 1998; pp 135-165.
4. Günter Zschornack, Physical Fundamentals. In *Handbook of X-Ray Data*, Springer: 2007; pp 9-97.
5. Goldstein, J. I., Qualitative X-Ray Analysis. In *Scanning Electron Microscopy and X-ray Microanalysis*, Springer: 1998; pp 341-363.
6. Isakozawa, S.; Kaji, K.; Tamura, K.; Zhang, X. F.; Sandborg, A.; Baba, N., The development of a new windowless XEDS detector. *J. Electron Microsc.* **2010**, *59* (6), 469-472.
7. Hovington, P.; Timoshevskii, V.; Burgess, S.; Demers, H.; Statham, P.; Gauvin, R.; Zaghbi, K., Can we detect Li K X-ray in lithium compounds using energy dispersive spectroscopy? *Scanning* **2016**, *38* (6), 571-578.
8. Kita, T.; Harada, T.; Nakano, N.; Kuroda, H., Mechanically Ruled Aberration-Corrected Concave Gratings for a Flat-Field Grazing-Incidence Spectrograph. *Appl Optics* **1983**, *22* (4), 512-513.
9. Nakano, N.; Kuroda, H.; Kita, T.; Harada, T., DEVELOPMENT OF A FLAT-FIELD GRAZING-INCIDENCE XUV SPECTROMETER AND ITS APPLICATION IN PICOSECOND XUV SPECTROSCOPY. *Appl Optics* **1984**, *23* (14), 2386-2392.
10. Terauchi, M.; Kawana, M., Soft-X-ray emission spectroscopy based on TEM - Toward a total electronic structure analysis. *Ultramicroscopy* **2006**, *106* (11-12), 1069-1075.
11. Terauchi, M.; Takahashi, H.; Handa, N.; Murano, T.; Koike, M.; Kawachi, T.; Imazono, T.; Koeda, M.; Nagano, T.; Sasai, H.; Oue, Y.; Yonezawa, Z.; Kuramoto, S., A new WDS spectrometer for valence electron spectroscopy based on electron microscopy. *JEOL News* **2012**.
12. An, Z. L.; Kamezawa, C.; Hirai, M.; Kusaka, M.; Iwami, M., Valence band density of states of Cu₃Si studied by soft X-ray emission spectroscopy and a first-principle molecular orbital calculation. *Journal of the Physical Society of Japan* **2002**, *71* (12), 2948-2952.
13. Eisebitt, S.; Luning, J.; Rubensson, J. E.; Settels, A.; Dederichs, P. H.; Eberhardt, W.; Patitsas, S. N.; Tiedje, T., Resonant inelastic soft X-ray scattering at the Si L-3 edge: experiment and theory. *J Electron Spectrosc* **1998**, *93* (1-3), 245-250.
14. Terauchi, M.; Koshiya, S.; Satoh, F.; Takahashi, H.; Handa, N.; Murano, T.; Koike, M.; Imazono, T.; Koeda, M.; Nagano, T.; Sasai, H.; Oue, Y.; Yonezawa, Z.; Kuramoto, S., Chemical State Information of Bulk Specimens Obtained by SEM-Based Soft-X-Ray Emission Spectrometry. *Microscopy and Microanalysis* **2014**, *20* (3), 692-697.
15. Smith, E.; Dent, G., Introduction, Basic Theory and Principles. In *Modern Raman Spectroscopy – A Practical Approach*, John Wiley & Sons, Ltd: 2005; pp 1-21.

Chapter 3

Investigation of Li distribution in Li-Si alloys by windowless EDS

3.1 Introduction

Si anode is one of the most promising candidates among all of the investigated anode materials for Li ion or Li air batteries due to its high energy density.¹⁻³ The Li-Si alloy structures and compositions after Si lithiation have been widely studied because of their significance to battery characteristics such as energy capacity and cycle life.⁴⁻⁷ Soft X-ray emission spectroscopy (SXES) is a powerful method for investigating Li-Si alloys by revealing the valence band structure.⁸⁻⁹ This method has been successfully applied by Aoki et al. to study the compositions of Li-Si alloys by comparison of the experimental SXES results and the calculated density of states (DOS).¹⁰ The results revealed that for electrochemically lithiated Si(111) single crystal the Li-Si alloys consist of a crystalline $\text{Li}_{15}\text{Si}_4$, an amorphous $\text{Li}_{13}\text{Si}_4$ and a mixed Li_xSi alloy layer. However, it is difficult to identify the thickness of each layer using SXES due to its low spatial resolution of approximately one micron and the exact composition of the mixed Li_xSi alloy layer cannot be fully determined.

Recently, a newly developed windowless energy dispersive spectroscopy (EDS) was used to determine Li distribution with high spatial resolution and sensitivity to light elements.¹¹⁻¹² Since conventional EDS has a thin Be metal window to isolate the specimen from the detector, the soft X-rays below 150 eV cannot be detected because of the absorption of Be window. Windowless operation with a very short working distance and new electronic devices provides improved sensitivity for the detection of low energy X-rays including Li K_α and Si $\text{L}_{2,3}$ emissions, and elemental distribution at the nanometer scale. These features enable simultaneous measurement of Li K_α , Si $\text{L}_{2,3}$ and Si K_α emissions providing information about the composition and electronic states for Li-Si alloy. However, due to the low energy resolution of windowless EDS, the Li K_α and Si $\text{L}_{2,3}$ X-ray emissions will overlap making it difficult analyze the X-ray emission

intensities. The Li K_{α} and Si $L_{2,3}$ X-ray emissions need to remain separate for analysis.

In this chapter, the composition of the Li-Si alloy was studied by combining the high-energy resolution analysis of SXES and high spatial resolution analysis of windowless EDS. The Li-Si alloy was prepared by using single crystal Si(111) lithiation under potentiostatically charging at 10 mV vs. Li/Li⁺ in 1.0 M LiPF₆ in dimethyl carbonate (DMC) solvent. The lithiation charge density was 1000 mC·cm⁻². The Li K_{α} , Si $L_{2,3}$ and Si K_{α} intensity changes were analyzed to obtain the specific thicknesses and compositions for the Li-Si alloy layers.

3.2 Results and discussion

3.2.1 Electrochemistry of Si(111) lithiation

Figure 3-1(a) shows cyclic voltammogram for the lithiation and delithiation of a Si(111) electrode measured in 1.0 M LiPF₆ in DMC solution. The potential was scanned between 2.7 and 0.01 V (vs. Li/Li⁺) at a scan rate of 1 mV·s⁻¹. The inset shows an expanded region from 2.0 to 0.1 V during the negative scan, in which two small peaks attributed to electrolyte decomposition are clearly observed starting from around 1.8 and 0.5 V. The electrolyte decomposition process has been widely studied.¹³⁻¹⁵ It is well known that a solid electrolyte interphase (SEI) is formed on the Si(111) surface as an inert film after electrolyte decomposition, which retards further electrolyte decomposition. A high cathodic current started to flow at around 100 mV, which corresponds to the lithiation of Si(111). Two broad peaks at around 300 and 500 mV, which correspond to the delithiation of Si(111) were also clearly observed. The lithiation and delithiation charges were approximately 76.6 and 62.5 mC·cm⁻², respectively. The current efficiency, which is the ratio of anodic to cathodic charge, is approximately 82%. This efficiency is consistent with other reported values of around 80% at the first cycle of Si lithiation.¹⁶⁻¹⁷ The irreversible 20% charge is due to electrolyte decomposition and some of the Li remaining in the Li-Si alloy after delithiation.

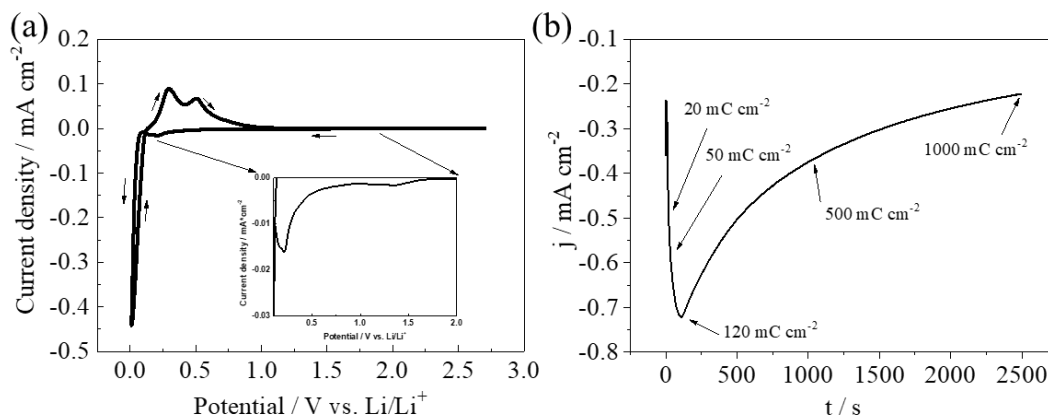


Figure 3-1 (a) Cyclic voltammogram for lithiation and delithiation of a Si(111) electrode measured in 1.0 M LiPF₆ in DMC solvent. The potential was scanned negatively from 2.7 to 0.01 V (vs. Li/Li⁺) and positively to 2.7 V (as indicated by arrows) at a scan rate of 1 mV·s⁻¹. The inset shows an expanded region from 2.0 to 0.1 V during the negative scan. (b) Current density as a function of time when the potential was stepped from 500 to 10 mV for Si(111) lithiation in 1.0 M LiPF₆ in DMC solvent.

The Li-Si alloy was prepared under potentiostatically lithiation at 10 mV. Figure 3-1(b) shows the current density as a function of time when the potential was stepped from 500 to 10 mV for Si(111) lithiation. The cathodic current density due to the lithiation of Si reached a maximum of 720 $\mu\text{A}\cdot\text{cm}^{-2}$ at first, and then decreased gradually to an almost constant value. The total lithiation charge was 1000 $\text{mC}\cdot\text{cm}^{-2}$ as indicated in Figure 3-1(b).

3.2.2 Layered Structures of Li-Si alloy

Figure 3-2(a) shows SEM image of the surface morphology of the Li-Si alloy. A large number of triangular pyramids (see inset image) of Li-Si alloy with a size of approximately 1.0 μm covered the Si(111) surface. Figure 3-2(b) shows a cross-sectional SEM image of the layered structures of the Li-Si alloy. The 1st layer consists of the triangular pyramid structures with approximately 1.0 μm height. Underneath the 1st layer there are the 2nd and 3rd layers with average thicknesses of approximately 1.5 and 2.0 μm respectively. Figure 3-3(b) shows the SXE spectra of the 1st, 2nd, 3rd and 4th layer as well as c-Si and Li metal references in the photon energy region of 50–105 eV, which covers the Si L_{2,3} (79–105 eV) and Li K _{α} (50–60 eV) emissions. Crystalline Si is a

semiconductor with a diamond structure formed by covalent bonding of sp^3 hybrid orbital. The Si $L_{2,3}$ emission peaks from c-Si were considered to be associated with low-lying Si 3s-3s bonding state at 89.6 eV, while the main peak at 92.0 eV and the shoulder at 96.0 eV originate from the p components of sp^3 hybridization.^{8, 18}

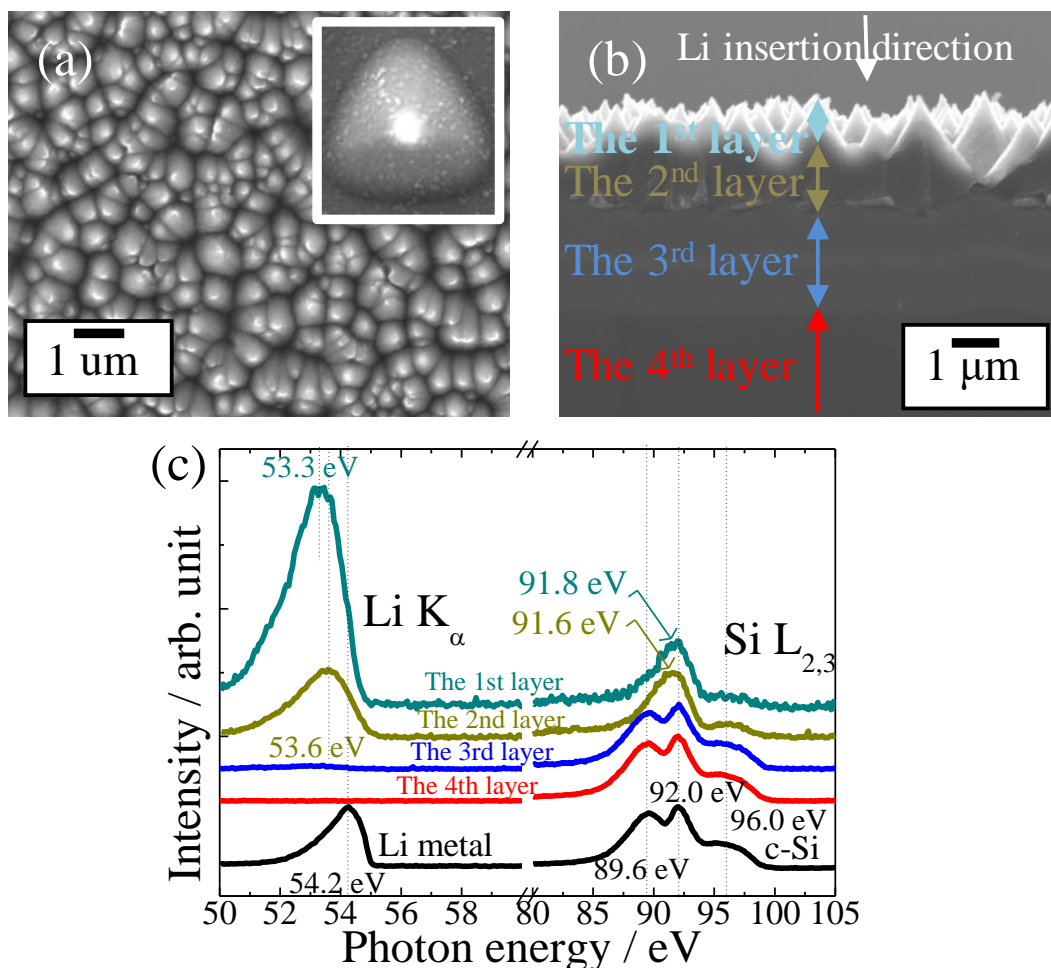


Figure 3-2 (a) Surface and (b) cross-sectional SEM images of the Li-Si alloy electrochemically prepared in 1 M $LiPF_6$ in DMC solvent. The lithiation charge density was $1000 \text{ mC}\cdot\text{cm}^{-2}$. The inset image is an enlarged Li-Si alloy pyramid. The layered structures from the cross-sectional view are presented by different color arrows. (c) SXE spectra for the 1st, 2nd, 3rd and 4th Li-Si alloy layers, as labeled in Figure 3-2(b). SXE spectra of c-Si and Li metal in the Si- $L_{2,3}$ region and the Li- K_{α} region, respectively, are shown as references. It should be noted that the intensity of the spectra was normalized by the peak at 92.0 eV.

The Si L_{2,3} band shape changed significantly in the SXE spectra for the 1st and 2nd layers, in which the dominant peaks were at 91.8 and 91.6 eV, respectively, compared with the three peaks for c-Si. The band center energies of the 1st and 2nd Li-Si alloy layers were estimated approximately 91.7 and 91.5 eV, respectively, higher than that of c-Si (90.7 eV). Here the band center energy is defined as the energy position at the half integral area of the spectrum. In the Li K_α emission spectra of the 1st and 2nd layers, single peaks were shifted to lower energies of 53.3 and 53.6 eV, respectively, compared with that of Li metal (54.2 eV). And the energy band centers of the 1st and 2nd Li-Si alloy layers were approximately 52.9 and 53.1 eV, respectively, lower than that for Li metal (53.7 eV). The observation that Si L_{2,3} shifted to higher energy and Li K_α shifted to lower energy confirmed the Si-Si bond breaking accompanied by Li-Si bond formation and electron transfer from Li to Si atoms. The SXE spectra were consistent with Aoki's work¹⁰, which revealed that the 1st layer was crystalline Li₁₅Si₄ and the 2nd layer was amorphous Li₁₃Si₄. However, it was difficult to separate the 1st and 2nd layers to obtain layer thicknesses by SXES. It was also very difficult to distinguish the 3rd layer from crystalline Si substrate of 4th layer using only SXE spectra.

3.2.3 EDS spectra analysis for Li distribution

Figure 3-3 shows EDS spectra of the c-Si (a) and Li metal (b) as references along with that of the 1st (c), 2nd (d), 3rd (e) and 4th (f) alloy layer obtained by windowless EDS. The spectra were shown in the photon energy region less than 150 eV, which cannot be detected by conventional EDS with Be metal window. The EDS spectra show the emissions of Si L_{2,3} and Li K_α accompanied by a noise peak around 4 eV. The noise peak is the cathodoluminescence that is a reverse process of photoelectric effect. The emitted photon energy is close to material working function. Here for Si and Li, the working function is ca. 4.6 and 2.9 eV. Because of the low energy resolution of EDS, the emitted photon energy was shown at 4 eV in the spectra. The inset of Figure 3-3(a) demonstrates the simultaneous detection of Si K_α and Si L_{2,3} X-ray emissions. The Si K_α emission is induced by the electron transition from Si L₂ and L₃ to Si K atomic shells, and its emission intensity is proportional to the Si concentration; however Si L_{2,3} emission is induced by the electron transition from the valence band (VB) to the Si L₂ and L₃ atomic

shells, so its emission intensity is proportional not only to the Si concentration but also affected by the VB electron state, i.e., chemical environment.¹⁹ The simultaneous detection of Si K_{α} and Si $L_{2,3}$ X-ray emissions provides the possibility to obtain both electronic and compositional information. Figure 3-3(b) shows the Li K_{α} emission spectrum. The peak position is around 54 eV, which is consistent with peak position observed in the SXE spectrum in Figure 3-2(c). Figure 3-3(c, d, e, f) show the spectra of the 1st, 2nd, 3rd, and 4th Li-Si layer, respectively. Low energy resolution leads to overlap of the Li K_{α} , Si $L_{2,3}$ peaks, and the noise peak. The noise peaks exist in all obtained spectra, and its intensity for each spectrum is same. The noise peak can be subtracted from Li K_{α} and Si $L_{2,3}$ emission peaks using Gaussian peak fitting. The deconvolution was successfully conducted to separate Li K_{α} and Si $L_{2,3}$ peaks from noise peak for all the spectra and shown in Figure 3-3.

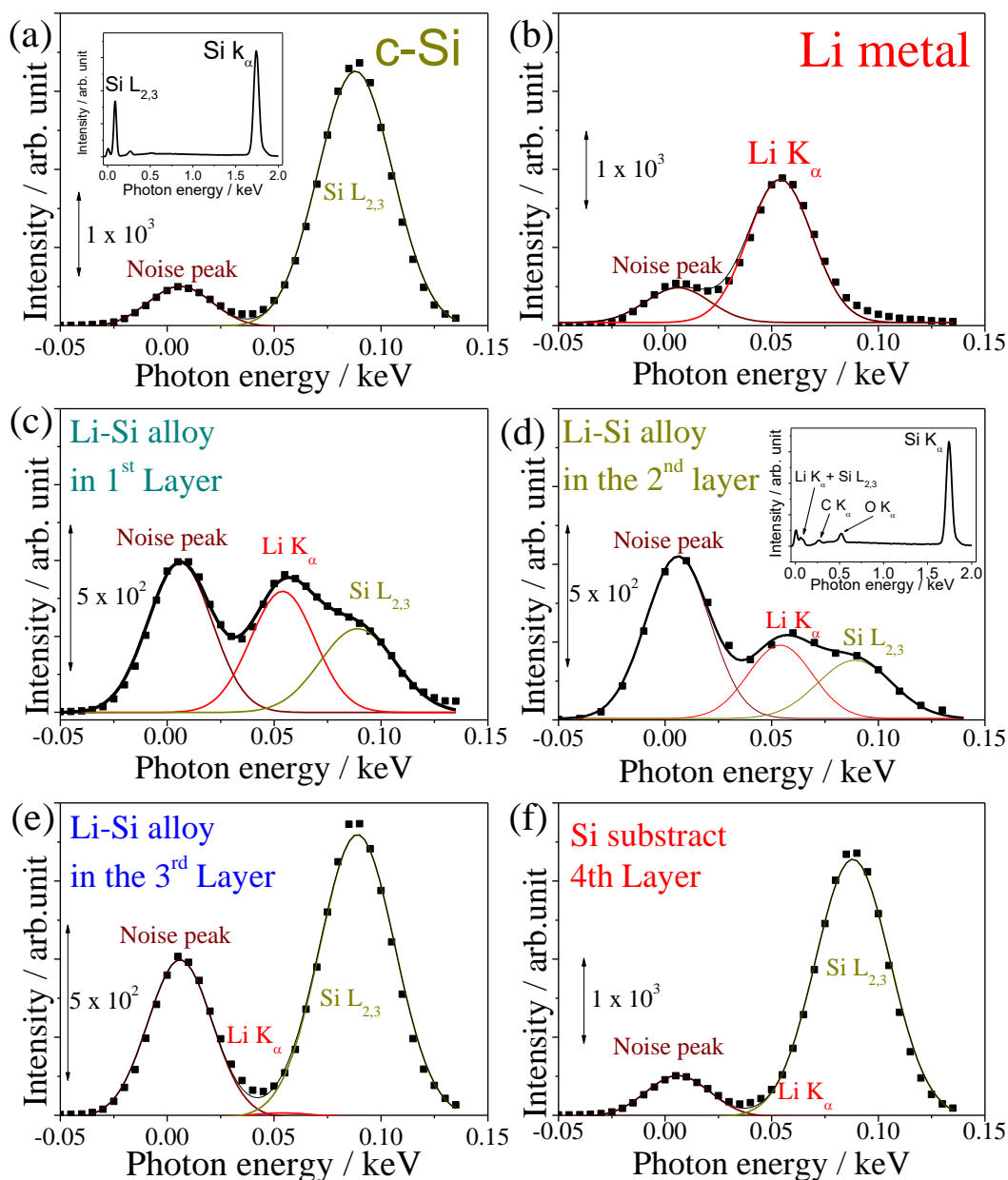


Figure 3-3 EDS spectra of the (a) c-Si and (b) Li metal as references along with that of the (c) 1st (d) 2nd, (e) 3rd and (f) 4th alloy layer. The positions of each layer were labeled in Figure 3-2(b). The accumulation time was 15 s for each spectrum. Deconvolution of the Li K α and Si L $_{2,3}$ emissions for spectra was successfully conducted by fixing the peak position at 54 and 89 eV and the full width at half maximum (FWHM) at 30 and 35 eV for Li and Si using Gaussian fitting, respectively. Here, the black points were raw data. The red line represents the Li K α emission; the dark yellow line represents the Si L $_{2,3}$ emission; the wine line represents the noise peak. The black line represents the fitting curve.

Figure 3-4(a) shows the SEM image of Li-Si alloy for EDS line scan along with the depth scale. The line scan direction was shown with color change according to Li K_{α} intensity change after windowless EDS measurements. The line scan direction was conducted from pyramid top to Si substrate. Figures 3-4(b) and (c) show the EDS depth profile along the line scan. Without deconvolution it was hard to determine Li K_{α} and Si $L_{2,3}$ emission intensity changes separately from Figure 3-4(b) due to their overlap. Figure 3-4(c) shows clearly that the Si K_{α} peak intensity increased from the 1st layer to Si substrate.

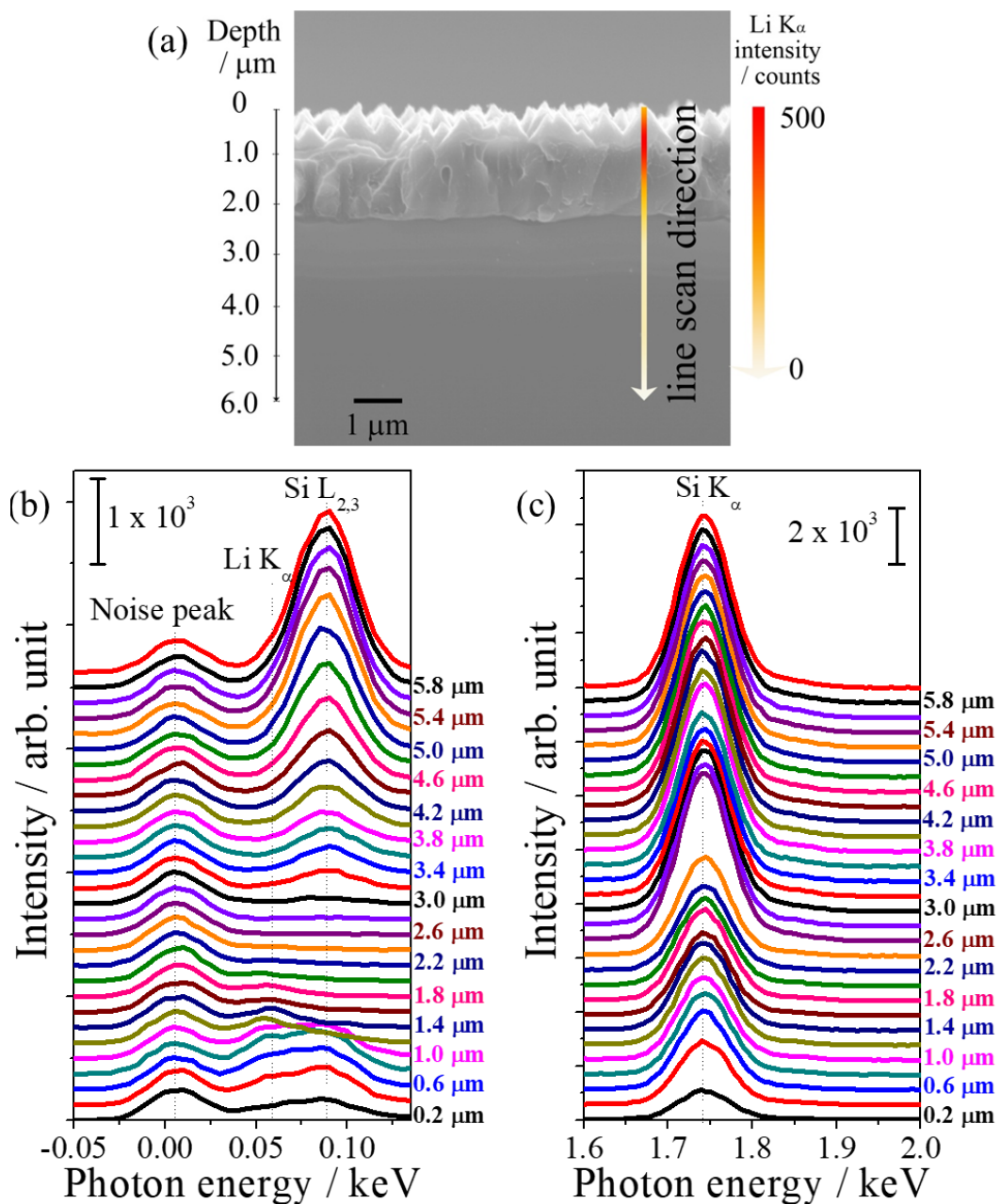


Figure 3-4 (a) Cross-sectional SEM image of electrochemically prepared Li-Si alloy for EDS line scan measurements. EDS line scan was performed by point position measurement at 200 nm intervals along the scan direction. The accumulation time was 15 s for each point measurement. The scan direction was presented by arrows with the color change to present the Li K_{α} intensity change obtained after deconvolution. (b,c) Line scan EDS spectra for the Li K_{α} , Si $L_{2,3}$ and Si K_{α} for line scan direction from a pyramid top to the Si substrate.

The deconvolution for Li K_{α} and Si $L_{2,3}$ emission peaks were conducted for EDS line scan spectra in Figure 3-4(b). Figure 3-5(a) shows the relative intensity changes of Li K_{α} , Si $L_{2,3}$ along with Si K_{α} emission intensity changes. Li K_{α} intensity was shown relative to pure Li metal intensity. Si $L_{2,3}$ and Si K_{α} intensities were shown relative to c-Si. Significant information could be obtained from these depth dependent EDS intensity changes.

First, the Li K_{α} intensity relative to pure Li metal increased to 0.25 at around 0.6 μm depth. This is due to the electron beam hitting the pyramid top, and a part of electron beam pass through the pyramid top. While the electron beam scanned from pyramid top to Si substrate, more parts of the electron beam hit the pyramid to increase the Li K_{α} emission intensity to a maximum around 0.6 μm deep in the 1st layer. Thereafter the Li K_{α} relative intensity decreased from the 1st layer to Si substrate, consistent with the Li-Si alloy layer structure, i.e., the first crystalline $\text{Li}_{15}\text{Si}_4$ and the second amorphous $\text{Li}_{13}\text{Si}_4$ layer, followed by lowly lithiated Si layer over Si substrate.¹⁰

Second, the relative Si K_{α} intensities of the 1st and 2nd layers to the 4th layer (Si substrate) are approximately 0.5, which corresponds to a mass density ratio of 0.52 for $\text{Li}_{15}\text{Si}_4$ (1.21 g cm^{-3}) to Si (2.33 g cm^{-3}) and of 0.54 for $\text{Li}_{13}\text{Si}_4$ (1.25 g cm^{-3}) to Si. This value is reasonable because Si K_{α} peak intensity is proportional to the Si atomic concentration. The relative Si K_{α} intensity of near 1.0 for the 3rd layer suggests similar Si concentration to the 4th layer (Si substrate), i.e., a very low Li concentration within the 3rd layer.

Third, the Si $L_{2,3}$ intensity relative to pure Si crystal was approximately 0.1 for the

2nd layer. This value can be explained by the effect of Li-Si bond formation on the emission intensities of Si L_{2,3}. Figure 3-5(b) shows the Li-Si bond formation by Si 3s and Li 2s electrons, and also the emission process of Si L_{2,3}. As is shown, the Si L_{2,3} intensity is affected by the valence electron since it is induced by the transition from the valence band electrons to the Si L₂ and L₃ shells.¹⁹ As explained in SXE spectra in Figure 3-2(c), the peak intensity at 89.6 eV in Si L_{2,3} for the 2nd Li-Si alloy layer decreased compared with c-Si. This peak intensity decrease was due to the decrease of the number of Si 3s orbital electrons, since 3s orbital electron participates in the Li-Si bond formation with Li 2s orbital electron as shown in Figure 3-5(b).¹⁰ In addition, the Si L_{2,3} intensity is proportional to the Si atomic concentration. Therefore, the Si L_{2,3} intensity ratio of about 0.1 for the 2nd layer was due to the Si concentration decrease by 0.5, and also the Si 3s valence electron number decrease to form Li-Si bond.

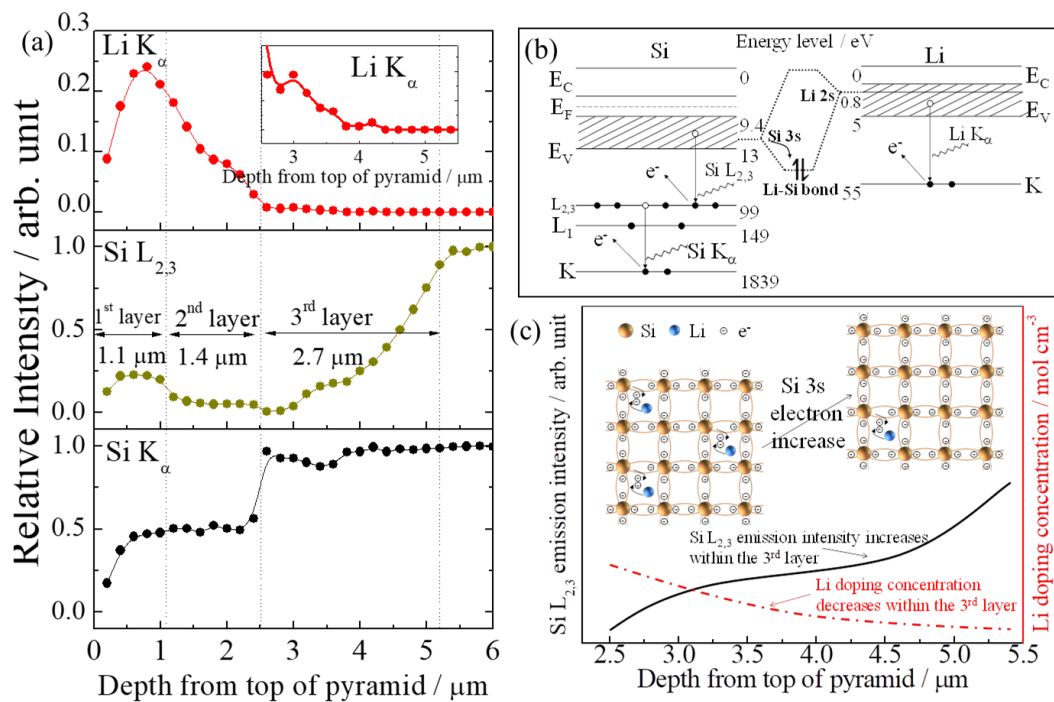


Figure 3-5 (a) Relative intensity changes of Li K_α, Si L_{2,3} and Si K_α peaks along corresponding direction after deconvolution. Li K_α intensity was shown relative to pure Li metal intensity. Si L_{2,3} and Si K_α intensities were shown relative to c-Si. (b) Energy level diagram to show the effect of Li-Si bond formation on the emission intensities of Li K_α and Si L_{2,3}. The electron binding energies for each shell of Si and Li atoms are

also included. (c) The schematic for the relationship of Li doping concentration and Si L_{2,3} emission intensity within the 3rd layer. The increase of Si L_{2,3} emission intensity was due to the increase of Si 3s electron along with Li doping concentration decrease within the 3rd layer.

Fourth, the Li K_α intensity decrease (see inset image in Figure 3-5a) and Si L_{2,3} intensity increases gradually within the 3rd layer. Figure 3-5(c) shows the schematic of Li doping concentration on Si 3s electron density. Since Si K_α intensity for the 3rd layer was similar to c-Si, the Si concentration was estimated to be similar to c-Si. In other words, the Li concentration was low within the 3rd layer. Even though Li concentration is low, it still has effect on the Si L_{2,3} intensity by affecting Si 3s electron. The gradual increase in the Si L_{2,3} intensity within the 3rd layer is due to Si 3s valence electron number increase with less Li doping as shown in Figure 3-5(c). Therefore, the gradual increase in the Si L_{2,3} intensity suggested a gradual decrease of Li doping concentration, consistent with a Li diffusion layer within the Si matrix from the 2nd layer to the 4th layer (Si substrate). This Li diffusion layer was found by windowless EDS for the first time to give the Li concentration distribution profile. In addition, the thickness for each layer can be determined by monitoring the Li K_α, Si L_{2,3} and Si K_α intensity changes as shown in Figure 3-5(a).

Two different EDS line scans were conducted as shown in Figure 3-6. Line scan 1 was conducted from pyramid top to Si substrate. Line scan 2 was conducted from near pyramid bottom to Si substrate. The two line-scans will determine where are the layer boundaries in the all Li-Si alloy, especially for the layer boundary between the 1st and 2nd layer. The layer boundary between the 2nd and 3rd layer is nearly straight observed from SEM image, however, the layer boundary between the 1st and 2nd layer is unclear from SEM image. The determination of layer boundary will help determine the Li distribution in the overall Li-Si alloy.

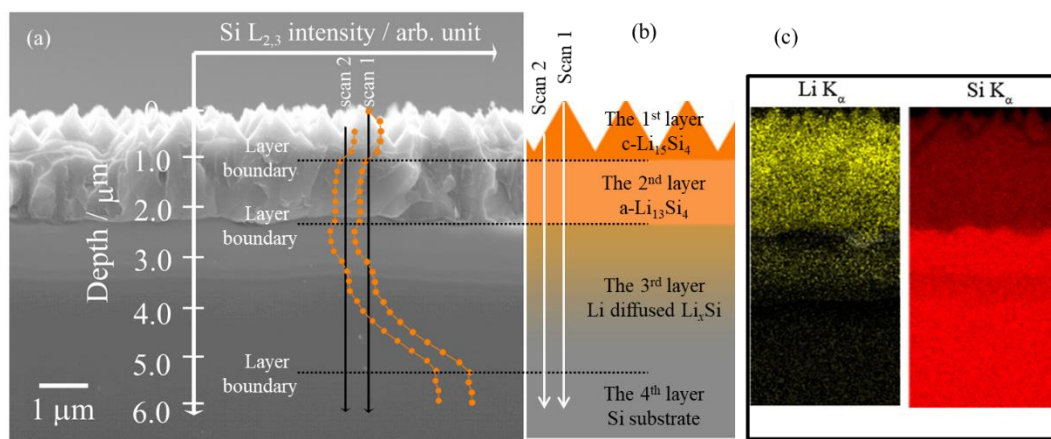


Figure 3-6 (a) Intensity changes of Si L_{2,3} along line scan direction 1 and 2 after deconvolution. Line scan direction 1 was conducted from pyramid top to Si substrate. Line scan direction 2 was conducted from near pyramid bottom to Si substrate. The boundaries between each layer were determined from Si L_{2,3} intensity change analysis. (b) Schematic illustration of Li distribution in the layered structure of the Li-Si alloy. Li concentration was represented by color intensity. (c) Li K_α and Si K_α mapping for the layered structure of the Li-Si alloy.

The Si L_{2,3} intensity changes along corresponding line scans were shown in Figure 3-6(a), It had been proved the layer boundary can be determined by monitoring the Si L_{2,3} intensity change in Figure 3-5(a). In Figure 3-6(a), the layer boundary can be determined by monitoring the Si L_{2,3} intensity change along both scan directions. In fact, the layer boundaries is determined and represented in the form of dots in each scan. Connecting the corresponding dots between each scan by a line can represent the layer boundary. Three lines can be drawn to represent the layer boundary between the 1st and 2nd layer, the 2nd and 3rd layer, the 3rd and 4th layer as shown in Figure 3-6(a). It can be found the three lines are nearly straight. Thus the layer boundaries were found to be nearly straight. The Li distribution profile in the overall Li-Si alloy can be determined.

A schematic illustration of Li distribution in the layered structure of the Li-Si alloy is shown in Figure 3-6(b). The Li K_α and Si K_α mapping for the layered structure of the Li-Si alloy in Figure 3-6(c) were consistent with the schematic illustration. The 1st layer consists of the c-Li₁₅Si₄ pyramids with the highest Li concentration; the 2nd layer consists of the a-Li₁₃Si₄ alloy with moderate Li concentration; the 3rd layer consists of the Li

diffused Li_xSi alloy with low Li concentration. The layer boundaries are nearly straight for each layer. The thicknesses are approximately 1.1, 1.4 and 2.7 μm for the 1st, 2nd and 3rd layer, respectively.

The work in this chapter had demonstrated the availability of spatially resolved Li detection in Li based battery materials using windowless EDS. It is of great significance for the development of battery materials. However, the disadvantage is that the quantitative analysis cannot be performed for Li by only using windowless EDS. Quantitative analysis are based on the truth the generated X-ray intensity is directly related to the element amount. This is not valid for Li since the generated X-ray intensity is related to not only the element amount but also the chemical states. A new quantification evaluation method need to be developed in the future to study the Li based alloys or compounds such as Li_xSn or Li_2O_2 .

3.3 Conclusions

In this chapter, windowless EDS combined with SXES was used to study the Li distribution within the Li-Si alloy with a charge density of $1000 \text{ mC}\cdot\text{cm}^{-2}$ prepared in 1.0 M LiPF_6 in DMC solvent. The overlap of Li K_α and Si $\text{L}_{2,3}$ due to the low energy resolution of EDS can be separated after deconvolution. Using windowless EDS X-ray emission intensity change analysis, the Li distribution in Li-Si alloys was obtained. In addition, it was found the Li concentration decrease gradually in the 3rd alloy layer by combining the analysis of windowless EDS and SXES. The thickness of each Li-Si layer could be also determined, especially for the 3rd layer which cannot be clearly observed by SEM.

Reference

1. Su, X.; Wu, Q. L.; Li, J. C.; Xiao, X. C.; Lott, A.; Lu, W. Q.; Sheldon, B. W.; Wu, J., Silicon-Based Nanomaterials for Lithium-Ion Batteries: A Review. *Advanced Energy Materials* **2014**, *4* (1), 23.
2. Szczech, J. R.; Jin, S., Nanostructured silicon for high capacity lithium battery anodes. *Energy & Environmental Science* **2011**, *4* (1), 56-72.
3. Kasavajjula, U.; Wang, C. S.; Appleby, A. J., Nano- and bulk-silicon-based insertion anodes for lithium-ion secondary cells. *J Power Sources* **2007**, *163* (2), 1003-1039.
4. Kang, C. S.; Son, S. B.; Kim, J. W.; Kim, S. C.; Choi, Y. S.; Heo, J. Y.; Suh, S. S.; Kim, Y. U.; Chu, Y. Y.; Cho, J. S.; Lee, S. H.; Oh, K. H., Electrochemically induced and orientation dependent crack propagation in single crystal silicon. *J Power Sources* **2014**, *267*, 739-743.
5. Son, S.-B.; Trevey, J. E.; Roh, H.; Kim, S.-H.; Kim, K.-B.; Cho, J. S.; Moon, J.-T.; DeLuca, C. M.; Maute, K. K.; Dunn, M. L.; Han, H. N.; Oh, K. H.; Lee, S.-H., Microstructure Study of Electrochemically Driven Li_xSi. *Advanced Energy Materials* **2011**, *1* (6), 1199-1204.
6. Chan, C. K.; Ruffo, R.; Hong, S. S.; Huggins, R. A.; Cui, Y., Structural and electrochemical study of the reaction of lithium with silicon nanowires. *J Power Sources* **2009**, *189* (1), 34-39.
7. Obrovac, M. N.; Christensen, L., Structural Changes in Silicon Anodes during Lithium Insertion/Extraction. *Electrochemical and Solid-State Letters* **2004**, *7* (5), A93-A96.
8. An, Z. L.; Kamezawa, C.; Hirai, M.; Kusaka, M.; Iwami, M., Valence band density of states of Cu₃Si studied by soft X-ray emission spectroscopy and a first-principle molecular orbital calculation. *Journal of the Physical Society of Japan* **2002**, *71* (12), 2948-2952.
9. Terauchi, M.; Koshiya, S.; Satoh, F.; Takahashi, H.; Handa, N.; Murano, T.; Koike, M.; Imazono, T.; Koeda, M.; Nagano, T.; Sasai, H.; Oue, Y.; Yonezawa, Z.; Kuramoto, S., Chemical State Information of Bulk Specimens Obtained by SEM-Based Soft-X-Ray Emission Spectrometry. *Microscopy and Microanalysis* **2014**, *20* (3), 692-697.
10. Aoki, N.; Omachi, A.; Uosaki, K.; Kondo, T., Structural Study of Electrochemically Lithiated Si(111) by using Soft X-ray Emission Spectroscopy Combined with Scanning Electron Microscopy and through X-ray Diffraction Measurements. *Chemelectrochem* **2016**, *3* (6), 959-965.
11. Hovington, P.; Timoshevskii, V.; Burgess, S.; Demers, H.; Statham, P.; Gauvin, R.; Zaghbi, K., Can we detect Li K X-ray in lithium compounds using energy dispersive spectroscopy? *Scanning* **2016**, *38* (6), 571-578.
12. Isakozawa, S.; Kaji, K.; Tamura, K.; Zhang, X. F.; Sandborg, A.; Baba, N., The development of a new windowless XEDS detector. *J. Electron Microsc.* **2010**, *59* (6), 469-472.
13. Vogl, U. S.; Lux, S. F.; Crumlin, E. J.; Liu, Z.; Terborg, L.; Winter, M.; Kostecki, R., The Mechanism of SEI Formation on a Single Crystal Si(100) Electrode. *J. Electrochem. Soc.* **2015**, *162* (4), A603-A607.
14. Pereira-Nabais, C.; Swiatowska, J.; Chagnes, A.; Ozanam, F.; Gohier, A.; Tran-Van, P.; Cojocar, C.-S.; Cassir, M.; Marcus, P., Interphase chemistry of Si electrodes used as anodes in Li-ion batteries. *Appl Surf Sci* **2013**, *266*, 5-16.
15. Philippe, B.; Dedryvere, R.; Allouche, J.; Lindgren, F.; Gorgoi, M.; Rensmo, H.; Gonbeau, D.; Edstrom, K., Nanosilicon Electrodes for Lithium-Ion Batteries: Interfacial Mechanisms Studied by Hard and Soft X-ray Photoelectron Spectroscopy. *Chemistry of Materials* **2012**, *24* (6), 1107-1115.
16. Chan, C. K.; Peng, H.; Liu, G.; Mellwrath, K.; Zhang, X. F.; Huggins, R. A.; Cui, Y., High-performance lithium battery anodes using silicon nanowires. *Nature Nanotechnology* **2008**, *3* (1), 31-35.
17. Holzapfel, M.; Buqa, H.; Hardwick, L. J.; Hahn, M.; Wuersig, A.; Scheifele, W.; Novak, P.; Koetz, R.; Veit, C.; Petrat, F.-M., Nano silicon for lithium-ion batteries. *Electrochim Acta* **2006**, *52* (3), 973-978.

18. Eisebitt, S.; Luning, J.; Rubensson, J. E.; Settels, A.; Dederichs, P. H.; Eberhardt, W.; Patitsas, S. N.; Tiedje, T., Resonant inelastic soft X-ray scattering at the Si L-3 edge: experiment and theory. *J Electron Spectrosc* **1998**, *93* (1-3), 245-250.
19. Skinner, H. W. B., The soft X-ray spectroscopy of solids I. K- and L-emission spectra from elements of the first two groups. *Philos. Trans. R. Soc. Ser. A-Math. Phys. Sci.* **1940**, *239* (801), 95-134.

Chapter 4

Lithiation Process Study for Single Crystal Silicon

4.1 Introduction

Higher energy and power in Li-based secondary batteries are required for electrical vehicles to build more efficient society. One key to enhance the energy and power in Li-based secondary batteries is to find a suitable anode material that had high energy and power density. Among all the studied anode materials, Si has high theoretical capacity of $3600 \text{ mAh}\cdot\text{g}^{-1}$ when a fully alloyed $\text{Li}_{15}\text{Si}_4$ phase forms at room temperature, which is almost ten times higher than that for graphite. However, volume expansion close to 400% hinders the application of such a Si anode in batteries.¹⁻³ Large volume changes cause significant internal stress within the Si anode. The internal stress will cause the Si anode fracture, which lead to rapid reducing in the battery capacity. Nano Si, such as nanoparticles or nanowires, has proven to be effective for the improvement of battery cycle performance.⁴⁻⁶ The improvement is due to that nano Si has enough buffer space between the particles for the volume expansion. Besides the volume expansion problems, there are still many remained issues for Si anode such as low power (low current density) due to low Li diffusion coefficient in Si. It is important to study the alloying mechanism of Li with Si. The structure and composition of Li-Si alloys after Si lithiation need to be investigated, since they determine the battery characteristics such as the energy capacity and cycle life.

The Li-Si alloy compositions have been widely studied because of their significance with respect to the battery characteristics such as energy capacity and cycle life. X-ray diffraction (XRD) is the most applied method to reveal the structure and composition of Li-Si alloys. Obrovac⁷ studied structural changes during the Si lithiation process at room temperature using XRD, and determined that the $\text{Li}_{15}\text{Si}_4$ phase crystallized from highly lithiated amorphous Si. Thereafter, several groups⁸⁻¹¹ also reported crystalline $\text{Li}_{15}\text{Si}_4$ formation from highly lithiated amorphous Si. However, there is still some controversy about if there is crystalline $\text{Li}_{15}\text{Si}_4$ phase since others reported only amorphous phases.¹²⁻

¹³ It is known to be difficult to detect crystalline Li-Si alloy from XRD measurements if the amount of the crystalline phase is small. Synchrotron XRD can detect small amount of the crystalline phase due to its more significant sensitivity than normal XRD. In addition, soft X-ray emission spectroscopy (SXES) is a powerful method for investigating Li-Si alloys. A combination of SXES and scanning electron microscopy (SEM) can reveal the structure and composition of the Li-Si alloys. The valence band (VB) structure of Li-Si alloys is determined by the excitation of inner shell electrons and emission of soft X-rays when electrons are transferred from the VB to the inner orbitals.¹⁴⁻¹⁵ SXES has been successfully applied by Aoki et al. to investigate the composition of Li_xSi alloys by comparison of the experimental SXES results with the calculated density of states (DOS).¹⁶ Combined with synchrotron XRD, the SXES results revealed that the Li-Si alloy layer was formed by electrochemically lithiated Si(111) single crystals. However, it is difficult from SXES to identify nanostructures due to its low spatial resolution, because the electron beam size is approximately one micron.

Recently, windowless energy dispersive spectroscopy (EDS) was used to determine Li elements with high spatial resolution and sensitivity to light elements.¹⁷ Windowless operation with a very short working distance and new electronic devices provide improved sensitivity for the detection of low energy X-rays, including Li K_α and Si $\text{L}_{2,3}$ emissions. These features enable the measurement of Li K_α , Si $\text{L}_{2,3}$ and Si K_α lines simultaneously to obtain the information on the composition and electronic states. It had been applied in Chapter 3 to determine the Li distribution in the Li-Si alloys. Therefore, the combination of high energy resolution analysis by SXES and high spatial resolution analysis by windowless EDS could be used to study the lithiation process of single crystal Si, by determining the structure, composition and electronic state changes of the Li-Si alloys.

In this chapter, the single crystal Si(111) lithiation process was studied. Five Li-Si alloys were electrochemically prepared under potentiostatically charging at 10 mV vs. Li/Li^+ . The charge densities were $20 \text{ mC}\cdot\text{cm}^{-2}$, $50 \text{ mC}\cdot\text{cm}^{-2}$, $120 \text{ mC}\cdot\text{cm}^{-2}$, $500 \text{ mC}\cdot\text{cm}^{-2}$ and $1000 \text{ mC}\cdot\text{cm}^{-2}$. The structure and composition changes were investigated using SEM and SXES. The Li distribution changes were investigated using windowless EDS.

Although the formation of crystalline $\text{Li}_{15}\text{Si}_4$ and amorphous $\text{Li}_{13}\text{Si}_4$ alloy phases is determined, the process for lithiation of single crystal Si remains unclear with respect to how the Li_xSi alloys nucleate and grow. On the other hand, the in-situ synchrotron XRD was conducted to study the lithiation process. The potential was stepped to 0.01 V for lithiation, and then stepped to 2.0 V for delithiation. During the lithiation-delithiation, the intensity of the peak relative to $\text{Li}_{15}\text{Si}_4(222)$ was recorded. Lithium insertion is an anisotropic process; therefore, it is preferable to use a single crystal with a specific crystalline orientation to determine the Si lithiation process. Thus, a single crystal Si(111) wafer was used for this investigation.

4.2 Results and Discussion

4.2.1 Si(111) Lithiation Process under Potentiostatic Charging

The lithiation process of Si(111) was investigated by measuring five Li-Si alloys as indicated in Figure 3-1(b). Here, 20 and 50 $\text{mC}\cdot\text{cm}^{-2}$ Li-Si alloys were prepared by stopping the charging process before the lithiation current reached its peak, a 120 $\text{mC}\cdot\text{cm}^{-2}$ Li-Si alloy was prepared at around the peak current, whereas 500 and 1000 $\text{mC}\cdot\text{cm}^{-2}$ Li-Si alloys were prepared after the peak current.

As analyzed in Chapter 3, the 1000 $\text{mC}\cdot\text{cm}^{-2}$ Li-Si alloys consist of the 1st layer of crystalline $\text{Li}_{15}\text{Si}_4$, the 2nd layer of amorphous $\text{Li}_{13}\text{Si}_4$, the 3rd layer of Li diffusion Li_xSi layer and the 4th layer of Si substrate. Through determining the morphology by SEM for the Li-Si alloys under increased charging time, the layer structure formation process can be determined.

Figure 4-1 shows surface and cross-sectional SEM images of the five Li-Si alloys. Figures 4-1(a) and 4-1(b) show the initial formation of triangular pyramid structures of Li-Si alloy on the Si(111) surface at the beginning before the lithiation current reached its maximum value. As the lithiation progressed, the Li-Si alloy pyramid grew gradually to cover almost the entire Si surface (Figure 4-1(c)) at around the peak lithiation current. The pyramid remained unchanged after the peak lithiation current, as shown in Figures 4-1(d) (500 $\text{mC}\cdot\text{cm}^{-2}$) and 4-2(e) (1000 $\text{mC}\cdot\text{cm}^{-2}$).

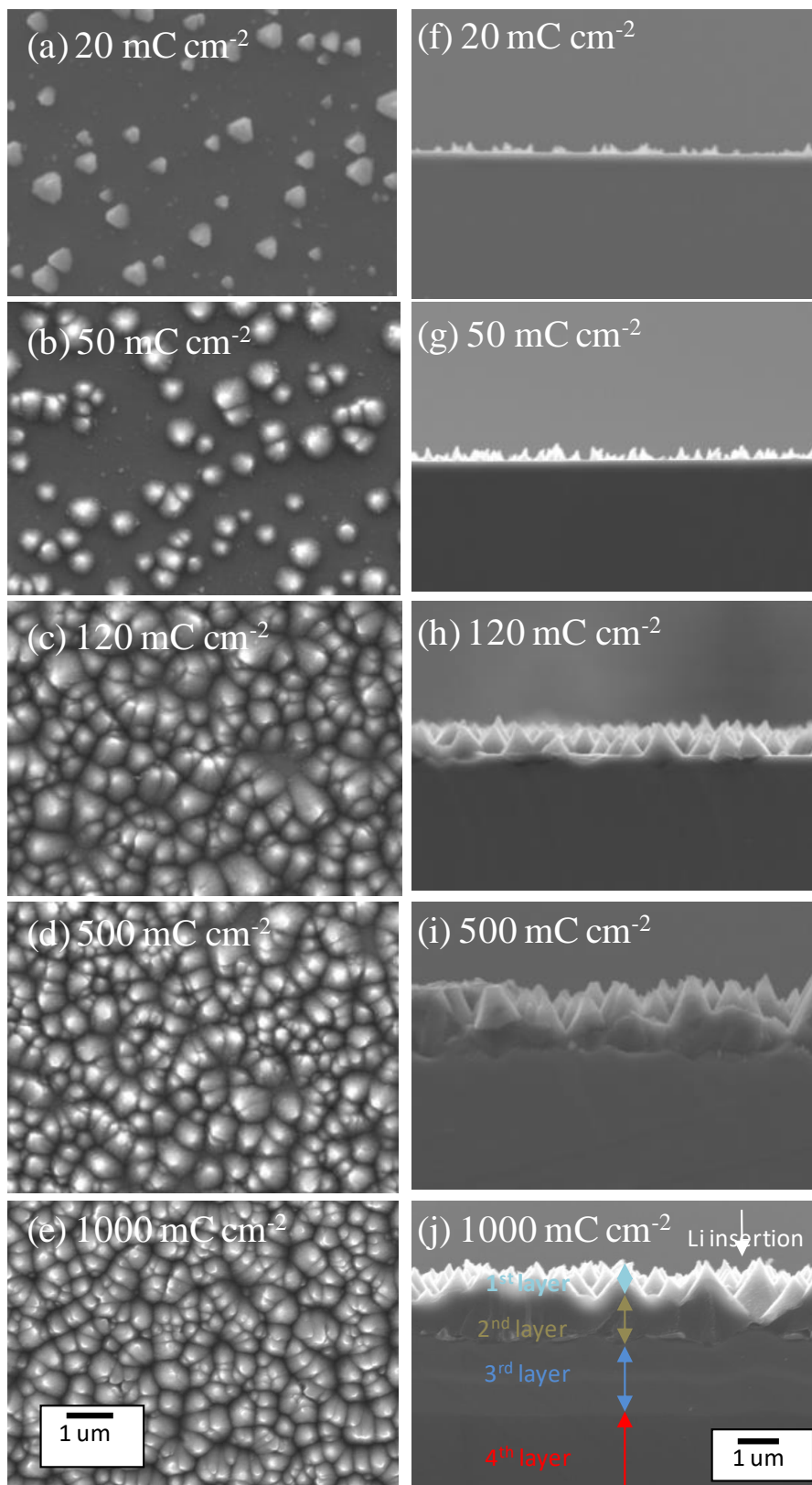


Figure 4-1. (a-e) Surface and (f-j) cross-sectional SEM images of electrochemically prepared Li-Si alloys. The charge densities for the Li-Si alloys increased.

Figures 4-1(f)-(j) show cross-sectional SEM images of the Li-Si alloys. Before the lithiation current reached its maximum value, the pyramid began to grow into electrolyte side as shown in Figures 4-1(f)-(h). After the peak current, a layer beneath the pyramid structures began to grow, as shown in Figures 4-1(i) ($500 \text{ mC}\cdot\text{cm}^{-2}$) and 4-2(j) ($1000 \text{ mC}\cdot\text{cm}^{-2}$). The layer structure was indicated in Figure 4-1(j). These results suggest that the lithiation charge leads to the growth of the 1st pyramid layer before the lithiation current reached its maximum value, while the subsequent lithiation charge lead to the growth of the 2nd layer after the lithiation current maximum.

The SEM observation only provided the structural change of the Li-Si alloys during Si lithiation. It cannot be used to determine the composition change. SXES was used to determine the composition change during the Si lithiation.

Figures 4-2 and 4-3 show the change in the Li K_{α} and Si $L_{2,3}$ SXE spectra during Si(111) lithiation for the 1st and 2nd layer, respectively. The low intensity of the Li K_{α} peak for the 3rd layer meant it was difficult to compare SXE spectra for the 3rd layer for different Li-Si alloys.

First, the peak positions of the Li K_{α} emission from the 1st layer were shifted to lower energy, as shown in Figure 4-2(a). During initial lithiation (20 and $50 \text{ mC}\cdot\text{cm}^{-2}$), the peak position was approximately 53.6 eV , which was the same as that for the 2nd layer of $1000 \text{ mC}\cdot\text{cm}^{-2}$ Li-Si alloy, therefore, the initial pyramid structures were more likely to be an amorphous $\text{Li}_{13}\text{Si}_4$ phase. The electron beam size (about $1.0 \mu\text{m}$) is larger than the pyramid size for the 20 and $50 \text{ mC}\cdot\text{cm}^{-2}$ Li-Si alloys, therefore, the Si $L_{2,3}$ emission peak originates from both c-Si and the Li-Si alloy. It was suggested that the amorphous Li-Si alloy was formed at the beginning of the lithiation process. However, around the cathodic peak current, the pyramid structures cover the entire surface, and the SXE spectra show a significant change between 50 and $120 \text{ mC}\cdot\text{cm}^{-2}$, i.e., the intensity of the peaks at 89.6 and 96.0 eV in the Si $L_{2,3}$ emission spectrum decreased significantly and the peak in the Li K_{α} emission spectrum shifted to 53.4 eV . These results can be explained in two ways: First, coverage of the Si surface by the Li-Si alloy preventing the detection of the signal from the c-Si, and a change from amorphous to crystalline $\text{Li}_{15}\text{Si}_4$. As lithiation progressed, the Li K_{α} peak position shifted slightly from

53.4 eV for the 120 mC·cm⁻² Li-Si alloy to 53.3 eV for the 1000 mC·cm⁻² Li-Si alloy, which suggested the complete formation of a crystalline phase. Therefore, the composition change in the 1st layer structure was confirmed by the change in the SXE spectra, that is, the 1st layer grew and transferred from amorphous to crystalline Li₁₅Si₄ alloy phase.

SXS spectra were also obtained for the 2nd layer in Figure 4-3. There was no formation of a 2nd layer before the lithiation cathodic current reached its maximum; therefore, there was no Li K_α emission observed for the 20, 50 and 120 mC·cm⁻² Li-Si alloys in Figure 4-3(a). The Si L_{2,3} emission suggests that this layer beneath the pyramid structures was similar to c-Si. However, when the 2nd layer began to grow to a bigger thickness, as indicated by SEM (500 and 1000 mC·cm⁻²), the Li K_α emission appeared. The Li K_α peak position was approximately 53.6 eV for both the 500 and 1000 mC·cm⁻² Li-Si alloys, and the Si L_{2,3} band center was estimated to be 91.5 eV. As previously described, this layer is amorphous Li₁₃Si₄. Combining the results of the SXE spectra for the 1st and 2nd layers, it can be concluded that the amorphous Li₁₅Si₄ pyramid structures nucleate and grow on the surface until the lithiation current reached its maximum, and then transform into crystalline Li₁₅Si₄, while the amorphous Li₁₃Si₄ alloy in the 2nd layer starts to grow only after the peak current is reached.

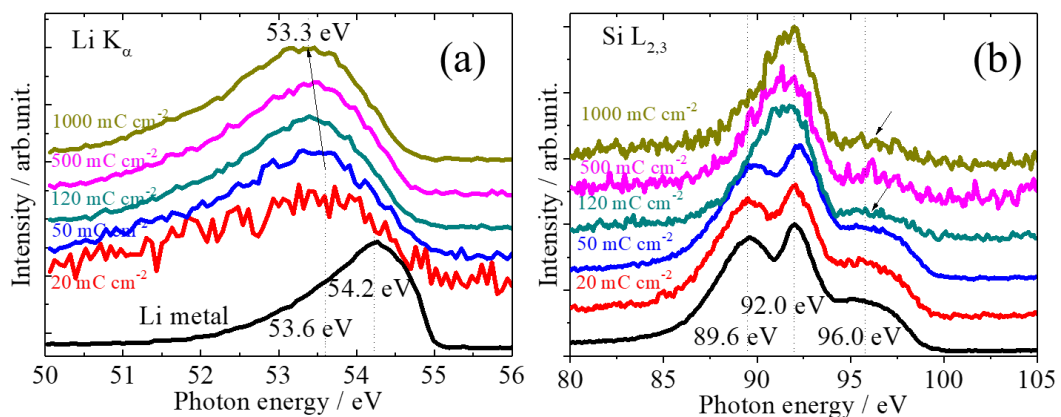


Figure 4-2 SXE spectra of the 1st layer for Li-Si alloys with different charge densities. SXE spectra for (a) Li metal in the Li K_α region and (b) c-Si in the Si L_{2,3} region are shown as references. The spectra were normalized by the peak at 92.0 eV.

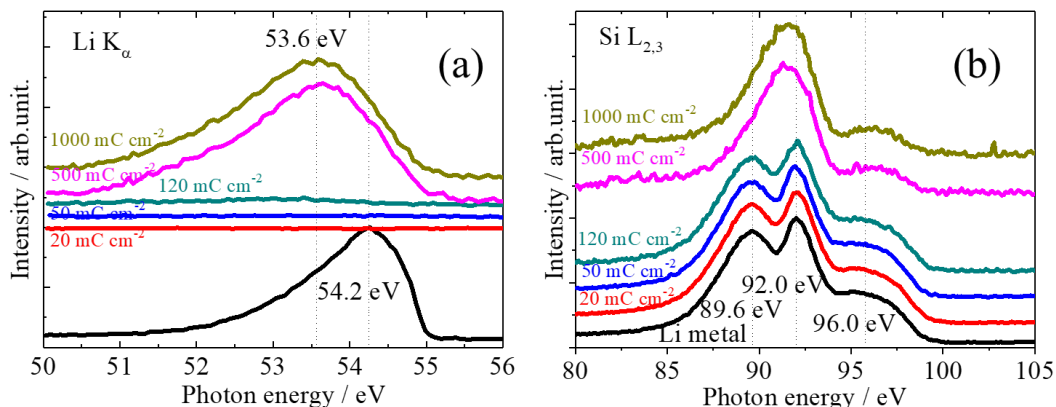


Figure 4-3. SXE spectra of the 2nd layer from the electrochemically prepared Li-Si alloys with different charge densities. SXE spectra for (a) Li metal in the Li K region and (b) c-Si in the Si L_{2,3} region are shown as references. The spectra were normalized by the peak at 92.0 eV.

SEM and SXES cannot identify the layer thickness of the 3rd Li diffused Li_xSi alloy layer, therefore, it was difficult to distinguish the changes in the thickness of the different layers during Si lithiation. Based on the analysis in Chapter 3, windowless EDS could indicate Li distribution and layer thickness of each distinct layer by comparing the intensity of the Li K_α, Si L_{2,3} and Si K_α peaks. Especially the Si L_{2,3} peak, can provide information on the 3rd Li diffused layer.

Figure 4-4 shows the Li K_α, Si L_{2,3} and Si K_α emission intensity change of Li-Si alloys with different charge densities. Since Li K_α emission appears at increased depth with increased charge density, it is clear that Li inserted Si gradually. The gradual Li insertion into Si also causes the Si K_α and Si L_{2,3} emission decrease gradually at increased depth. From windowless EDS analysis in Chapter 3, Li alloying with Si cause the appearance of Li K_α emission and decrease of Si K_α and Si L_{2,3} emission. Thus, the Li K_α, Si L_{2,3} and Si K_α emission intensity change behavior with increased charge density are reasonable.

The Li K_α and Si K_α emission can reflect the 1st and 2nd layer growth. However, they cannot reflect the 3rd layer alloy information, since the emission intensities of both in the 3rd layer were almost same to that for c-Si. Only Si L_{2,3} emission can reflect the 3rd layer growth with increased intensity within the 3rd layer.

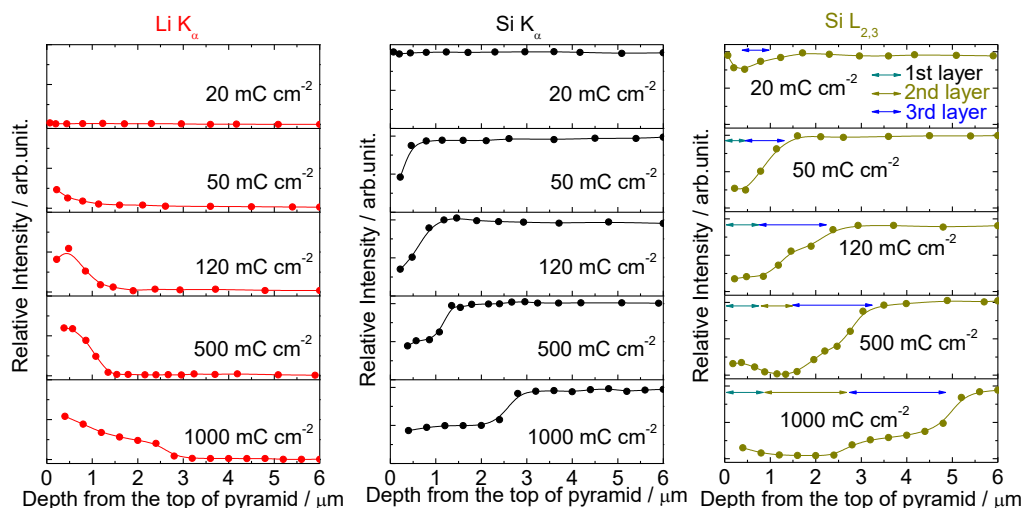


Figure 4-4. Line scan Li K_{α} , Si $L_{2,3}$ and Si K_{α} emission intensity of Li-Si alloys with different charge densities. The thicknesses determined from the intensity change are shown by arrows with different colors. The 1st, 2nd and 3rd layers are shown in dark cyan, dark yellow and blue, respectively.

From the depth profile of the Si $L_{2,3}$ peak intensity, the thicknesses of each layer could be easily determined, as indicated by the length of the arrows. The changes in the thickness of each layer were presented in Figure 4-5. First, the thickness of the 1st layer increased until the cathodic current reached its maximum and remained almost constant at approximately 1.0 μm . Similar growth behavior was observed for the 3rd layer with a greater thickness of approximately 2.6 μm . The 2nd layer grew only after the peak current was reached, becoming approximately 1.5 μm for the 1000 $\text{mC}\cdot\text{cm}^{-2}$ Li-Si alloy. This distinct change in the layer thicknesses could only be observed using windowless EDS. By combining SEM observations and windowless EDS measurements, the electrochemical lithiation process could be described as simultaneous the 1st layer and the 3rd layer growth during initial lithiation, with a constant thickness maintained after the peak lithiation current was reached, and subsequent the 2nd layer growth.

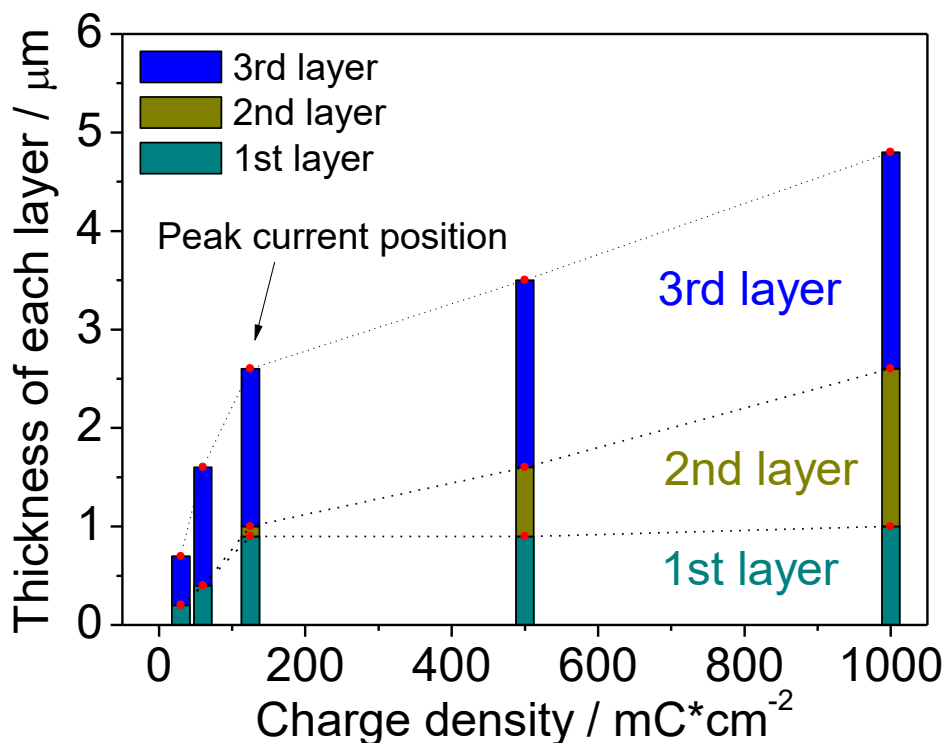


Figure 4-5. Change in the thickness of different layers relative to the charge density determined from the Si $L_{2,3}$ intensity in Figure 4-4.

4.2.2 In-situ Synchrotron XRD Study for Si Lithiation

The formation of $c\text{-Li}_{15}\text{Si}_4$ after Si(111) lithiation had been determined using ex-situ synchrotron XRD and SXES. Ex-situ SXES revealed a transformation trend from amorphous to crystalline phase $\text{Li}_{15}\text{Si}_4$ during Si lithiation, but it did not reveal if the crystalline was possible to form at beginning of Si lithiation. This is because SXES detection area is large than $1.0\ \mu\text{m}$, but the pyramid size is smaller than $0.1\ \mu\text{m}$ (Figure 4-1a) at beginning of Si lithiation, which makes the SXE spectra contain most signal from the Si substrate but not the pyramid (The spectra of Si $L_{2,3}$ are almost same for $20\ \text{mC}\cdot\text{cm}^{-2}$ Li-Si alloy and Si substrate). In other words, the possible formation of crystalline phase $\text{Li}_{15}\text{Si}_4$ at beginning of Si lithiation cannot be well revealed by SXE spectra. On the other hand, it had been reported the metastable crystalline phase $\text{Li}_{15}\text{Si}_4$ may become unstable when the ambient condition changes.¹¹ If the crystalline phase $\text{Li}_{15}\text{Si}_4$ become unstable, ex-situ SXES may reveal misleading information. Compared with ex-situ method, in-situ synchrotron XRD can reveal more real-time information

about the Si lithiation.

Figure 4-6(a) is the schematic for out-of-plane XRD measurement. The intensity of the peak relative to $\text{Li}_{15}\text{Si}_4(222)$ was recorded during Si lithiation and delithiation. Figure 4-6(b) shows the lithiation-delithiation current flow as a function of time. Before the charge started, the crystal orientation of Si(111) need to be found and fixed in favor of looking for c- $\text{Li}_{15}\text{Si}_4$. It took about 6 hours to finish adjusting the crystal orientation. After the crystal orientation adjustment, the lithiation-delithiation process started. The starting time shown in Figure 4-6(a) is relative to the starting of lithiation-delithiation process. When the charge started at 0.01 V, a very large cathodic current of about -2.1 mA started to flow and then decreased with time. Since the electrolyte layer need to be thin enough for the X-ray penetration to reach the Si(111) wafer, the Li ion source in the electrolyte is limited. During the lithiation, the Li ion source in the thin electrolyte layer was consumed, which resulted in the decrease of the current controlled by Li ion diffusion. After 600 min, the charge stopped and the potential was hold at OCP of 200 mV for 120 min. Before charging, the OCP is around 2.7 V. After charging, the OCP changed to 200 mV, which indicated Si had alloyed with Li. Thereafter, the discharge started under potentiostatically at 2.0 V. A greatly large anodic current of 6.5 mA started to flow and then decreased with time. The Li-Si alloy delithiated to form Si and Li.

During the lithiation and delithiation process, the X-ray diffraction intensities were recorded. Figure 4-6(c) shows azimuthal ϕ dependent X-ray diffraction intensity at $2\theta = 24.60$ (c- $\text{Li}_{15}\text{Si}_4$ (222)) at 0-60 min, 233-300 min and 653-720 min. The time was corresponding to Figure 4-6(b). According to previous work¹⁶, the XRD pattern had confirmed the formation of c- $\text{Li}_{15}\text{Si}_4$ epitaxially grown on Si(111) substrate. As observed from Figure 4-6(c), the diffraction peak relative to c- $\text{Li}_{15}\text{Si}_4$ (222) were displayed at several azimuthal degrees, which suggested it depend on the X-ray reaching positions on the sample. This is due to the growth position of c- $\text{Li}_{15}\text{Si}_4$ (222) on the Si substrate or some mismatch of c- $\text{Li}_{15}\text{Si}_4$ (222) with the Si(111) substrate as shown in Figure 4-7(a). Some places have no c- $\text{Li}_{15}\text{Si}_4$ formation, so there is no diffraction peak. After charging, the azimuthal dependent peak number relative to c- $\text{Li}_{15}\text{Si}_4$ (222) increased, and the peak intensity increased either. This suggested more c- $\text{Li}_{15}\text{Si}_4$ formed on the substrate.

The more $c\text{-Li}_{15}\text{Si}_4$ formation was consistent with SXES results as shown in Figure 4-2(a), which also revealed more $c\text{-Li}_{15}\text{Si}_4$ formation after lithiation.

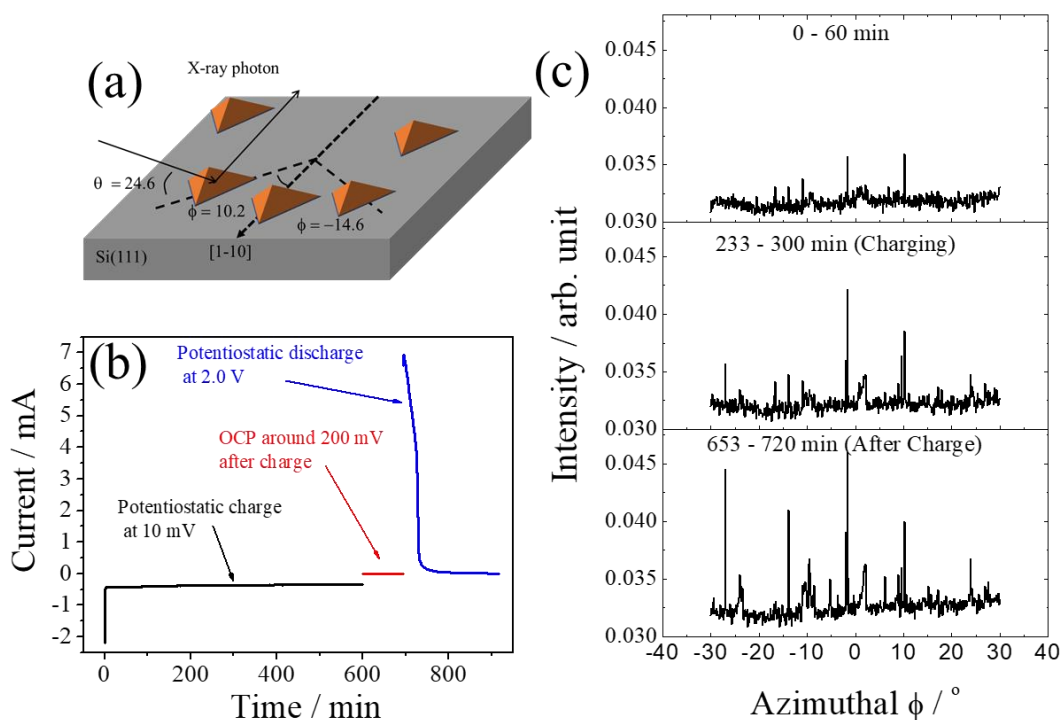


Figure 4-6. (a) Schematic for the in-situ XRD measurement. (b) Current density as a function of time when the potential was stepped to 0.01 V for Si(111) lithiation, and then stepped to 2.0 V for Si(111) delithiation. (c) Azimuthal ϕ dependent X-ray diffraction intensity at $2\theta = 24.6^\circ$ (the peak is relative to $c\text{-Li}_{15}\text{Si}_4$ (222)) at 0-60 min, 233-300 min and 653-720 min. The time was corresponding to Figure 4-6(b).

Figure 4-7 shows XRD pattern changes relative to $c\text{-Li}_{15}\text{Si}_4$ (222) during the charge-discharge process when $\phi = 10.2$, and the intensity change relative to Si(222). The pyramid had formed at $\phi = 10.2$ during 0-60 min, so its growth corresponding to X-ray intensity change was monitored. As is observed, the intensities of diffraction peak corresponding to $c\text{-Li}_{15}\text{Si}_4$ (222) increased after Si lithiation and decreased after delithiation. This confirmed the growth of $c\text{-Li}_{15}\text{Si}_4$ after lithiation and dissolved after delithiation. The peak of $c\text{-Li}_{15}\text{Si}_4$ (222) become broader after charge, which suggest the average size of $c\text{-Li}_{15}\text{Si}_4$ become smaller. According to the SXES results, the $a\text{-Li}_{15}\text{Si}_4$

of small size will transform to c-Li₁₅Si₄. In other words, more amount of smaller c-Li₁₅Si₄ will form from a-Li₁₅Si₄ after charge, which lead to a smaller average size of c-Li₁₅Si₄. Therefore, the peak of c-Li₁₅Si₄(222) become broader after charge because the average size of c-Li₁₅Si₄ become smaller. The peak intensity of c-Li₁₅Si₄(222) increase after charge because the amount of c-Li₁₅Si₄ increases. On the other hand, the intensities of diffraction peak corresponding to Si(222) decreased after charging and increased after discharging. This is due to Si alloying with Li after lithiation and dealloying with Li after delithiation. The peak of Si(222) become broader after charge. This is because Si substrate is a big single crystal and its crystallinity was broken after charge since more Si was alloyed with Li to form Li-Si alloy.⁸ According to the XRD intensity change of c-Li₁₅Si₄(222) and Si(222) during the charging and discharging process, it can be summarized that c-Li₁₅Si₄ formed after charge and dissolved after discharge; Si was alloyed with Li to form Li-Si alloy after charge and dealloyed after discharge.

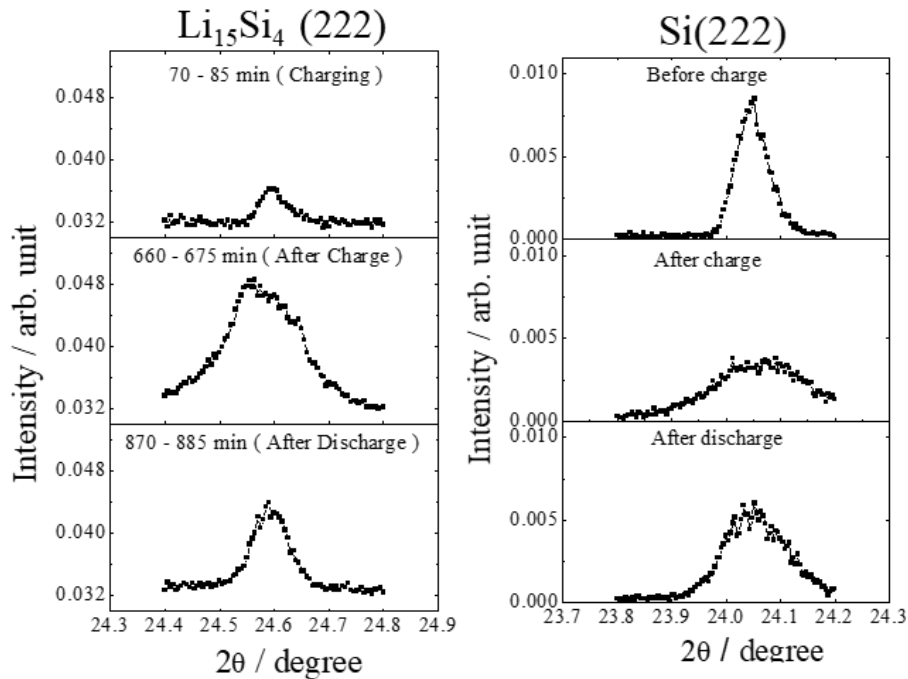


Figure 4-7. Out-of-plane XRD pattern intensity changes relative to c-Li₁₅Si₄(222) at $\phi = 10.2$, and the intensity change relative to c-Li₁₅Si₄ (222) during lithiation and delithiation.

Figure 4-8 shows the surface and cross-sectional SEM images of Li-Si alloys after

in situ measurements. As been observed, there are Li-Si alloy pyramid on the Si substrate, but the Si surface is not all covered by Li-Si alloy pyramid. This is because the Li ion source in the thin electrolyte is not enough to support the Li-Si alloy grow to cover the Si substrate, and finally does not show a similar layered structure as shown in Figure 4-1e. The structure is similar to initial Si lithiation as shown in Figure 4-1a. The Li-Si alloy remained on the Si surface after delithiation. This explained there still had diffraction intensity relative c-Li₁₅Si₄ (222).

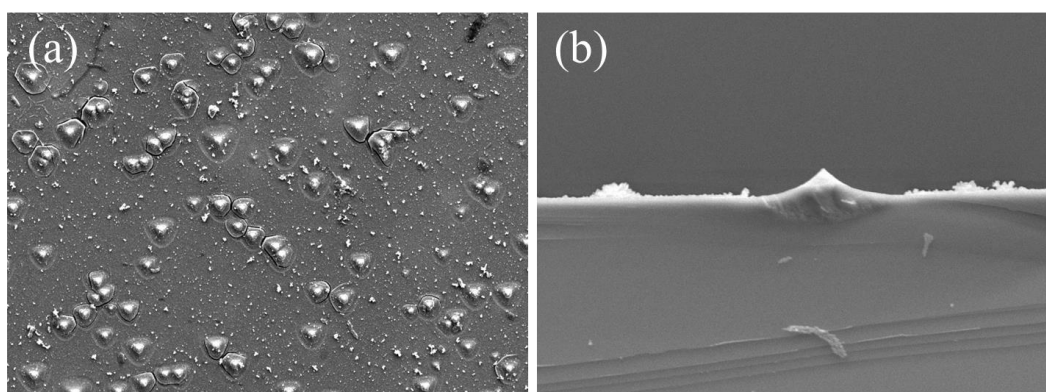


Figure 4-8. (a) Surface and (b) cross-sectional SEM images of Li-Si alloy after in-situ measurements.

In short summary, the in-situ synchrotron XRD study for Si lithiation was conducted. The diffraction peak intensity relative to c-Li₁₅Si₄ (222) increased after lithiation and decreased after delithiation which confirmed the formation of c-Li₁₅Si₄ and its dealloying. The Si(222) diffraction peak intensity decreased after lithiation and increased after delithiation, which determined the reaction of c-Si with Li and a-Si formation after delithiation. The in-situ synchrotron XRD revealed that the crystalline Li₁₅Si₄ phase can form at the beginning of Si lithiation, although the SXES results revealed there was only amorphous Li₁₅Si₄ phase formation. This is possible due to the SXES detection beam size is much larger than pyramid size that make SXES signal most came from Si substrate, and also possible due to the metastable crystalline Li₁₅Si₄ phase transformed to amorphous phase during the ex-situ SXES detection. Combined with SXES and in-situ synchrotron XRD, we can summary that there are the formations of amorphous and crystalline Li₁₅Si₄ phase at the beginning of Si lithiation, and amorphous transformed

into crystalline phase when Si has more lithiation. The synchrotron XRD revealed the formation of crystalline $\text{Li}_{15}\text{Si}_4$ phase at the beginning of Si lithiation, which SXES did not reveal but determined the formation of amorphous $\text{Li}_{15}\text{Si}_4$ phase. The mechanism of transformation from amorphous to crystalline $\text{Li}_{15}\text{Si}_4$ phase needs to be further studied such as controlling the lithiation potential or lithiation degree, although it is known that it can be due to a possible energy favorable mechanism.

4.2.3 Diffusion Controlled Instantaneous Nucleation and Growth of Si(111) Lithiation

In order to determine the kinetics of nucleation and growth during the lithiation of Si(111), the potentiostatically charging method was employed at different overpotential. Figure 4-9(a) shows the current density as a function of time of Si(111) lithiation in 1.0 M LiPF_6 in DMC after the electrode potential was stepped to the lithiation potential region at 10, 30, 50 and 70 mV. The cathodic current due to electrochemical lithiation was observed. The current density increased with increasing overpotential. The behavior of current change with time is similar for all the overpotentials, in which the current density increases to a maximum and then decreases gradually. Figure 4-9(b) shows the SEM images of the Li-Si alloy prepared under different potentials. The pyramid number density (corresponds to bigger pyramids) decreased with smaller overpotential (the lithiation potential change from 10 mV to 70 mV vs Li/Li^+). This is reasonable that smaller overpotential resulted in less nuclei formation.

The electrochemical nucleation and growth can be 3-dimensional (3D) and 2-dimensional (2D) nucleation and growth theory. 3D nucleation and growth apply to a particle or pyramid, but 2D nucleation and growth apply to a monolayer formation on a substrate. According to the SEM image in Figure 4-1, the electrochemical nucleation and growth of the Li-Si alloys must be 3D mode. In 3D nucleation and growth, if the nucleation rate is very high and the nuclei form in a very short time, it will be called instantaneous nucleation; if the nucleation rate is low and the nuclei form with time, it will be called progressive nucleation. Here, the nucleation and growth mechanism can be determined by fitting experimental results using the nucleation and growth models which are called instantaneous (equation 4-1) and progressive (equation 4-2) nucleation,

respectively

$$[j/j_{\max}]^2 = \frac{1.9542}{t/t_{\max}} \{1 - \exp[-1.2564(t/t_{\max})]\}^2 \quad 4-1$$

$$[j/j_{\max}]^2 = \frac{1.2254}{t/t_{\max}} \{1 - \exp[-2.3367(t/t_{\max})^2]\}^2 \quad 4-2$$

It is convenient to use reduced variable plots, where $(j/j_{\max})^2$ is plotted vs. (t/t_{\max}) for comparison of theoretical plots with the experimental current obtained at different overpotential, which was shown in Figure 4-9(c). A good agreement with experimental data along with the instantaneous nucleation mechanism is obtained at high overpotential when the lithiation potential were 10 mV and 30 mV. However, the lithiation prefer to progressive nucleation at lower overpotential when the lithiation potential were 50 mV and 70 mV. This is consistent with predicted model.

Here, a general expression equation 4-3 for three-dimensional diffusion-controlled electrodeposition was applied to fit the entire current, to get the parameters A (nucleation rate constant per site) and N_0 (number density of active sites over Si surface),

$$j(t) = \left(\frac{zFD^{1/2}c}{\pi^{1/2}t^{1/2}} \right) \left(1 - \exp \left\{ -N_0\pi k' D \left[t - \frac{(1 - \exp(-At))}{A} \right] \right\} \right) \quad 4-3$$

where c is the lithium ion concentration in the bulk and $k' = (8\pi cM/\rho)^{1/2}$ with M and ρ being the molecular weight and density of the Si-Li alloy, respectively. Instantaneous and progressive nucleation models are the special cases when the nucleation rates are greatly large and greatly small. Equation 4-3 will transfer to equation 4-4 with extreme large A and equation 4-5 with extreme small A , respectively,

$$j(t) = \left(\frac{zFD^{1/2}C}{\pi^{1/2}t^{1/2}} \right) (1 - \exp\{-N_0\pi k'Dt\}) \quad 4-4$$

$$j(t) = \left(\frac{zFD^{1/2}C}{\pi^{1/2}t^{1/2}} \right) (1 - \exp\{-N_0\pi k'DAt^2\}) \quad 4-5$$

Equation 4-4 and 4-5 will be reduced into equation 4-1 and 4-2 when $(j/j_{\max})^2$ vs. (t/t_{\max}) were applied. Therefore, by fitting the current using equation 4-3, the nucleation rate A and number density N_0 can be obtained and shown in Figure 4-9(c).

According to the atomistic model, the potential dependence of nucleation rate, is given by

$$\frac{d \ln A N_{\infty}}{d|\eta|} = \frac{ze}{kT} (\beta + N_{\text{crit}}) \quad 4-5$$

Here, η is the overpotential, and N_{crit} is the number of atoms in the critical nucleus and k is the Boltzmann constant. β is a cluster-adsorbate interaction parameter, related to the atom attachment mechanism. When the overpotential increased, the nucleation rate and number density of active sites increased. These phenomena were consistent with that in Si lithiation when the overpotential was changed shown in Figure 4-9(d). In summary, the Si(111) lithiation process can be described by a diffusion controlled instantaneous nucleation model.

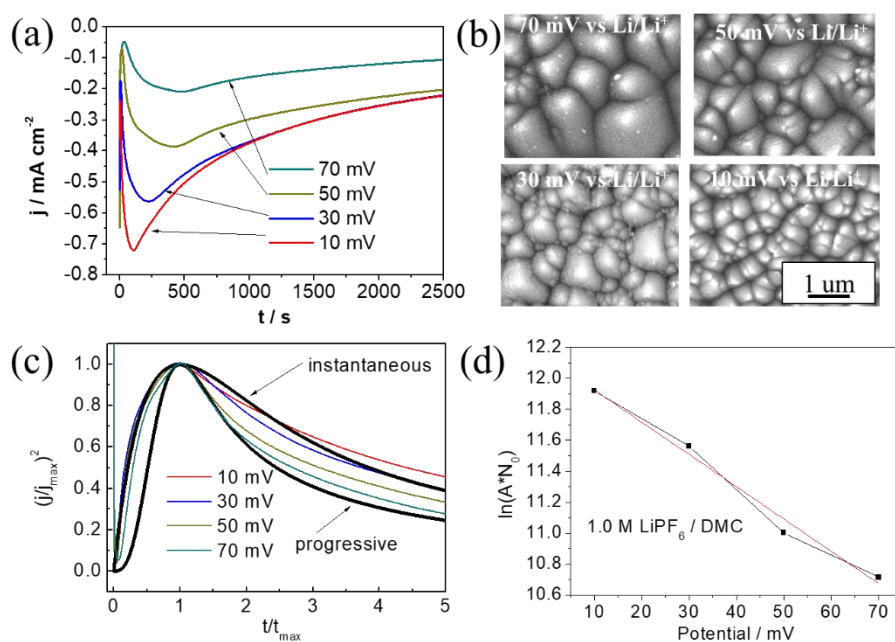


Figure 4-9. (a) Current density as a function of time for Si(111) lithiation at different potential in 1.0 M LiPF₆ in DMC solution. (b) SEM images of the Li-Si alloys prepared under different potential. (c) $(j/j_{\text{max}})^2$ vs. t/t_{max} plot of the current density in (a) compared with theoretical curves for instantaneous and progressive nucleation model according to equation 4-1 and 4-2. (d) Calculated number density of Si-Li alloy pyramid on the surface according to the instantaneous nucleation and growth model.

4.3 Conclusions

In this chapter, electrochemically prepared Li-Si alloys with increasing charge density under potentiostatic charging at 10 mV vs. Li/Li⁺ were investigated using SEM, SXES and windowless EDS to study the single crystal Si(111) lithiation process. Under potentiostatic charging, the lithiation current density increased to a peak of 720 $\mu\text{A}\cdot\text{cm}^{-2}$, and then decreased gradually to a constant value. The crystalline Li₁₅Si₄ alloy layer began to grow, while the Li diffused Li_xSi alloy layer grew into the Si substrate until the lithiation current reach its maximum. The amorphous Li₁₃Si₄ alloy then began to grow after the peak lithiation current was reached, which led to the main lithiation charge. In addition, SXES revealed that surface pyramid structures form an amorphous Li₁₅Si₄ phase at the beginning of lithiation, which then transform into a crystalline Li₁₅Si₄ phase before the peak lithiation current is reached. The in-situ XRD confirmed further the formation of crystalline Li₁₅Si₄ phase at beginning of Si lithiation. Combined with SXES and in-situ synchrotron XRD, we can summary that there are the formations of amorphous and crystalline Li₁₅Si₄ phase at the beginning of Si lithiation, and amorphous transformed into crystalline phase when Si has more lithiation. The Si(111) lithiation process can be described by a diffusion controlled instantaneous nucleation model.

Reference

1. Kasavajjula, U.; Wang, C. S.; Appleby, A. J., Nano- and bulk-silicon-based insertion anodes for lithium-ion secondary cells. *J Power Sources* **2007**, *163* (2), 1003-1039.
2. Su, X.; Wu, Q. L.; Li, J. C.; Xiao, X. C.; Lott, A.; Lu, W. Q.; Sheldon, B. W.; Wu, J., Silicon-Based Nanomaterials for Lithium-Ion Batteries: A Review. *Advanced Energy Materials* **2014**, *4* (1), 23.
3. Chan, C. K.; Peng, H.; Liu, G.; McIlwrath, K.; Zhang, X. F.; Huggins, R. A.; Cui, Y., High-performance lithium battery anodes using silicon nanowires. *Nature Nanotechnology* **2008**, *3* (1), 31-35.
4. Szczech, J. R.; Jin, S., Nanostructured silicon for high capacity lithium battery anodes. *Energy & Environmental Science* **2011**, *4* (1), 56-72.
5. Liu, X. H.; Zhong, L.; Huang, S.; Mao, S. X.; Zhu, T.; Huang, J. Y., Size-Dependent Fracture of Silicon Nanoparticles During Lithiation. *Acs Nano* **2012**, *6* (2), 1522-1531.
6. Teki, R.; Datta, M. K.; Krishnan, R.; Parker, T. C.; Lu, T.-M.; Kumta, P. N.; Koratkar, N., Nanostructured Silicon Anodes for Lithium Ion Rechargeable Batteries. *Small* **2009**, *5* (20), 2236-2242.
7. Obrovac, M. N.; Christensen, L., Structural Changes in Silicon Anodes during Lithium Insertion/Extraction. *Electrochemical and Solid-State Letters* **2004**, *7* (5), A93-A96.
8. Li, J.; Dahn, J. R., An in situ X-ray diffraction study of the reaction of Li with crystalline Si. *J. Electrochem. Soc.* **2007**, *154* (3), A156-A161.
9. Son, S.-B.; Trevey, J. E.; Roh, H.; Kim, S.-H.; Kim, K.-B.; Cho, J. S.; Moon, J.-T.; DeLuca, C. M.; Maute, K. K.; Dunn, M. L.; Han, H. N.; Oh, K. H.; Lee, S.-H., Microstructure Study of Electrochemically Driven Li_xSi. *Advanced Energy Materials* **2011**, *1* (6), 1199-1204.
10. Zeng, Z.; Liu, N.; Zeng, Q.; Ding, Y.; Qu, S.; Cui, Y.; Mao, W. L., Elastic moduli of polycrystalline Li₁₅Si₄ produced in lithium ion batteries. *J Power Sources* **2013**, *242*, 732-735.
11. Misra, S.; Liu, N.; Nelson, J.; Hong, S. S.; Cui, Y.; Toney, M. F., In Situ X-ray Diffraction Studies of (De)lithiation Mechanism in Silicon Nanowire Anodes. *Acs Nano* **2012**, *6* (6), 5465-5473.
12. Chan, C. K.; Ruffo, R.; Hong, S. S.; Huggins, R. A.; Cui, Y., Structural and electrochemical study of the reaction of lithium with silicon nanowires. *J Power Sources* **2009**, *189* (1), 34-39.
13. Liu, X. H.; Wang, J. W.; Huang, S.; Fan, F. F.; Huang, X.; Liu, Y.; Krylyuk, S.; Yoo, J.; Dayeh, S. A.; Davydov, A. V.; Mao, S. X.; Picraux, S. T.; Zhang, S. L.; Li, J.; Zhu, T.; Huang, J. Y., In situ atomic-scale imaging of electrochemical lithiation in silicon. *Nature Nanotechnology* **2012**, *7* (11), 749-756.
14. An, Z. L.; Kamezawa, C.; Hirai, M.; Kusaka, M.; Iwami, M., Valence band density of states of Cu₃Si studied by soft X-ray emission spectroscopy and a first-principle molecular orbital calculation. *Journal of the Physical Society of Japan* **2002**, *71* (12), 2948-2952.
15. Terauchi, M.; Koshiya, S.; Satoh, F.; Takahashi, H.; Handa, N.; Murano, T.; Koike, M.; Imazono, T.; Koeda, M.; Nagano, T.; Sasai, H.; Oue, Y.; Yonezawa, Z.; Kuramoto, S., Chemical State Information of Bulk Specimens Obtained by SEM-Based Soft-X-Ray Emission Spectrometry. *Microscopy and Microanalysis* **2014**, *20* (3), 692-697.
16. Aoki, N.; Omachi, A.; Uosaki, K.; Kondo, T., Structural Study of Electrochemically Lithiated Si(111) by using Soft X-ray Emission Spectroscopy Combined with Scanning Electron Microscopy and through X-ray Diffraction Measurements. *Chemelectrochem* **2016**, *3* (6), 959-965.
17. Hovington, P.; Timoshevskii, V.; Burgess, S.; Demers, H.; Statham, P.; Gauvin, R.; Zaghbi, K., Can we detect Li K X-ray in lithium compounds using energy dispersive spectroscopy? *Scanning* **2016**, *38* (6), 571-578.

Chapter 5

Effects of Hydrogen Fluoride on the Structures and Compositions of Li-Si alloys

5.1 Introduction

One of the problems that limit the use of Si anode in Li ion batteries is the big volume expansion after alloying with Li.¹⁻³ The big volume expansion resulted in unstable surface chemistry. A solid electrolyte interphase (SEI) between Si anode and electrolyte can be destroyed due to the cycled Si anode expansion and shrinkage.⁴ The unstable SEI was harmful to cycle life of secondary batteries since the electrolyte was consumed due to its reaction with Si anode. Several strategies such as Si nanoparticles or nanowires have been proven to be effective to reduce the volume expansion and enhance the SEI stability.⁵⁻⁷ The interphase can affect the structures and compositions of the Li-Si alloys after Si alloying with Li, and then affect the battery performance such as cycle life and capacity.⁸⁻¹¹

Electrolyte addition are considered as key factors that affect the battery performance of the Si based secondary batteries.¹² It had been revealed the Si anode based secondary batteries using ethylene carbonate (EC) or propylene carbonate (PC) as electrolyte solvents had low capacity and cycle life.¹³⁻¹⁴ Some reports had determined the fluoroethylene carbonate (FEC) solvent can improve the capacity and cycle life of the Si anode based secondary battery significantly.¹⁵⁻¹⁶ The improvements were considered to stem from a stable SEI formation. It had been known FEC can decompose into vinyl carbonate (VC) and hydrogen fluoride (HF). VC can polymerize into a passivation polymer film as stable interphase on Si surface, to prevent the continuous electrolyte decomposition. HF was expected to form LiF species on Si surface to suppress the reaction between the Si surface and the electrolyte.¹⁵⁻¹⁷ Although the beneficial effects of FEC on SEI by forming polymer film and LiF species had been widely studied, the effects of FEC on the structures and compositions of Li-Si alloys are not yet understood. Our previous studies on the structures and compositions of the electrochemically

prepared Li-Si alloys had revealed the Li-Si alloy had layered structure and composition.¹⁸⁻¹⁹ The soft x-ray emission spectroscopy (SXES) and windowless energy dispersive spectroscopy (EDS) were the main characterization techniques.

In this chapter, the FEC and its decomposed product HF effects on the structures and compositions of the Li-Si alloys were studied by combining SEM, SXES, and windowless EDS analysis. The Li-Si alloys were prepared by using single crystal Si(111) lithiation under potentiostatically charging at 10 mV vs. Li/Li⁺ in 1.0 M LiPF₆ in FEC and PC solvents with different concentration of HF aqueous solution addition. The lithiation charge density is 1000 mC·cm⁻² for all the Li-Si alloys. The structures are obtained by SEM. The components are analyzed by SXES. The Li K_α, Si L_{2,3} and Si K_α intensity changes were strictly analyzed to obtain the specific thicknesses and Li distribution for the Li-Si alloy layers. The effects of FEC and its decomposed product HF on the structures and compositions of the Li-Si alloys will be determined and discussed.

5.2 Results and Discussion

5.2.1 Compositions of Li-Si alloys Prepared in PC and FEC

Figure 5-1(a) and (b) show SEM images for the surface and the cross section of Li-Si alloys prepared in the electrolyte of 1.0 M LiPF₆ in PC solvent. It was observed from Figure 5-1(a) that a large number of pyramid structures (see inset figure) covered the Si surface. Figure 5-1(b) shows the layered structure of the Li-Si alloy. The 1st layer consists of the triangular pyramid structures with approximately 0.7 μm height. Underneath the 1st layer there are the 2nd and 3rd layers with average thicknesses of approximately 1.2 and 2.0 μm, respectively. Figure 5-1(c) and (d) show SEM images for the surface and the cross section of Li-Si alloys prepared in the electrolyte of 1.0 M LiPF₆ in FEC solvent. The pyramid had smaller size than that prepared in PC. The layered structures are also shown in this Li-Si alloy.

The compositions of the Li-Si alloys were determined by SXES. Figure 5-1(e-f) show the SXE spectra of the 1st, 2nd and 3rd as well as Li metal and c-Si references in the photon energy region of 50–105 eV, which covered Li K_α and Si L_{2,3} X-ray emissions. Combined with DOS calculation,²⁰ it had been indicated the peak energy of 53.3 eV in

Li K_{α} and 91.8 eV in Si $L_{2,3}$ was relative to c- $\text{Li}_{15}\text{Si}_4$ alloy, and the peak energy of 53.6 eV in Li K_{α} and 91.6 eV in Si $L_{2,3}$ was relative to a- $\text{Li}_{13}\text{Si}_4$ alloy.¹⁸ The Si $L_{2,3}$ emission peaks from c-Si were associated with low-lying Si 3s-3s bonding state at 89.6 eV, while the main peak at 92.0 eV and the shoulder at 96.0 eV originate from the p components of sp^3 hybridization.²¹⁻²² In the following discussion, the peak energies were used to determine the compositions of the Li-Si alloys.

The Li K_{α} emission peak energies of the 1st layers in the Li-Si alloys prepared in PC and FEC were 53.3 and 53.6 eV (Figure 5-1(e)), respectively. It indicated the 1st layer in the Li-Si alloy of PC was c- $\text{Li}_{15}\text{Si}_4$ alloy, and the 1st layer in the Li-Si alloy of FEC was a- $\text{Li}_{13}\text{Si}_4$ alloy. The Li K_{α} emission peak energies of the 2nd layers in the Li-Si alloys prepared in PC and FEC were both 53.6 eV. It indicated the 2nd layers in the Li-Si alloys of PC and FEC were both a- $\text{Li}_{13}\text{Si}_4$ alloy. There was little Li K_{α} emission intensity of the 3rd layers in both Li-Si alloys since the Li concentration in the 3rd layer was very small.¹⁹ Therefore from the Li K_{α} emission peak energies analysis, it was found the Li-Si alloy prepared in FEC preferred to form a- $\text{Li}_{13}\text{Si}_4$ alloy compared with that prepared in PC. The composition determination results could be further confirmed by Si $L_{2,3}$ emission spectra. In Figure 5-1(f), the Si $L_{2,3}$ emission peak energies of the 1st layers in the Li-Si alloys prepared in PC and FEC were 91.8 and 91.6 eV, respectively. It indicated the 1st layer in the Li-Si alloy of PC was c- $\text{Li}_{15}\text{Si}_4$ alloy, and the 1st layer in the Li-Si alloy of FEC was a- $\text{Li}_{13}\text{Si}_4$ alloy. These results were consistent with the Li K_{α} analysis results. The Si $L_{2,3}$ emission peak energies of the 2nd layers in the Li-Si alloys prepared in PC and FEC were both 91.6 eV, which confirmed again the 2nd layers in the Li-Si alloys of PC and FEC were both a- $\text{Li}_{13}\text{Si}_4$ alloy.

The SXE spectra of the Li-Si alloy prepared in PC were consistent with Aoki's work,¹⁸ which determined the 1st layer was c- $\text{Li}_{15}\text{Si}_4$ and the 2nd layer was a- $\text{Li}_{13}\text{Si}_4$. The composition in the 3rd layer was hard to determine by SXE spectra, however it had been determined as a Li-diffused Li_xSi alloy layer using windowless EDS in our previous work.¹⁹ The SXE spectra of the Li-Si alloy prepared in FEC indicated the 1st and 2nd layer were both a- $\text{Li}_{13}\text{Si}_4$. In a word, the compositions of the Li-Si alloys prepared in PC and FEC were different.

Since FEC can decompose into VC and HF, the HF concentration in the electrolyte of 1.0 M LiPF₆ in FEC solvent was measured using IC. The result revealed the HF concentration was larger than 50 mM in the electrolyte. However, the HF concentration in the electrolyte of 1.0 M LiPF₆ in PC solvent was less than 0.05 mM. The produced HF in the electrolyte of 1.0 M LiPF₆ in FEC solvent was expected to affect the structures and compositions of the Li-Si alloy. In the following part, the effects of HF on the structures and compositions were studied by adding HF aqueous solution into the electrolyte. The underlying mechanism was discussed.

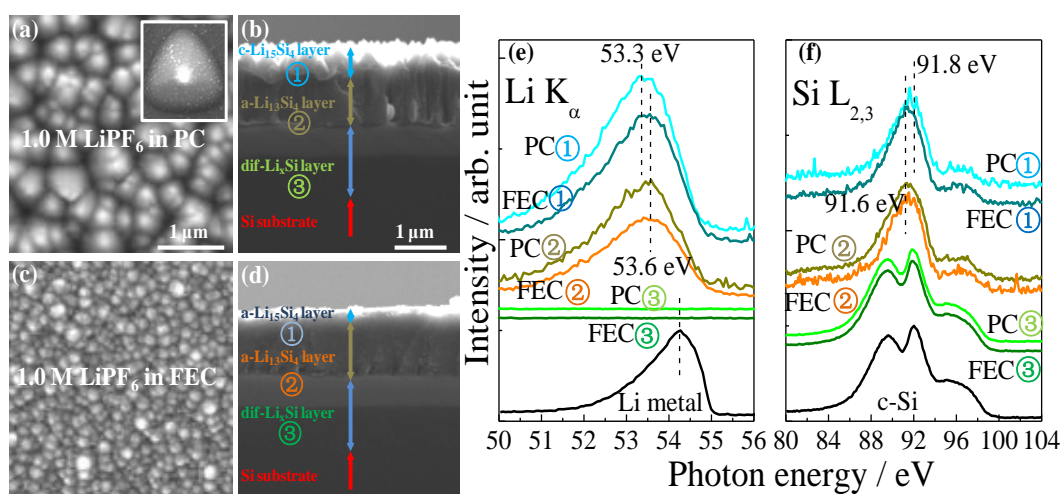


Figure 5-1. SEM images for (a, c) the surface and (b, d) the cross section of Li-Si alloys prepared in the electrolyte of 1.0 M LiPF₆ dissolved in PC and FEC solvents, respectively. In Figure 5-1 (b) and (d), the layered structures of the 1st, 2nd, 3rd and Si substrate are represented by different color arrows and number. The compositions are shown according to the SXES results in Figure 1e-f. (e-f) SXE spectra of the 1st, 2nd, 3rd and 4th layers of these two Li-Si alloys. The peak energy of 53.6 eV in Li K_α and 91.6 eV in Si L_{2,3} relative to a-Li₁₃Si₄ alloy are shown. The peak energy of 53.3 eV in Li K_α and 91.8 eV in Si L_{2,3} relative to c-Li₁₅Si₄ alloy are also shown.

5.2.2 The effects of HF on the structures and compositions of Li-Si alloys

Figure 5-2(a-d) show the SEM images for the surface of Li-Si alloys prepared in different electrolytes that had increased HF concentration. The pyramids exist in all the Li-Si alloys and covered the Si surface. The sizes of the pyramids are dependent on the

HF concentrations in the electrolytes. The pyramid size was measured and shown in Figure 5-2(e). It was found that when the electrolytes had increased HF concentrations, the pyramid size of the Li-Si alloys prepared therein decreased. Obviously, the pyramid nuclei number density increased when the HF concentration increased.

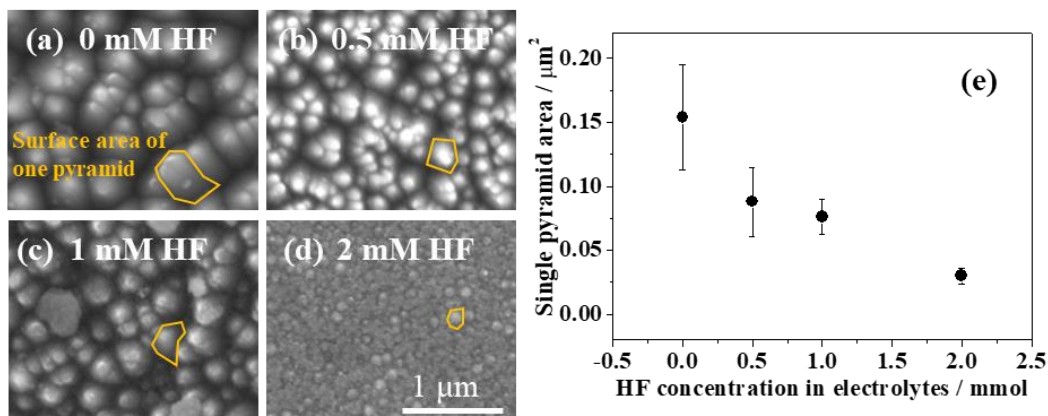


Figure 5-2. (a-d) SEM images for the surface of the Li-Si alloys prepared in 0/0.5/1/2 mM HF containing electrolytes and (e) pyramid size change with HF concentration (solid dots) for all Li-Si alloy. The measurement schematic for pyramid size is shown in Figure 2a and at least 100 pyramids were measured.

The HF effects can be better determined by observing its effects on the layered structures of the Li-Si alloys. Figure 5-3(a-d) shows the SEM images for the cross section of the Li-Si alloys. The layered structures are observed for all the Li-Si alloys. For the Li-Si alloy prepared in the electrolyte of 1.0 M LiPF₆ in PC solvent without HF addition, it had been determined to consist of the 1st crystalline Li₁₅Si₄ layer, the 2nd amorphous Li₁₃Si₄ layer, and the 3rd Li-diffused Li_xSi layer. Obviously, the layer thicknesses of the 1st and 2nd layer in different Li-Si alloys were dependent on the electrolytes which had increased HF concentrations.

The effects of HF on the compositions of the Li-Si alloys were determined using SXES. Figure 5-3(e, f) show the SXE spectra of the 1st layers in the Li-Si alloys prepared in the electrolytes with increase HF concentration. When the electrolytes had increased HF concentrations, the Li K_α emission peak of the Li-Si alloys prepared therein changed from 53.3 to 53.6 eV (Figure 5-3(e)). The 53.3 and 53.6 eV were the peak energy of Li

K_{α} emission spectra of c- $\text{Li}_{15}\text{Si}_4$ and a- $\text{Li}_{13}\text{Si}_4$, respectively, according to previous analysis.¹⁸ The peak energy change from 53.3 to 53.6 eV indicated that the amount of c- $\text{Li}_{15}\text{Si}_4$ in the 1st layer decreased, instead the amount of a- $\text{Li}_{13}\text{Si}_4$ increased. Meanwhile, the Si $L_{2,3}$ emission peak of the Li-Si alloys changed from 91.8 to 91.6 eV (Figure 5-3(f)). Since the peak energies of Si $L_{2,3}$ emission spectra of c- $\text{Li}_{15}\text{Si}_4$ and a- $\text{Li}_{13}\text{Si}_4$ were 91.8 and 91.6 eV, respectively, the peak shifts from 91.8 to 91.6 eV indicated that the 1st layer preferred to form a- $\text{Li}_{13}\text{Si}_4$ instead of c- $\text{Li}_{15}\text{Si}_4$. This result was consistent with that from the observation of Li K_{α} emission peaks shift. In a word, the amount of c- $\text{Li}_{15}\text{Si}_4$ in the 1st layer decreased when the HF concentration increased in the electrolytes. The compositions of the Li-Si alloys were altered by HF addition.

Figure 5-3(g, h) show the SXE spectra of the 2nd layers in the Li-Si alloys. Although the electrolytes had increased HF concentrations, the Li K_{α} and Si $L_{2,3}$ emission peaks of the Li-Si alloys prepared therein had the same energy position of 53.6 and 89.6 eV. Both peak positions were corresponding to the Li K_{α} and Si $L_{2,3}$ emission peaks of a- $\text{Li}_{13}\text{Si}_4$. It indicated the composition in the 2nd layers of all the four different Li-Si alloys were a- $\text{Li}_{13}\text{Si}_4$ and independent on the HF concentration.

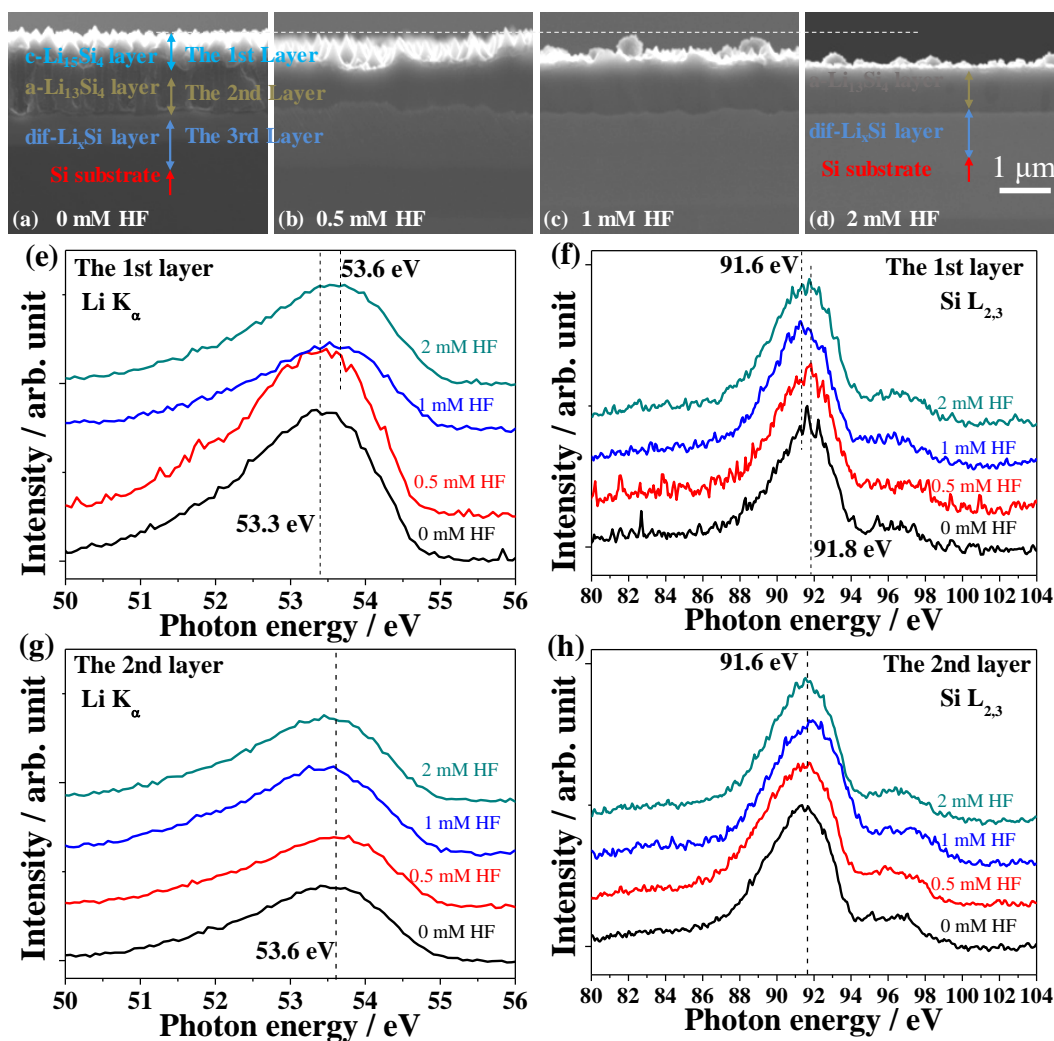


Figure 5-3. (a-d) SEM images for the cross section of the Li-Si alloys prepared in 0/0.5/1/2 mM HF containing electrolytes. (e) Li K_{α} and (f) Si $L_{2,3}$ emission spectra of the 1st layer in the four Li-Si alloys. (g) Li K_{α} and (h) Si $L_{2,3}$ emission spectra of the 2nd layer in the four Li-Si alloys. The peak energy positions are represented by dotted line, in which, 53.3 and 53.6 eV in Li K_{α} emission spectra and 91.6 and 91.8 eV in Si $L_{2,3}$ emission spectra are shown.

Windowless EDS had been applied to determine the Li distribution in Li-Si alloys,¹⁹ and also the layer thickness. For a Li-Si alloy prepared in 1.0 M LiPF₆ in PC solvent, it had revealed the Li distribution profile determined by windowless EDS was consistent with layered structure determined by SXES. In the above SXE spectra analysis, it suggested the compositions of the Li-Si alloys prepared in electrolytes containing different HF concentration were different. To further reveal the amount of different

compositions like c-Li₁₅Si₄, a-Li₁₃Si₄ and Li-diffused Li_xSi alloy, windowless EDS was used.

Figure 5-4(a,b) show the intensity changes of Li K_α and Si K_α emissions along the line scan from the pyramid top (the 1st layer) to Si substrate for the Li-Si alloys, respectively. The intensity changes of Li K_α were similar for all the four Li-Si alloys in Figure 5-4(a). The Li K_α intensity decreased from the 1st layer to Si substrate, consistent with the Li-Si alloy layered structure which consist the 1st c-Li₁₅Si₄ layer, the 2nd a-Li₁₃Si₄ layer and the 3rd lowly lithiated Li_xSi layer over Si substrate. The boundaries between the 1st and 2nd layer, the 2nd and 3rd layer, can be determined by monitoring the Li K_α intensity change. It can be easily observed the layer boundaries (dotted arrows) in the Li-Si alloys moved to less deep position when the used electrolytes had increased HF concentration. In Figure 5-4(b), the Si K_α intensity increased from the 1st layer to Si substrate. The boundaries between the 2nd and 3rd layer can be determined by monitoring the Si K_α intensity change. It can be also observed the layer boundaries moved to less deep position when the used electrolytes had increased HF concentration. This is consistent with the observation in Li K_α intensity change. However, the intensity changes of Li K_α and Si K_α are not able to determine the thickness of each layer in the Li-Si alloys, since the boundaries between the 3rd layer and Si substrate are unclear. As can be observed in the insert Figure in Figure 5-4(a), the Li K_α intensities within the 3rd layer is not high enough to distinguish the layer between the 3rd layer and Si substrate.

As had been reported, the thickness of each layer can be precisely determined by monitoring the Si L_{2,3} intensity change.¹⁹ Figure 5-4(c) shows the Si L_{2,3} intensity changes for the four Li-Si alloys. The boundaries between the 1st, 2nd, 3rd layer and Si substrate can be easily determined by monitoring the intensity change and shown as arrows. Then the thickness of each layer for all the four Li-Si alloys can be easily determined and shown in Figure 5-4(d). It was found that when the electrolytes had increased HF concentrations from 0 to 2 mM, the 1st layer thickness (the c-Li₁₅Si₄ pyramid height) in the Li-Si alloys prepared therein decreased from approximately 0.7 to 0.1 μm, and the 2nd layer thickness increased from approximately 1.1 to 1.3 μm. Obviously, the Li distribution in the Li-Si alloys had been changed when the used

electrolytes had increased HF concentration. In addition, the thicknesses of the 3rd layer for all the four Li-Si alloys were almost the same.

The thickness can be used to estimate the amount of c-Li₁₅Si₄, a-Li₁₃Si₄ and Li-diffused Li_xSi alloy in the Li-Si alloys. In the present work, the lithiation charge density was 1000 mC·cm⁻² for each Li-Si alloy. Since the lithiation charge was due to Li⁺ ion reduction to alloy Li, we can evaluate the Li amount in c-Li₁₅Si₄ and a-Li₁₃Si₄ based on their layer thicknesses, to reveal how much charge was used to form c-Li₁₅Si₄ and a-Li₁₃Si₄. The Li-Si alloy prepared in 1.0 M LiPF₆ in PC solvent without HF addition, had approximately 0.7 μm c-Li₁₅Si₄ (pyramid) and 1.1 μm a-Li₁₃Si₄. Therefore, the charge used to form c-Li₁₅Si₄ and a-Li₁₃Si₄ were approximately 180 and 760 mC·cm⁻², respectively, in 1000 mC·cm⁻² charge. In other words, about 18% and 76% charge were used to form c-Li₁₅Si₄ and a-Li₁₃Si₄, respectively. The left 6% charge was used to the 3rd layer formation and electrolyte decomposition. As a comparison, the Li-Si alloy prepared in 1.0 M LiPF₆ in PC solvent with 2mM HF addition, had approximately 0.1 μm c-Li₁₅Si₄ and 1.3 μm a-Li₁₃Si₄. The charge used to form c-Li₁₅Si₄ and a-Li₁₃Si₄ were approximately 30 and 900 mC·cm⁻², respectively. In other words, about 3% and 90% charge were used to form c-Li₁₅Si₄ and a-Li₁₃Si₄, respectively. Obviously, the amount of c-Li₁₅Si₄ in the Li-Si alloys decreased from 18% to 3% and the amount of a-Li₁₃Si₄ in the Li-Si alloys increased from 76% to 90% when the used electrolyte had 2 mM HF addition as shown in Figure 5-4(d).

It had been determined the Li-Si alloys prepared in 1.0 M LiPF₆ in FEC had the similar structure and composition with that prepared in 1.0 M LiPF₆ in PC with 2 mM HF addition. We can say the amount of c-Li₁₅Si₄ was about 3% in the Li-Si alloys prepared in 1.0 M LiPF₆ in FEC, significantly smaller than 18% in the Li-Si alloys prepared in 1.0 M LiPF₆ in PC with 0 mM HF. The experimental result that the amount of c-Li₁₅Si₄ for FEC is smaller than that for PC, can explain why FEC had better battery performance in Si-based secondary batteries. Since the crystalline alloy phase formation was generally considered to be detrimental to battery performance,²³ the less c-Li₁₅Si₄ formation in the Li-Si alloys will be good for battery performance.

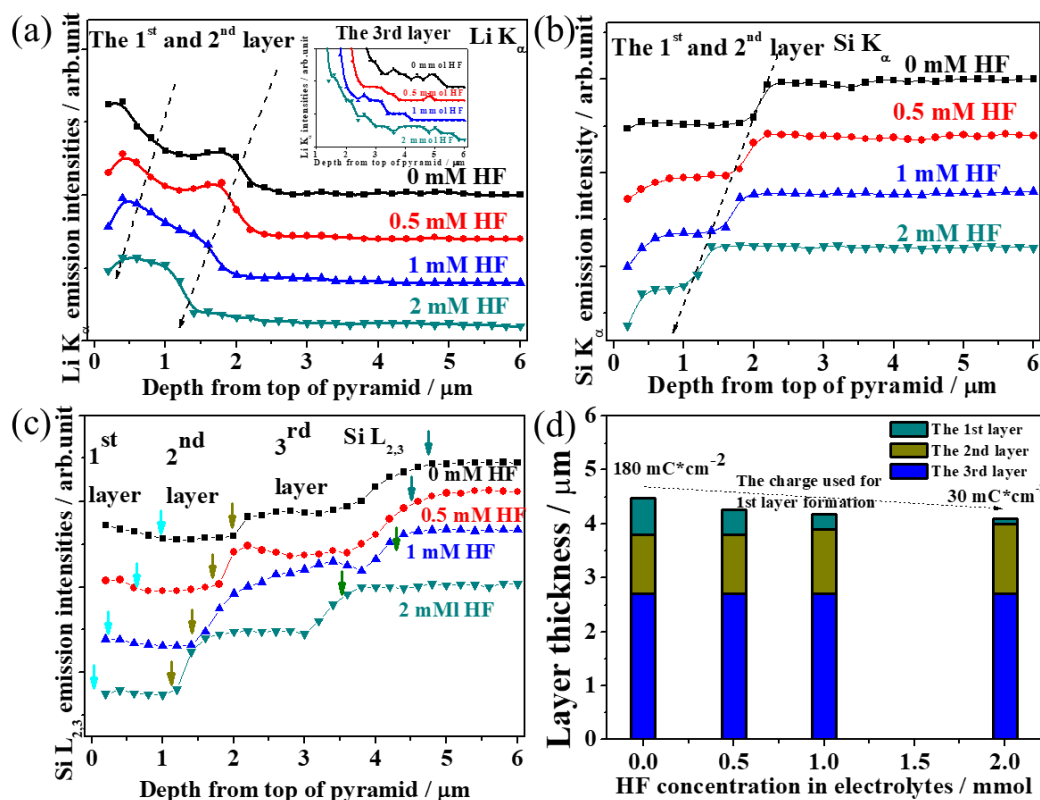


Figure 5-4. Windowless EDS (a) Li K α , (b) Si K α and (c) Si L_{2,3} emission intensity changes along the cross section from the pyramid top to Si substrate for the four Li-Si alloys. The HF concentrations in the electrolytes are shown. The inset in Figure 5-4(a) shows the enlarged Li K α emission intensity changes within the 3rd layer. The boundary between the 1st, 2nd, 3rd, and Si substrate can be determined by monitoring the intensity change. In Figure 5-4(c), the cyan arrows represent the boundary between the 1st and 2nd layer. The dark yellow arrows represent the boundary between the 2nd and 3rd layer. The dark green arrows represent the boundary between the 3rd and 4th layer. (d) The layer thicknesses of the 1st, 2nd and 3rd layer for the four Li-Si alloys determined from Figure 5-4(c).

The electrolyte of 1.0 M LiPF₆ in FEC contained HF bigger than 50 mM. The HF mainly stems from the decomposition of FEC. As analyzed above, the HF can reduce the size of the c-Li₁₅Si₄ pyramid, in other words, increase the pyramid nuclei number density. It had been reported F⁻ can be adsorbed on Si surface to form F-Si bond.²⁴ The adsorption of F species on Si(111) were confirmed by XPS results which was shown in Figure 5-5(a). The photoelectron emission intensities from F 1s increased when the

electrolytes had increased HF concentration, which indicated the amount of F element on Si(111) surface increased. The increase of F element amount was due to two parts, in which, one is the enhanced LiF (686.5 eV) deposition through Li⁺ and F⁻ ion, and the other is the F⁻ ion adsorption on Si(111) surface to generate F-Si bond (688.5 eV) as shown in Figure 5-5(b). The Langmuir adsorption model (the equation in Figure 5-5(b)) is used to simulate F⁻ ion adsorption. The Langmuir adsorption model can be applied to fixed number of adsorption sites on solid surface and all the adsorption sites are equal. In our work, the Si substrate is single crystal H-Si(111), which has almost fixed and equal Si adsorption sites for F⁻ ion adsorption. The Langmuir adsorption model can be applied to a monolayer adsorption and a dynamic equilibrium between adsorbed and desorbed species. In our work, the H-Si(111) single crystal is atomically flat and the F⁻ ion adsorption should be a monolayer adsorption. As shown in Figure 5c, the adsorption and desorption of F⁻ ion are in equilibrium. Therefore, the Langmuir adsorption model can be used to fit the F⁻ ion adsorption in our work. The value of adsorption constant K is ca. 716, which is obtained by fitting the experimental data in Figure 5b. Therefore, the adsorption energy ΔG_{ads} is 16.3 kJ/mol according to the equation:

$$\Delta G_{\text{ads}} = RT \ln K,$$

where R and T are the gas constant and room temperature, respectively. The energy is far less than ca. 120 kJ/mol of reaction $\text{HF} + \text{SiH} = \text{SiF} + \text{H}_2$, according to the enthalpy calculation in NIST (a database that is National Institute of Standards and Technology, the formation enthalpy of each species is as follow in kJ/mol, HF: -273.3, SiH: 366.9, SiF: -27.1, H₂: 0). There may be a reason for that the experimental adsorption energy is far less than the calculated reaction enthalpy energy. The reaction $\text{HF} + \text{SiH} = \text{SiF} + \text{H}_2$ suggest a strong SiF (bond strength 582 kJ/mol) chemical bond formation which suggest a strong F adsorption on Si. However, the adsorption energy is only 16.3 kJ/mol and far less than 120 kJ/mol. It can be assumed the F⁻ is adsorbed on Si by electrostatic interaction, which is weaker than a chemical bond formation. Therefore, the adsorption energy is far smaller than 120 kJ/mol.

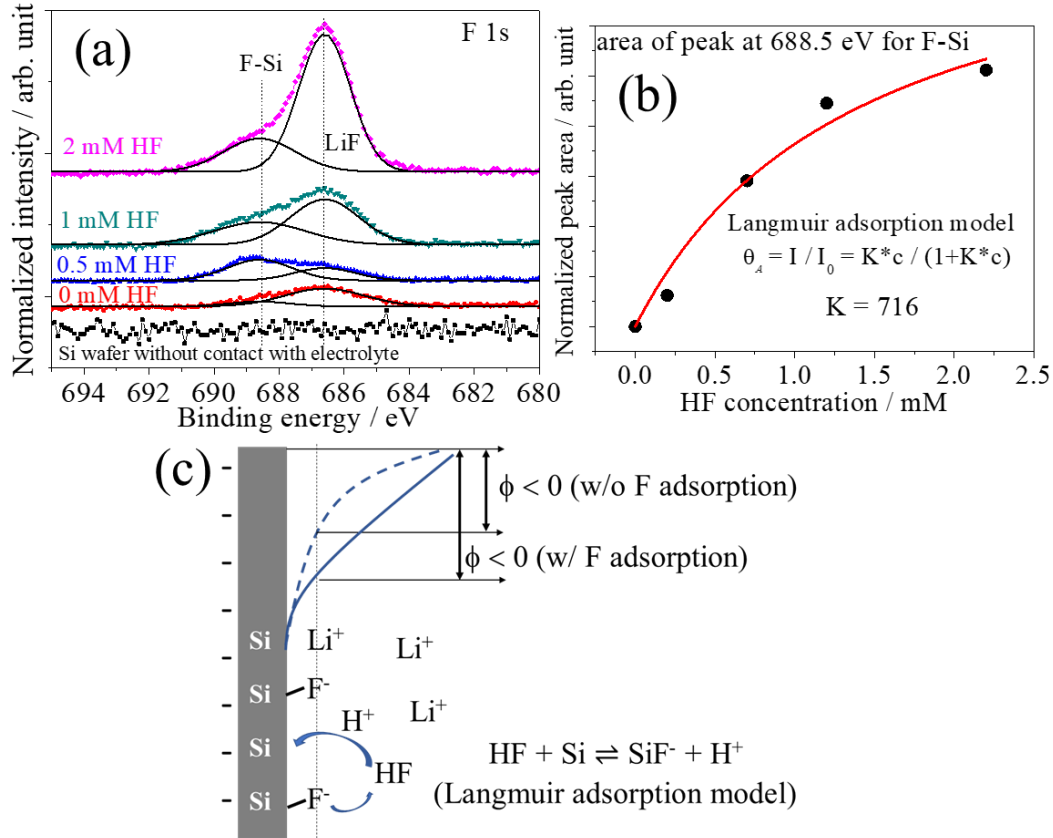


Figure 5-5. (a) XPS F 1s spectra for Si(111) after contact with electrolytes that had increased HF concentrations. Peaks at 688.5 eV are representative of F-Si species, while those at 686.5 eV are representative of LiF species. (b) XPS peak areas at 688.5 eV for F-Si on Si(111) after contact with electrolytes that had increased HF concentrations. The peak area is normalized to Si 2p intensity. (c) Schematic for F adsorption and its effect on the change of surface potential.

The F⁻ adsorption can improve the Li-Si alloy nuclei formation since it improve the surface Li⁺ ion concentration which is a function of potential according to the equation²⁵

$$C_s = C_0 \exp(-F\phi/RT),$$

where C_s is the surface Li⁺ ion concentration, C_0 is the bulk Li⁺ ion concentration, ϕ is the surface potential, F , R and T are Faraday constant, gas constant and room temperature, respectively. The surface potential ϕ went more negative by F⁻ adsorption as shown in Figure 5-5(c), therefore, the surface Li⁺ ion concentration increased. As a result, the nuclei number density of the Li-Si alloys on Si surface increased, to form

smaller pyramid as explained in Figure 5-6. This explained why the Li-Si alloys had smaller pyramid (less amount of c-Li₁₅Si₄) when the electrolyte was 1.0 M LiPF₆ in FEC or had HF addition.

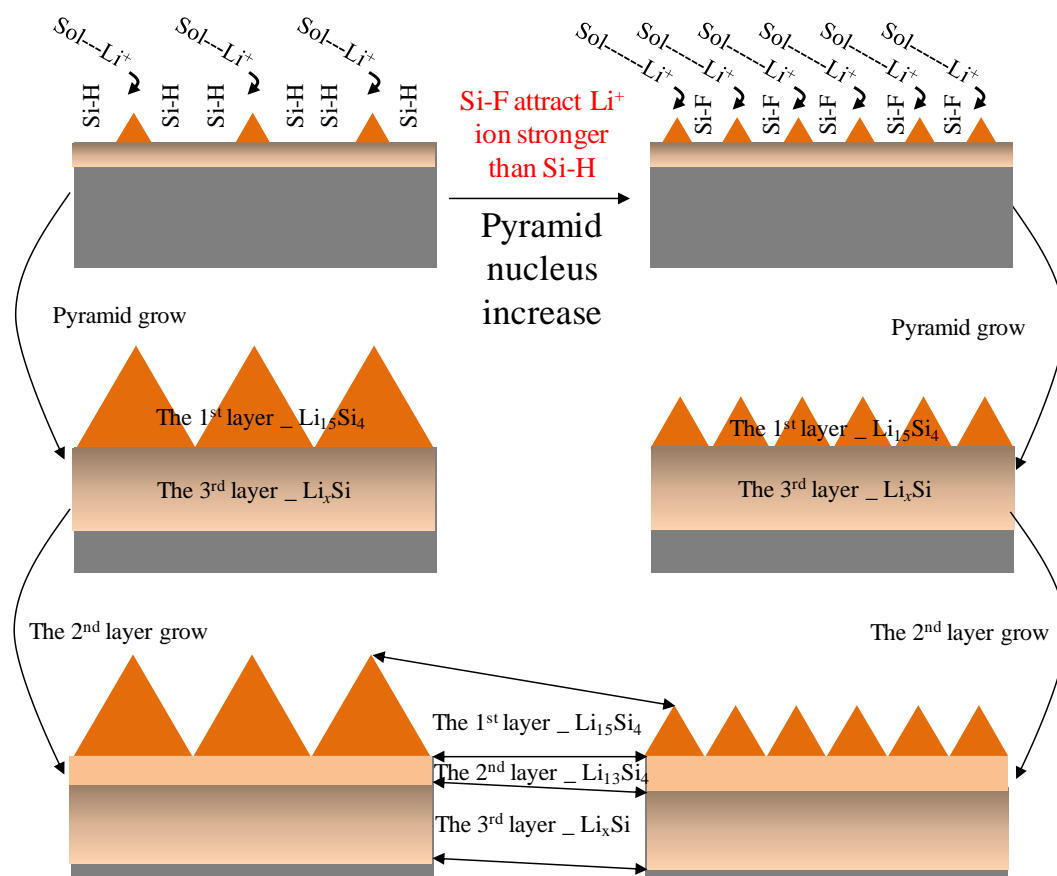


Figure 5-6 The schematic for the F⁻ ion effects on the Si(111) lithiation. The layer growth process was also shown.

Figure 5-7 shows the current density as a function of time when the potential was stepped to 0.01 V for Si(111) lithiation. The electrolytes are 1.0 M LiPF₆ in PC solvent with addition of 0, 0.5, 1.0, 2.0 and 4.0 mM HF aqueous solution. For all the Si(111) lithiation behavior in the electrolytes with varied HF concentration, the cathodic current density increased to a maximum at first, and then decreased gradually to an almost constant value. The maximum current decreased with increased HF addition, which had been represented by an arrow in Figure 5-7. According to the analysis in chapter 4, the time when the maximum current arrived (here we call it as maximum time) was inversely proportional to Li-Si alloy nuclei number density. When HF concentration increased in

the electrolytes, the maximum time decreased, which suggested the Li-Si alloy nuclei number density increased. Therefore, the pyramid size decreased. This is consistent with the results observed from the SEM images.

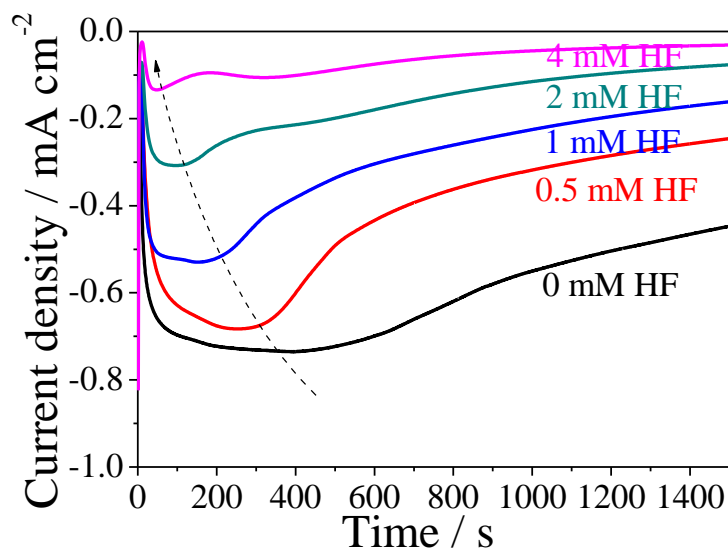


Figure 5-7 Current density as a function of time when the potential was stepped from 500 to 10 mV for Si(111) lithiation in 1.0 M LiPF₆ in PC solvent with varied HF concentration.

On the other hand, trace amount of water played significant role on battery performance.²⁶ In the present study, the electrolytes of 1.0 M LiPF₆ in PC and FEC also contained less than 0.2 mM H₂O. Additionally, when we studied the HF effects by adding HF aqueous solution into the electrolytes, trace amount of water was added inevitably. It had been determined the addition of 2 mM HF aqueous solution can significantly change the structures and compositions of the Li-Si alloys, however, 2 mM HF aqueous solution also contained 2.2 mM H₂O. The water effects on the structures and compositions of Li-Si alloys need to be determined and in the present work 2.2 mM ultrapure water was mixed into the electrolyte of 1.0 M LiPF₆ in PC. The HF concentration in the electrolyte was measured every 4 hours using IC after the water was mixed inside. Figure 6 shows the HF concentration change in the electrolyte with keeping time. Obviously, the HF concentration increased with time, since water will react with LiPF₆ in the electrolytes to produce HF as reported.²⁷ We used the electrolytes

that were mixed with 2 mM H₂O for 0 and 24 hours, to prepare the Li-Si alloys. As was observed, when the electrolyte was just mixed with H₂O for 0 hour, the Li-Si alloys prepared therein showed similar pyramid size with that without H₂O addition. However, when the electrolyte was mixed with H₂O for 24 hours and about 2 mM HF was produced, the Li-Si alloys prepared therein had greatly smaller pyramid compared with that without H₂O addition. In summary, the water can reduce the pyramid size since it can react with LiPF₆ to produce HF, and then adsorbed on Si surface to affect the structure and composition of the Li-Si alloys.

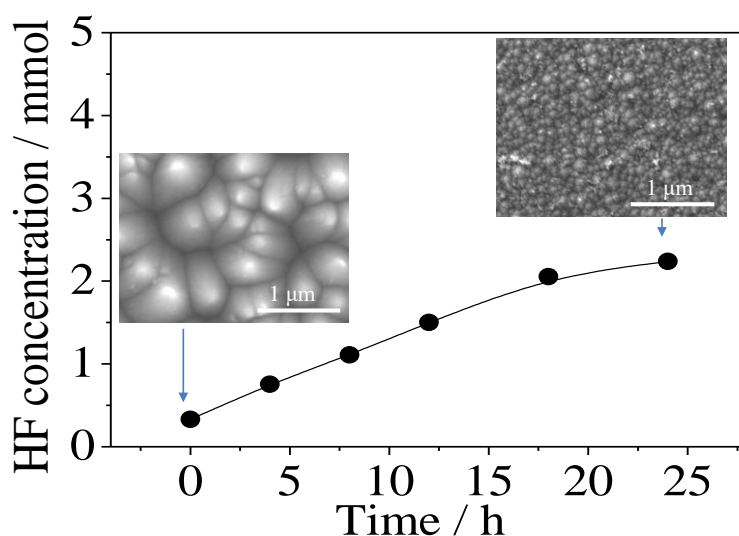


Figure 5-8. HF concentration changes with time in the electrolyte after mixed with 2 mM H₂O. The insets are the SEM images of the Li-Si alloys prepared in the corresponding electrolytes

5.3 Conclusions

In conclusion, the Li-Si alloy preferred to form a-Li₁₃Si₄ alloy instead of c-Li₁₅Si₄ when the electrolytes for the Li-Si alloys preparation had increased HF concentration. Since FEC can decompose to produce HF, the Li-Si alloy prepared in FEC had less amount of c-Li₁₅Si₄ than that in PC. Since the crystalline alloy phase formation generally considered to be detrimental to battery performance,²³ the less c-Li₁₅Si₄ formation in the Li-Si alloys will be good for battery performance. This explained the reason for FEC to improve the battery performance since FEC can decompose to generate HF.

Reference

1. Kasavajjula, U.; Wang, C. S.; Appleby, A. J., Nano- and bulk-silicon-based insertion anodes for lithium-ion secondary cells. *J Power Sources* **2007**, *163* (2), 1003-1039.
2. Su, X.; Wu, Q. L.; Li, J. C.; Xiao, X. C.; Lott, A.; Lu, W. Q.; Sheldon, B. W.; Wu, J., Silicon-Based Nanomaterials for Lithium-Ion Batteries: A Review. *Advanced Energy Materials* **2014**, *4* (1), 23.
3. Chan, C. K.; Peng, H.; Liu, G.; McIlwrath, K.; Zhang, X. F.; Huggins, R. A.; Cui, Y., High-performance lithium battery anodes using silicon nanowires. *Nature Nanotechnology* **2008**, *3* (1), 31-35.
4. Lee, Y. M.; Lee, J. Y.; Shim, H.-T.; Lee, J. K.; Park, J.-K., SEI layer formation on amorphous Si thin electrode during precycling. *J. Electrochem. Soc.* **2007**, *154* (6), A515-A519.
5. Szczech, J. R.; Jin, S., Nanostructured silicon for high capacity lithium battery anodes. *Energy & Environmental Science* **2011**, *4* (1), 56-72.
6. Liu, X. H.; Zhong, L.; Huang, S.; Mao, S. X.; Zhu, T.; Huang, J. Y., Size-Dependent Fracture of Silicon Nanoparticles During Lithiation. *Acs Nano* **2012**, *6* (2), 1522-1531.
7. Teki, R.; Datta, M. K.; Krishnan, R.; Parker, T. C.; Lu, T.-M.; Kumta, P. N.; Koratkar, N., Nanostructured Silicon Anodes for Lithium Ion Rechargeable Batteries. *Small* **2009**, *5* (20), 2236-2242.
8. Ogata, K.; Salager, E.; Kerr, C. J.; Fraser, A. E.; Ducati, C.; Morris, A. J.; Hofmann, S.; Grey, C. P., Revealing lithium-silicide phase transformations in nano-structured silicon-based lithium ion batteries via in situ NMR spectroscopy. **2014**, *5*, 3217.
9. Gregorczyk, K. E.; Liu, Y.; Sullivan, J. P.; Rubloff, G. W., In Situ Transmission Electron Microscopy Study of Electrochemical Lithiation and Delithiation Cycling of the Conversion Anode RuO₂. *Acs Nano* **2013**, *7* (7), 6354-6360.
10. Pharr, M.; Zhao, K.; Wang, X.; Suo, Z.; Vlassak, J. J., Kinetics of Initial Lithiation of Crystalline Silicon Electrodes of Lithium-Ion Batteries. *Nano Lett* **2012**, *12* (9), 5039-5047.
11. McDowell, M. T.; Ryu, I.; Lee, S. W.; Wang, C. M.; Nix, W. D.; Cui, Y., Studying the Kinetics of Crystalline Silicon Nanoparticle Lithiation with In Situ Transmission Electron Microscopy. *Adv Mater* **2012**, *24* (45), 6034+.
12. Xu, K., Electrolytes and Interphases in Li-Ion Batteries and Beyond. *Chem Rev* **2014**, *114* (23), 11503-11618.
13. Shi, F. F.; Song, Z. C.; Ross, P. N.; Somorjai, G. A.; Ritchie, R. O.; Komvopoulos, K., Failure mechanisms of single-crystal silicon electrodes in lithium-ion batteries. *Nat Commun* **2016**, *7*.
14. Carvalho, A.; Rayson, M. J.; Briddon, P. R.; Manzhos, S., Effect of the adsorption of ethylene carbonate on Si surfaces on the Li insertion behavior. *Chem Phys Lett* **2013**, *585*, 157-161.
15. Lin, Y. M.; Klavetter, K. C.; Abel, P. R.; Davy, N. C.; Snider, J. L.; Heller, A.; Mullins, C. B., High performance silicon nanoparticle anode in fluoroethylene carbonate-based electrolyte for Li-ion batteries. *Chem Commun* **2012**, *48* (58), 7268-7270.
16. Etacheri, V.; Haik, O.; Goffer, Y.; Roberts, G. A.; Stefan, I. C.; Fasching, R.; Aurbach, D., Effect of Fluoroethylene Carbonate (FEC) on the Performance and Surface Chemistry of Si-Nanowire Li-Ion Battery Anodes. *Langmuir* **2012**, *28* (1), 965-976.
17. Xu, C.; Lindgren, F.; Philippe, B.; Gorgoi, M.; Bjorefors, F.; Edstrom, K.; Gustafsson, T., Improved Performance of the Silicon Anode for Li-Ion Batteries: Understanding the Surface Modification Mechanism of Fluoroethylene Carbonate as an Effective Electrolyte Additive. *Chemistry of Materials* **2015**, *27* (7), 2591-2599.
18. Aoki, N.; Omachi, A.; Uosaki, K.; Kondo, T., Structural Study of Electrochemically Lithiated Si(111) by using Soft X-ray Emission Spectroscopy Combined with Scanning Electron Microscopy and through

X-ray Diffraction Measurements. *Chemelectrochem* **2016**, 3 (6), 959-965.

19. Lin, H.; Noguchi, H.; Uosaki, K., Application of windowless energy dispersive spectroscopy to determine Li distribution in Li-Si alloys. *Appl Phys Lett* **2018**, 112 (7), 073903.
20. Lyalin, A.; Kuznetsov, V. G.; Nakayama, A.; Abarenkov, I. V.; Tupitsyn, I. I.; Gabis, I. E.; Uosaki, K.; Taketsugu, T., Lithiation of Silicon Anode based on Soft X-ray Emission Spectroscopy: A Theoretical Study. *arXiv preprint arXiv:1801.01983* **2018**.
21. An, Z. L.; Kamezawa, C.; Hirai, M.; Kusaka, M.; Iwami, M., Valence band density of states of Cu₃Si studied by soft X-ray emission spectroscopy and a first-principle molecular orbital calculation. *Journal of the Physical Society of Japan* **2002**, 71 (12), 2948-2952.
22. Eisebitt, S.; Luning, J.; Rubensson, J. E.; Settels, A.; Dederichs, P. H.; Eberhardt, W.; Patitsas, S. N.; Tiedje, T., Resonant inelastic soft X-ray scattering at the Si L-3 edge: experiment and theory. *J Electron Spectrosc* **1998**, 93 (1-3), 245-250.
23. Beaulieu, L. Y.; Hatchard, T. D.; Bonakdarpour, A.; Fleischauer, M. D.; Dahn, J. R., Reaction of Li with Alloy Thin Films Studied by In Situ AFM. *J. Electrochem. Soc.* **2003**, 150 (11), A1457-A1464.
24. Michalak, D. J.; Amy, S. R.; Aureau, D.; Dai, M.; Esteve, A.; Chabal, Y. J., Nanopatterning Si(111) surfaces as a selective surface-chemistry route. *Nat. Mater.* **2010**, 9 (3), 266-271.
25. Bard, A. J.; Faulkner, L. R., *Electrochemical Methods: Fundamentals and Applications*. Wiley: 2000.
26. Yoshida, S.; Masuo, Y.; Shibata, D.; Haruta, M.; Doi, T.; Inaba, M., Adsorbed Water on Nano-Silicon Powder and Its Effects on Charge and Discharge Characteristics as Anode in Lithium-Ion Batteries. *J. Electrochem. Soc.* **2017**, 164 (1), A6084-A6087.
27. Markevich, E.; Salitra, G.; Fridman, K.; Sharabi, R.; Gershinsky, G.; Garsuch, A.; Semrau, G.; Schmidt, M. A.; Aurbach, D., Fluoroethylene Carbonate as an Important Component in Electrolyte Solutions for High-Voltage Lithium Batteries: Role of Surface Chemistry on the Cathode. *Langmuir* **2014**, 30 (25), 7414-7424.

Chapter 6

Solvent effects on Li distribution within Li-Si alloys

6.1 Introduction

The energy capacity and cycle life of the Si anode based secondary batteries are relative to electrolytes. The electrolyte can decompose in the first cycle of Si lithiation to form a layer of poor electron conductivity while good ion conductivity of the surface film when the potential is below 1.3 V vs. Li/Li⁺. This film is well known as the solid electrolyte interface (SEI). SEI can prevent the further decomposition of the electrolyte kinetically. Severe electrolyte decomposition can reduce the energy capacity and cycle life for the Si anode based secondary batteries. First, the continuous expansion and shrinkage of the Si electrode material makes the SEI thicker, decreasing the electrical conductivity of Si electrode and increasing the irreversible capacity.¹⁻² Because of expansion and shrinkage of Si in the charge and discharge process, SEI film can be broken and the surface of Si electrode exposes to the electrolyte again, leading the further electrolyte decomposition to reduce the battery capacity. Second, the volume expansion and shrinkage of Si can cause breakage and pulverization of Si particles, which is particularly more severe for larger Si particles.³ Breakage can cause Si new surfaces and contact the electrolyte, resulting in further electrolyte decomposition and loss of electrical contact between the particles. Generally speaking, it is expected to have better performance for Si anode based secondary battery if the electrolyte is stable for decomposition, or it can form a stable SEI on Si surface.

Electrolytes were considered as a key element that determines the battery characteristics such as the electrochemical reversibility, cycle life, rate capability and columbic efficiency for Li based secondary batteries such as Li ion, Li air or Li-S secondary batteries. For instance, in Li ion secondary batteries, the conventional electrolyte uses Li salt solved in propylene carbonate (PC) or dimethyl carbonate (DMC) as solvent. This electrolyte has enhanced effects on capacity and cycle life of the Li ion secondary batteries. However, the electrolyte using PC or DMC as solvent is highly

unstable in Li-O₂ or Li-S secondary batteries. Dimethyl sulfoxide (DMSO) and tetraethylene glycol dimethyl ether (TEGDME) are reported to have the best stability when they are used in Li-O₂ and Li-S secondary batteries, respectively. Therefore, the electrolyte must be chosen to have the best performance on the battery characteristics for Li based secondary batteries. Especially when considering the solvents, it must be stable or has enhanced effect on battery characteristic like energy capacity and cycle life. The emerging research interest on Li-O₂ and Li-S secondary batteries make Si anode more promising application in these batteries.^{4,7} When Si anode is applied in these secondary batteries to replace Li anode, the solvent effects on Si lithiation must be studied since electrolytes are different for Li-ion, Li-O₂ and Li-S secondary batteries.

In this chapter, the solvent effects on the structures and compositions of the Li-Si alloys were studied by combining SEM, SXES, and windowless EDS analysis. The Li-Si alloys were prepared by using single crystal Si(111) lithiation under potentiostatic charging at 10 mV vs. Li/Li⁺ in 1.0 M LiPF₆ in different solvents. The solvents are DMSO, TMS, EA, TEGDME, DMC, and PC. The lithiation charge density is 1000 mC·cm⁻² for all the Li-Si alloys. The structures are obtained by SEM. The components are analyzed by SXES. The Li K_α, Si L_{2,3} and Si K_α intensity changes were strictly analyzed to obtain the specific thicknesses and Li distribution for the Li-Si alloy layers. The solvent effects were discussed.

6.2 Results and Discussion

6.2.1 Electrochemistry of Si(111) Lithiation in Different Solvents

Figure 6-1 shows the cyclic voltammogram for lithiation and delithiation of single crystal Si(111) electrode measured in 1.0 M LiPF₆ in different solvents. The solvents are DMSO, TMS, EA, TEGDME, DMC, and PC. The potential was scanned negatively from 2.7 to 0.01 V (vs. Li/Li⁺) and positively to 2.7 V (as indicated by arrows) at a scan rate of 1 mV·s⁻¹. The arrows indicated the scan directions.

It had been analyzed for the lithiation and delithiation process of the single crystal Si(111) electrode in 1.0 M LiPF₆ in DMC solvent in section 3.2.1 in Chapter 3. A high cathodic current started to flow at around 100 mV, which corresponds to the lithiation of Si(111). Two broad peaks at around 300 and 500 mV, which correspond to the

delithiation of Si(111) were also clearly observed. The cathodic and anodic charges were approximately 76.6 and 62.5 $\text{mC}\cdot\text{cm}^{-2}$, respectively. The current efficiency, which is ratio of anodic to cathodic charge, is approximately 82%. This efficiency is consistent with other reported values.⁸⁻⁹ The irreversible 20% charge is due to electrolyte decomposition and some Li remaining in the Li-Si alloy after delithiation.

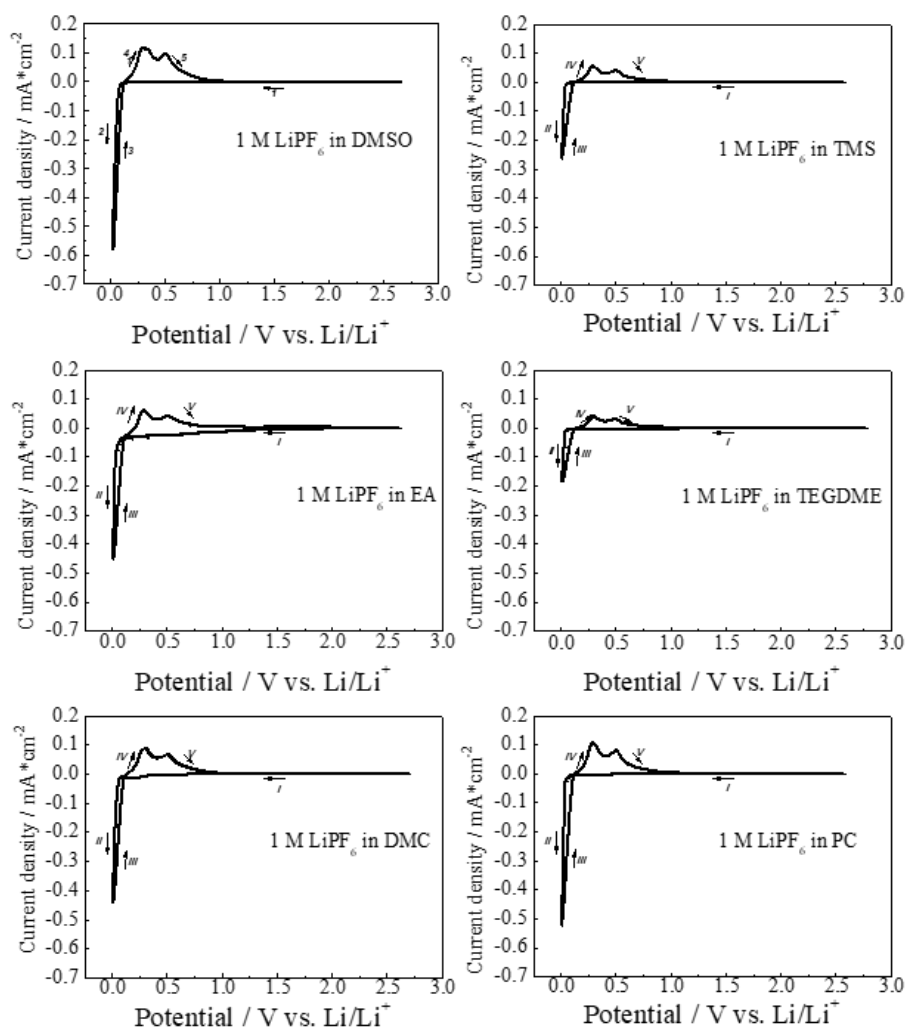


Figure 6-1 Cyclic voltammogram for lithiation and delithiation of single crystal Si(111) electrode measured in 1.0 M LiPF₆ in different solvents. The solvents are DMSO, TMS, EA, TEGDME, DMC, and PC. The potential was scanned negatively from 2.7 to 0.01 V (vs. Li/Li⁺) and positively to 2.7 V at a scan rate of 1 $\text{mV}\cdot\text{s}^{-1}$. The arrows indicated the scan direction.

The lithiation and delithiation process of the single crystal Si(111) electrode in 1.0 M LiPF₆ in other solvents are similar to that in 1.0 M LiPF₆ in DMC solvent. A high

cathodic current started to flow at around 100 mV, which corresponds to the lithiation of Si(111). Two broad peaks at around 300 and 500 mV, which correspond to the delithiation of Si(111) were also clearly observed. However the current are different for Si(111) lithiation in different solvents. This is due to the difference in the Li-Si alloy nuclei formation number density and the Li^+ ion conductivity in the electrolytes. The current efficiency, which is ratio of anodic to cathodic charge, ranges from approximately 80% to 90%. Since some irreversible charge is due to electrolyte decomposition, the difference in this current efficiency should be due to the electrolyte decomposition difference in different solvents.

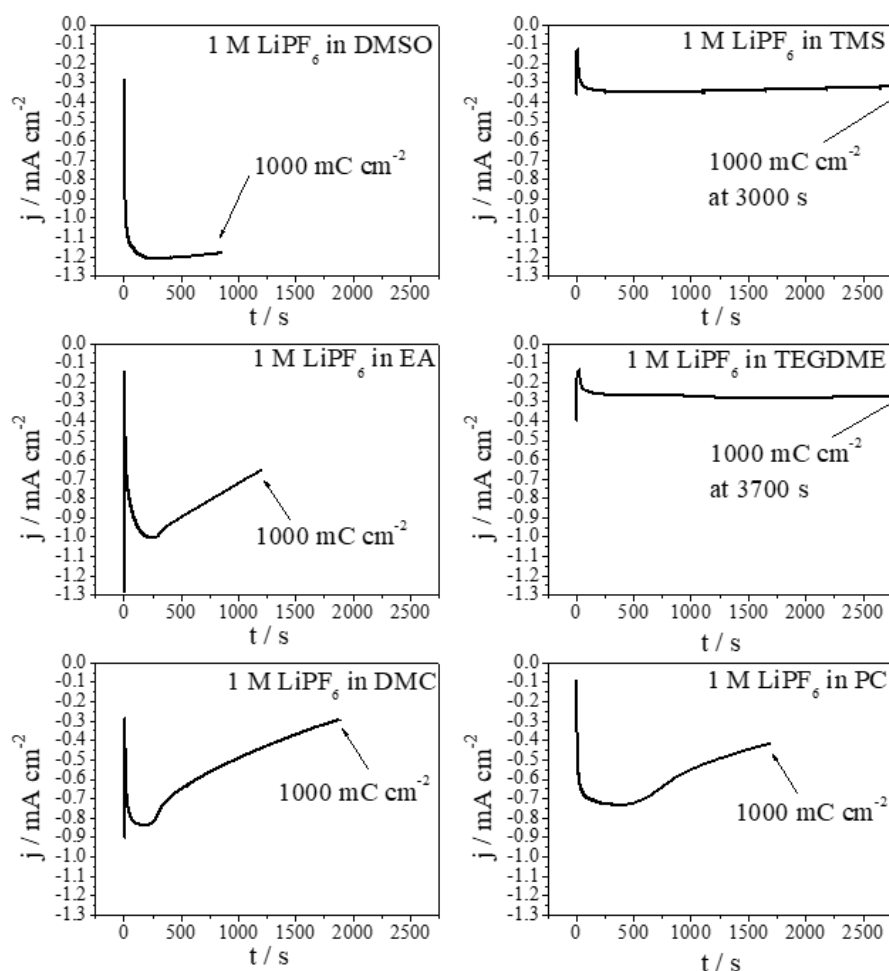


Figure 6-2 Current density as a function of time when the potential was stepped from 500 to 10 mV for Si(111) lithiation in 1.0 M LiPF_6 in different solvents. The solvents are DMSO, TMS, EA, TEGDME, DMC, and PC. The lithiation charge density was 1000 mC cm^{-2} as indicated by arrows.

The Li-Si alloys were prepared under potentiostatic charge at 10 mV. Figure 6-2 shows the current density as a function of time when the potential was stepped from 500 to 10 mV for Si(111) lithiation in 1.0 M LiPF₆ in different solvents. The cathodic current density due to the lithiation of Si increased to a maximum at first, and then decreased gradually to an almost constant value, for all the solvents. The Li-Si alloys were prepared when the lithiation charge was 1000 mC·cm⁻² as indicated by arrows in Figure 6-2. The current maximum is different for different solvents. It is due to the difference in the Li-Si alloy nuclei formation number density and the Li⁺ ion conductivity in the electrolytes, which is also shown in CV results in Figure 6-1. The structures to determine the Li-Si alloy nuclei number density are obtained by SEM and will be discussed in section 6.2.2.

6.2.2 Structures and Compositions of Li-Si alloys Prepared in Different Solvents

Figure 6-3(a-f) shows SEM images of the surface morphology of the Li-Si alloys prepared in 1.0 M LiPF₆ in different solvents. Triangular pyramids exist in all Li-Si alloys and covered the specimen surface. It can be clearly seen that the sizes of pyramid depend on the solvents, and range from approximately 2.0 to 0.1 μm. The pyramid size was counted by measuring single pyramid area as shown in Figure 6-3(a) and shown in Table 6-1. In each Li-Si alloy, at least 100 pyramids were measured. The pyramid size depends on the solvents and ranks as follow: DMSO > TMS > EA > TEGDME > DMC > PC.

Figure 6-3(A-F) shows SEM images of the cross section of the Li-Si alloys prepared in 1.0 M LiPF₆ in different solvents. In Chapter 3, the structure and composition in Li-Si alloy prepared in 1.0 M LiPF₆ in DMC had been analyzed precisely. This layered structure of the Li-Si alloy was also shown here in Figure 6-3(E). The compositions of the Li-Si alloys consist of the 1st crystalline Li₁₅Si₄ layer, the 2nd amorphous Li₁₃Si₄ layer, and the 3rd Li diffused Li_xSi layer. The layered structures were clearly observed for all the Li-Si alloys prepared in different solvents. However, the layer thickness depends on the solvents. The sum thickness of the 1st and 2nd layer can be determined by SEM images and shown in Table 6-1; the sum thicknesses of the 1st with 2nd layer depend on the solvents and vary from approximately 3.0 to 2.0 μm. It ranks as follow: DMSO > TMS > EA > TEGDME > DMC > PC. The thickness of the 3rd layer cannot be obtained because

the 3rd layer cannot be observed clearly by SEM images.

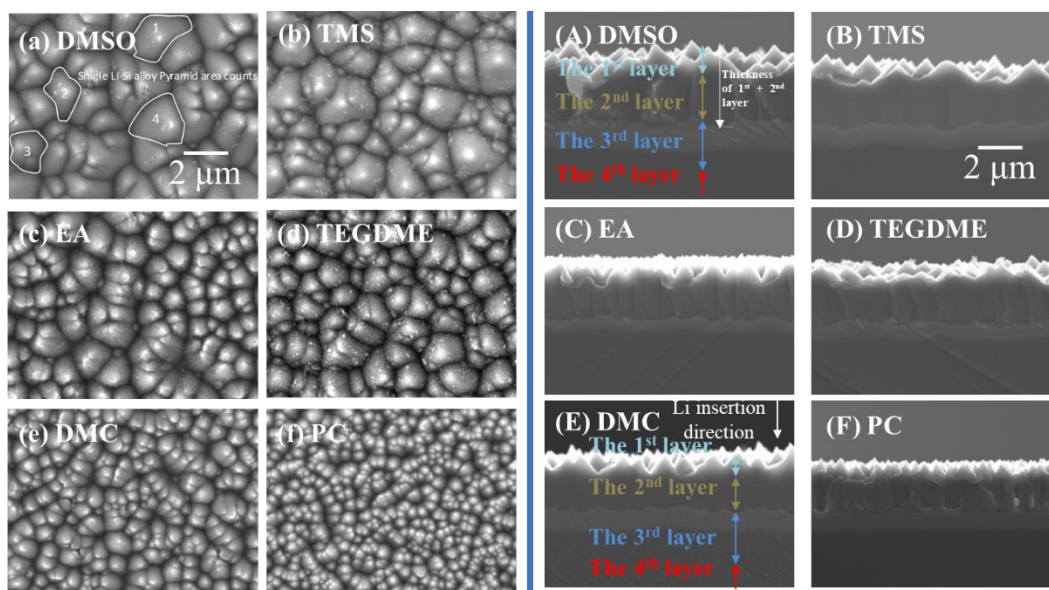


Figure 6-3 SEM images for (a-f) the surface and (A-F) cross section of Li-Si alloys prepared in 1.0 M LiPF₆ in different solvents. The lithiation charge density is 1000 mC·cm⁻² for each Li-Si alloy. The solvents are DMSO (a, A), TMS (b, B), EA (c, C), TEGDME (d, D), DMC (e, E), and PC (f, F). Thickness statistics of the 1st with the 2nd layer for each Li-Si alloy. The layered structures were represented in both (A) and (E), which are the Li-Si alloys prepared in DMSO and DMC, respectively.

Table 6-1 Pyramid size and sum thickness of the 1st and 2nd layer of the Li-Si alloy prepared in different solvents

solvents	DMSO	TMS	EA	TEGDME	DMC	PC
Pyramid size / μm	1.36 \pm 0.15	1.32 \pm 0.13	1.02 \pm 0.09	0.93 \pm 0.08	0.68 \pm 0.05	0.41 \pm 0.05
Thickness of the 1st and 2nd layer / μm	2.97 \pm 0.18	2.71 \pm 0.13	2.47 \pm 0.08	2.42 \pm 0.17	2.34 \pm 0.13	1.98 \pm 0.08

In Chapter 4, it was found when the charge of Si(111) lithiation is 50 mC·cm⁻² in 1.0 M LiPF₆ in DMC solvent, the pyramid is around 0.1 μm and consist of a-Li₁₃Si₄. Then

it will transfer to $c\text{-Li}_{15}\text{Si}_4$ when the pyramid grew to a bigger size. For the Li-Si alloy prepared in FEC in Chapter 5, the Li-Si alloy pyramid in the 1st layer is small to approximately 0.1 μm and also consists of $a\text{-Li}_{13}\text{Si}_4$. It suggests the pyramid was energetically stable to be $a\text{-Li}_{13}\text{Si}_4$ when it is small.

Figure 6-4 show the SXE spectra for the 1st and 2nd layer in the Li-Si alloys prepared in different solvents. The 1st layer for the Li-Si alloys was pyramid layer. The peak position of Si $L_{2,3}$ and Li K_{α} emission for all the Li-Si alloys was 91.8 and 53.3 eV, respectively, which indicate the pyramid layer is $c\text{-Li}_{15}\text{Si}_4$. The 2nd layer for the Li-Si alloys was the layer beneath pyramid layer. The peak position of Si $L_{2,3}$ and Li K_{α} emission was 91.6 eV and 53.6 eV, respectively, which indicate the pyramid layer is $a\text{-Li}_{13}\text{Si}_4$. In summary, all the Li-Si alloys prepared in these different solvents have the same composition, which consists of the 1st layer of $c\text{-Li}_{15}\text{Si}_4$ and 2nd layer $a\text{-Li}_{13}\text{Si}_4$.

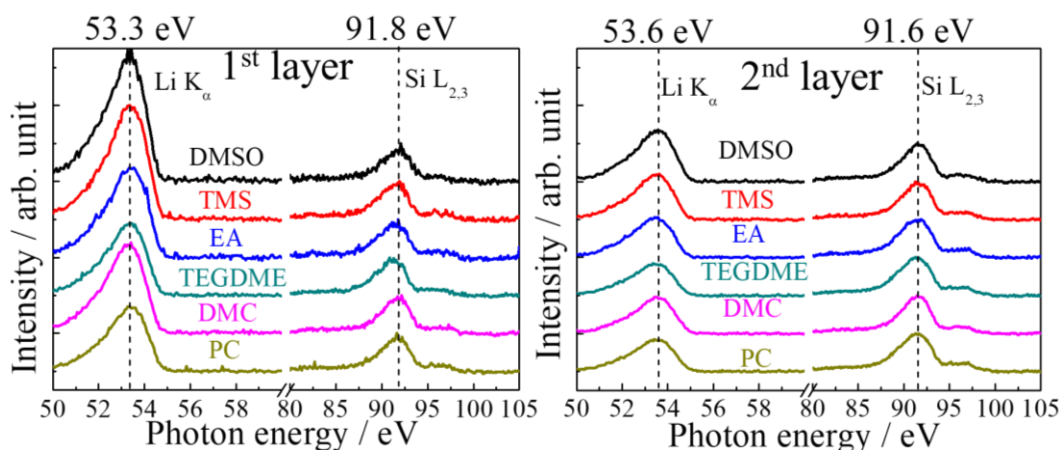


Figure 6-4 SXE spectra for the 1st and 2nd layer in Li-Si alloys prepared in different solvents.

Even though these Li-Si alloys have same compositions, they have different amount ratio of $c\text{-Li}_{15}\text{Si}_4$ and $a\text{-Li}_{13}\text{Si}_4$ alloy phase. To determine the amount (or layer thickness) of $c\text{-Li}_{15}\text{Si}_4$, $a\text{-Li}_{13}\text{Si}_4$ and Li-diffused Li_xSi alloy in the 1st, 2nd and 3rd layer in different Li-Si alloys prepared in different solvents, the EDS line scan were applied to all the Li-Si alloys. The EDS line scan method and its analysis were already presented in Chapter 3. After the EDS spectra deconvolution were conducted, the intensities of Li K_{α} , Si $L_{2,3}$ and Si K_{α} were obtained for all the Li-Si alloys prepared in different solvents.

Figure 6-5a shows the intensity changes of Li K_{α} emissions along the line scan for the Li-Si alloys prepared in different solvents. The intensity changes were similar for all the Li-Si alloys. That is, the Li K_{α} intensity increased with the 1st layer at first, and then decreased from the 1st layer to Si substrate. The Li K_{α} intensity decreased from the 1st layer to Si substrate, consistent with the Li-Si alloy layer structure, i.e., the first crystalline $Li_{15}Si_4$ and the second amorphous $Li_{13}Si_4$ layer, followed by lowly lithiated Si layer over Si substrate. However, the Li K_{α} intensity change in each layer depends on the solvents. The boundaries between the 1st and 2nd layer, the 2nd and 3rd layer, were determined by monitoring the intensity change. Two arrows were used to represent the boundaries in each Li-Si alloy. It can be easily seen the layer boundaries moved to less deep position by the order: DMSO-TMS-EA-TEGDME-DMC-PC. The Li distribution depends on the solvents, that is, less Li remains in the 1st layer when the solvents changed from DMSO to PC. Figure 6-5b shows the intensity changes of Si K_{α} emissions along the line scan for the Li-Si alloys prepared in different solvents. The intensity changes were similar for all the Li-Si alloys. The Si K_{α} intensity increased from the 1st layer to Si substrate. The arrow was used to represent the boundaries in each Li-Si alloy. It can also be easily seen the layer boundaries moved to less deep position by the order: DMSO-TMS-EA-TEGDME-DMC-PC. This order is consistent with the observation in Li K_{α} intensity change.

In Chapter 3, the Li distribution in the 3rd layer of the Li-Si alloy prepared in 1.0 M in DMC can be known by monitoring the Si $L_{2,3}$ intensity change, because the Li K_{α} intensities are too low to distinguish its intensity changes. The 3rd layer is found to be Li diffused Li_xSi layer. The thickness of each layer can be precisely determined by monitoring the Si $L_{2,3}$ intensity change. Figure 6-5c shows the intensity changes of Si $L_{2,3}$ along the line scan for the Li-Si alloys prepared in different solvents. For all the Li-Si alloys, the intensity changes of Si $L_{2,3}$ show similar behavior. The Li distribution had been precisely determined, in which, the Li concentration decrease from the 1st layer to Si substrate, and the Li concentration decrease within the 3rd layer like a Li diffusion layer. The thicknesses of each layer can be easily determined and shown in Figure 6-5(d). The thickness of the 1st layer depends on the solvents and decreased by the

following order: DMSO-TMS-EA-TEGDME-DMC-PC. The thickness of the 3rd layer is almost the same for all the Li-Si alloys. The thickness of each layer can be used to calculate how much charge needed for the layer growth shown in Figure 6-5(e). Less charge was used to grow the 1st layer when the solvent changed from DMSO to PC. It suggested less amount of c-Li₁₅Si₄ formed in the 1st layer.

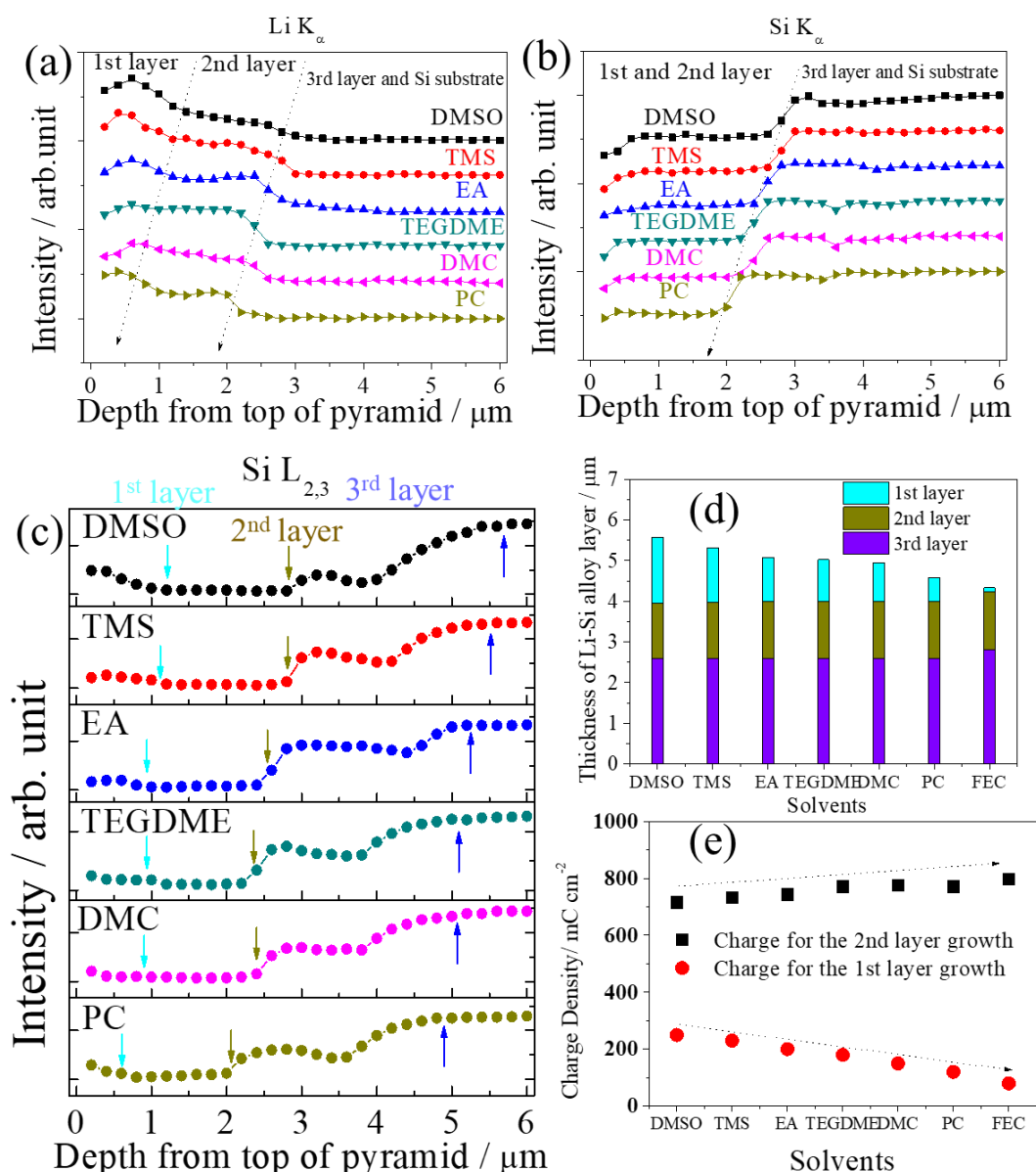


Figure 6-5 Intensity changes of (a) Li K_α, (b) Si K_α and (c) Si L_{2,3} emissions along the line scan for the Li-Si alloys prepared in different solvents. The boundaries between the 1st and 2nd layer, the 2nd and 3rd layer, were determined by monitoring the intensity change. (d) The thicknesses of each layer for different Li-Si alloys determined from Figure 6-5(c). (e) The charge that is used for the 1st and 2nd layer growth in different Li-

Si alloys.

6.2.3 Discussion on the Factors of Solvents that Affect Si(111) lithiation

To make clear what is the main factor that the solvents affect the structures and compositions of the Li-Si alloy, we did galvanostatic and potentiostatic lithiation, which will determine if the current or potential is the main factor. Figure 6-6 and 6-7 show the SEM images of the Li-Si alloy galvanostatic charged in different solvents at -100 and -400 $\mu\text{A}\cdot\text{cm}^{-2}$. The currents are chosen according to the maximum cathodic currents in different solvents ranging from -100 to -500 $\mu\text{A}\cdot\text{cm}^{-2}$ in Figure 6-1. If the current was the only main factor that affect the pyramid size, the pyramid size must be the same under the same current in different solvents. However, Figure 6-6 and 6-7 had shown that even though the lithiation current was the same, the structures (pyramid size) were different in different solvents. Under the same galvanostatic current, the structures (pyramid size) still depend on the solvents. There must be more essential factor than the lithiation current for the solvents that affect the structures of the Li-Si alloys.

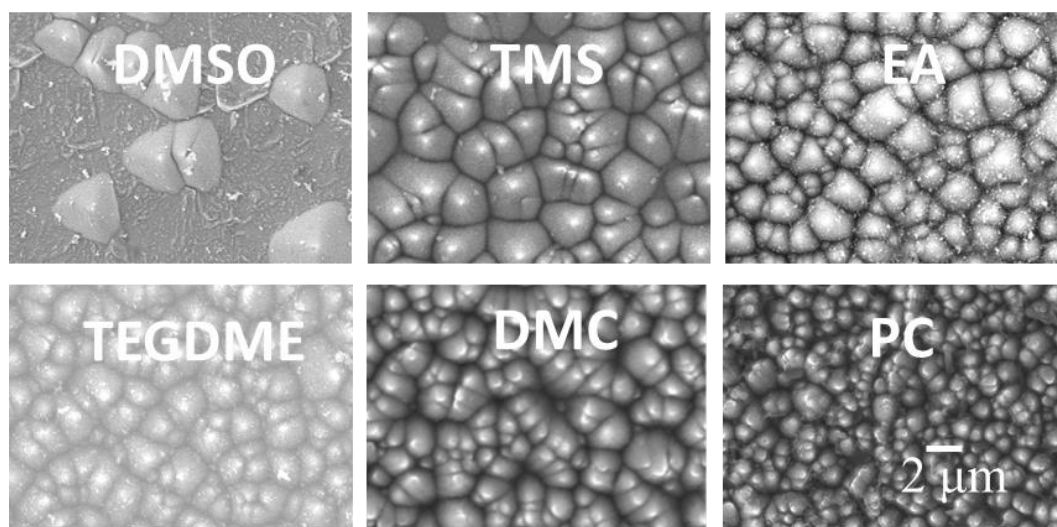


Figure 6-6 SEM images of the surface of Li-Si alloys galvanostatic prepared in 1.0 M LiPF_6 in different solvents. The lithiation current was $-100 \mu\text{A}\cdot\text{cm}^{-2}$.

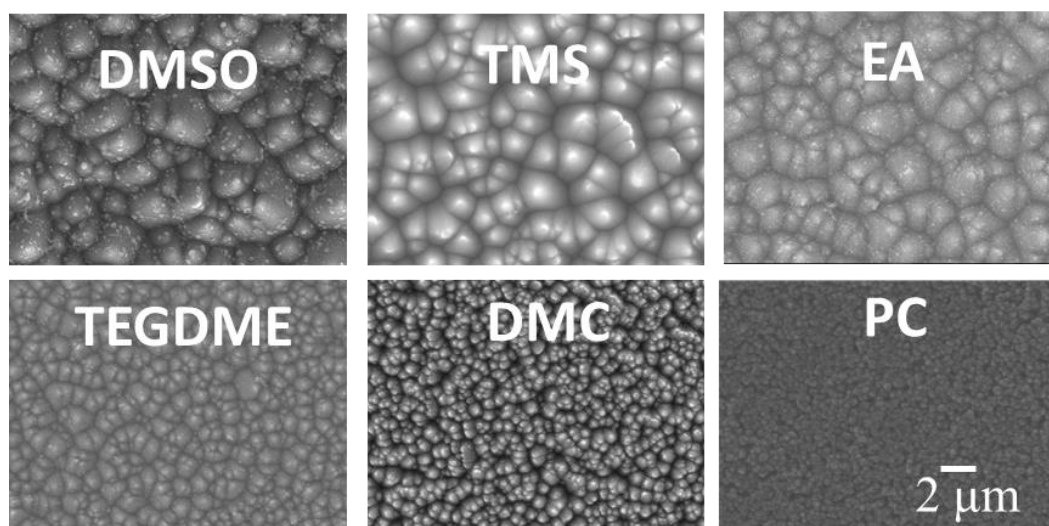


Figure 6-7 SEM images for the surface of Li-Si alloys galvanostatic prepared in 1.0 M LiPF_6 in different solvents. The lithiation current was $-400 \mu\text{A}\cdot\text{cm}^{-2}$

In chapter 4, we had clarified that the structures of the Li-Si alloys can be affected by the potential (10, 30, 50 and 70 mV vs Li/Li^+) in the same solvent. The pyramid nuclei number density is decided by the potential (overpotential). The potentiostatic lithiation under different potential was also conducted in different solvent as shown in Figure 6-8. As is observed, the pyramid number density is decided by the potential and the solvents. From Figure 6-3 and 6-8, the effects of the solvent on the Li-Si pyramid structure (Li-Si alloy pyramid nuclei number density) can be summarized as follow: first, the pyramid nuclei number density N_0 increases when the potential goes more negative ($70 \rightarrow 50 \rightarrow 30 \rightarrow 10$ mV) in the same solvent; second, the pyramid nuclei number density N_0 increases when the solvent changes by the solvent order (DMSO \rightarrow TMS \rightarrow EA \rightarrow TEGDME \rightarrow DMC \rightarrow PC).

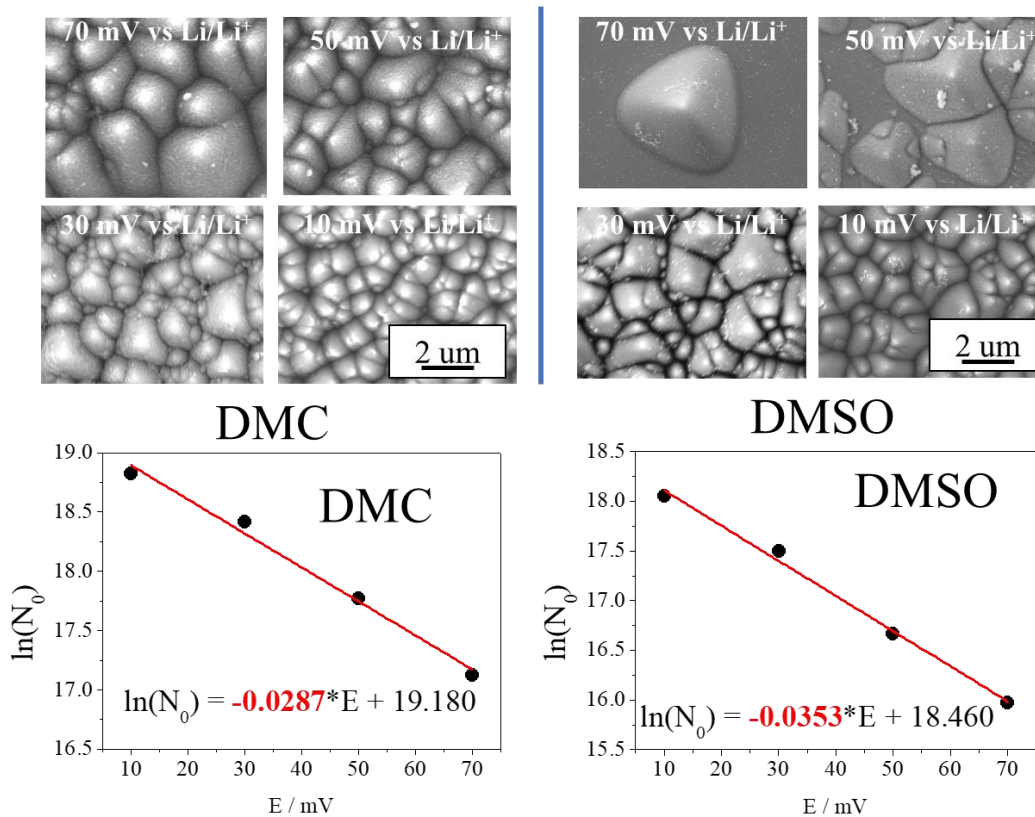
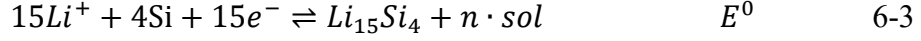
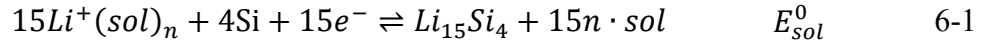


Figure 6-8 SEM images of the Li-Si alloys potentiostatic prepared at 70, 50, 30 and 10 mV in DMC and DMSO. The relationship of nuclei number density with the applied potential are also shown for both solvents.

To explain the relationship between pyramid nuclei number density N_0 and the potential and the solvent, it need to know and analyze the electrochemical reaction that happen on the Si surface. The Li-Si alloy composition on the surface had been determined as c-Li₁₅Si₄ in Chapter 3. Reaction 6-1 show the electrochemical reaction of solvated Li ion with Si to form Li₁₅Si₄. Here, E_{sol}^0 is the equilibrium potential which is relative to the solvents. As is known, Li ion remains in the electrolyte as solvated ion $Li^+(sol)_n$ (sol is the solvent molecule, n is the number of coordinating molecule). Before it alloys with Si, the solvated Li ion needs to desolvate as shown in reaction 6-2, in which, K_{desol} is the desolvation constant defined as $K_{desol} = ([Li^+] \cdot [sol]^n / [Li^+(sol)_n])^{15}$. $[Li^+]$, $[sol]$ and $[Li^+(sol)_n]$ are the concentrations of the free Li ion, the solvent and the solvated Li ion, respectively. After the solvated Li ion desolvate as reaction 6-2, it will react with Si to form Li₁₅Si₄ as shown in reaction 6-3, in which, E^0 is the equilibrium potential which is independent on the solvents.



The sum of reaction 6-2 and 6-3 will result in reaction 6-1. The relationship between E_{sol}^0 , K_{desol} and E^0 can be obtained and shown in equation 6-4,

$$E_{sol}^0 = E^0 + \frac{RT}{F} \ln K_{desol} \quad 6-4.$$

The equilibrium potential E_{sol}^0 in different solvents is a function of the desolvation constant K_{desol} . The nuclei number density N_0 is a function of overpotential η and can be almost linear to $\exp(\eta F/RT)$ and shown in equation 6-5,¹⁰⁻¹¹

$$N_0 \propto \exp\left(\frac{\eta F}{RT}\right) = \exp\left(\frac{(E_{sol}^0 - E)F}{RT}\right) = \exp\left(-\frac{EF}{RT}\right) \cdot \exp\left(\frac{E_{sol}^0 F}{RT}\right) \quad 6-5,$$

where E is the applied potential, E_{sol}^0 is the equilibrium potential in reaction 6-1, R and T are the gas constant and ambient temperature. Bring the equation 6-4 into 6-5 and the following equation 6-6 can be obtained,

$$N_0 \propto \exp\left(\frac{E_{sol}^0 F}{RT}\right) \cdot \exp\left(-\frac{EF}{RT}\right) \cdot K_{desol} \quad 6-6.$$

Based on equation 6-6, we can explain the experimental results, that is, the nuclei number density N_0 (or the pyramid size) is affected by the applied potential E (10, 30, 50, 70 mV vs Li/Li⁺) and the solvent K_{desol} (DMSO, TMS, EA, TEGDME, PC, DMC).

First, $\exp\left(\frac{E_{sol}^0 F}{RT}\right)$ in equation 6-6 is a constant, because E^0 is independent on the solvents according to equation 6-3. N_0 can be only affected by E and K_{desol} , which are relative to the applied potential and the solvents, respectively.

Second, $\exp\left(-\frac{EF}{RT}\right)$ is a function of the applied potential E . In the same solvent, K_{desol} is fixed. Therefore, more negative potential (70 \rightarrow 10 mV) resulted in more N_0 nuclei formation and smaller pyramid. There is a linear relationship between $\ln N_0$ and

E , which had been obtained and shown in Figure 4-10 and Figure 6-8 and was consistent with the experimental results. The curve slope of $\ln N_0$ and E is $-F/RT$, which has a constant value of -0.0389 mV^{-1} . This suggest the slope is independent on the solvents. In Figure 6-8, the slope of $\ln N_0$ and E is -0.0287 and -0.0353 mV^{-1} in DMC and DMSO were close to the theoretical value -0.0389 mV^{-1} .

Third, for the same applied potential E , the nuclei number density N_0 is a function of desolvation constant K_{desol} . It is expected larger K_{desol} will resulted in more N_0 nuclei formation. In other words, if the solvated Li ion is easier to desolvate, more N_0 nuclei will form. To explain the solvent dependent nuclei formation, we need to compare K_{desol} among the different solvents. However, it is difficult to obtain the specific value of K_{desol} for all the different solvents. To obtain the value, the first principle calculation can be used to calculate the specific value, but it will take very long time for all the solvents. According to the equation that define the desolvation constant $K_{desol} = ([Li^+] \cdot [sol]^n / [Li^+(sol)_n])^{15}$, K_{desol} is function the concentration $[Li^+(sol)_n]$ of the solvated Li ion, here, the sum of $[Li^+]$ and $[Li^+(sol)_n]$ is 1 M. If the value of $[Li^+(sol)_n]$ can be obtained or compared for different solvent, it can be quantitatively or qualitatively used to analyze the nuclei number density. Raman spectroscopy can detect the vibration mode of the solvent molecule from $Li^+(sol)_n$. This inspires us to use Raman spectroscopy to qualitatively compare K_{desol} or $[Li^+(sol)_n]$ in different solvents.¹²

It need to be mentioned at first that there are two kinds of organic solvent molecule in Li salt containing electrolytes: one is free solvent molecule without solvating Li^+ ion; another is solvating solvent molecule to Li^+ ion $Li^+(sol)_n$. The amount of free and solvating solvent molecule in the electrolyte depend on the solvent properties. It has no meaning to compare K_{desol} or $[Li^+(sol)_n]$ by directly compare the Raman intensity of the solvated Li ion $[Li^+(sol)_n]$ in different solvents, because the vibration mode in different solvents is different. An indicator solvent is needed to realize this compare by selecting one same vibration mode (such as stretching mode of DMSO molecule), and other solvent was added into this indicator solvent to see how $[Li^+(DMSO)_n]$ will change. For example, it is expected the solvating molecule $Li^+(DMSO)_n$ will increase

if another easier-to-desolvate (large K_{desol}) solvent is added, because the Li^+ ion will be extracted for the easier-to-desolvate solvent to solvated by free DMSO. Based on this rule, we can compare the desolvation constant K_{desol} for the different solvents. According to Raman intensity, we can compare the ratio change of solvating to free solvent molecule amounts $[\text{Li}^+(\text{DMSO})_n]/[\text{DMSO}]$ after adding other solvents into DMSO, and then qualitatively compare the desolvation constant K_{desol} .

Figure 6-9(a) shows the Raman spectra of DMSO solvent and the electrolyte of 1 M LiPF_6 in DMSO. The Raman shift ranges from 640 to 760 cm^{-1} . The Raman shift peak of the C-S symmetric and asymmetric stretching modes of the free and solvating DMSO are observed. Two bands at 667 and 697 cm^{-1} were assigned to the C-S symmetric and asymmetric stretching modes of the free DMSO. Two band at 676 and 708 cm^{-1} were assigned to the C-S symmetric and asymmetric stretching modes of the electrolyte of 1 M LiPF_6 in DMSO. Figure 6-9(b) shows the Raman spectra of the electrolytes of 1 M LiPF_6 in EA, TMS, TEGDME, and DMC. Since these spectra show no peaks or limited peaks in this Raman shift range, the application of the intensity ratio of free DMSO and solvating DMSO was convenient. As explained above, the intensity ratio of free DMSO and solvating DMSO will be used as qualitative parameter to compare the desolvation ability K_{desol} of the solvents or the concentration $[\text{Li}^+(\text{sol})_n]$ of the solvated Li ion.

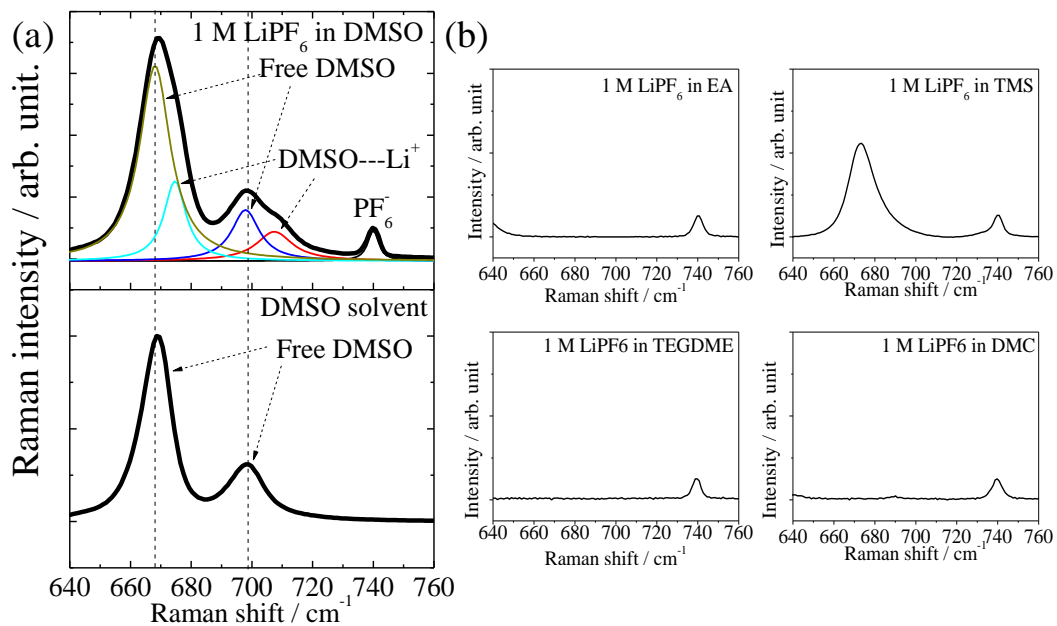


Figure 6-9 (a) Raman spectra of the electrolyte of 1 M LiPF₆ in DMSO, and DMSO solvent. The Raman shift range from 640 to 760 cm⁻¹, in which the Raman shift of the C-S symmetric and asymmetric stretching modes of the free and solvating DMSO are shown. (b) Raman spectra of the electrolytes of 1 M LiPF₆ in EA, TMS, TEGDME, and DMC. These spectra show no peaks or limited peaks in this Raman shift range from 640 to 760 cm⁻¹.

Figure 6-10(a) shows the Raman spectra of the electrolyte of 1 M LiPF₆ in DMSO mixed with equal volume of other solvents. The Raman shift range from 640 to 760 cm⁻¹. The solvents are TMS, EA, TEGDME, DMC, and PC. The intensity ratio of Raman peaks at 697 and 708 cm⁻¹ are obtained to determine the concentration of the solvated Li⁺ ion [Li⁺(sol)_n]. The principle was shown in Figure 6-10(b). In the electrolyte of 1 M LiPF₆ in DMSO mixed with equal volume of other solvents, free DMSO is able to attract solvated Li⁺ ion by the mixed solvents and replace the other solvent to transfer to a solvating DMSO. Therefore, the number of solvating DMSO will increase if the mixed solvents is easier to desolvate (or larger K_{desol}), in other words, the Raman peak ratio of solvating DMSO to free DMSO will increase. The Raman peak ratio of solvating DMSO to free DMSO is a qualitative number to represent the K_{desol} for different solvents.

Figure 6-10(c) shows this intensity ratio after deconvolution in Figure 6-10(a). It can be easily seen the ratio nearly increase by the solvents order: DMSO-TMS-EA-TEGDME-DMC-PC. It suggests K_{desol} increase by the solvent order: DMSO-TMS-EA-TEGDME-DMC-PC. Now according to the Raman intensity ratio compare, it is able to compare the K_{desol} for different solvents like Figure 6-10(c) shows.

Because $N_0 \propto K_{desol}$ and $K_{desol} = ([Li^+] \cdot [sol]^n / [Li^+(sol)_n])^{15} \propto I^{15}$ at the same applied potential, the following relationship $N_0 \propto I^{15}$ can be obtained. Here, the pyramid nuclei number density N_0 can be obtained from Figure 6-3 (the same applied potential is 10 mV) and the Raman intensity ratio I is shown in Figure 6-10(c). The relationship between N_0 and I^{15} is plotted in Figure 6-10(d). It can be fitted as nearly linear relationship as discussed. Therefore, the solvent dependence was explained.

In short summary, according to the equation $N_0 \propto \exp(\frac{E^0 F}{RT}) \cdot \exp(-\frac{EF}{RT}) \cdot K_{desol}$, it

can explain the experimental results, in which, the pyramid nuclei number density increases (pyramid size decreases) when the applied potential E goes negative ($70 \rightarrow 10$ mV); the pyramid nuclei number density increases (pyramid size decreases) when the solvent is easier to desolvate the solvated Li ion (larger K_{desol}).

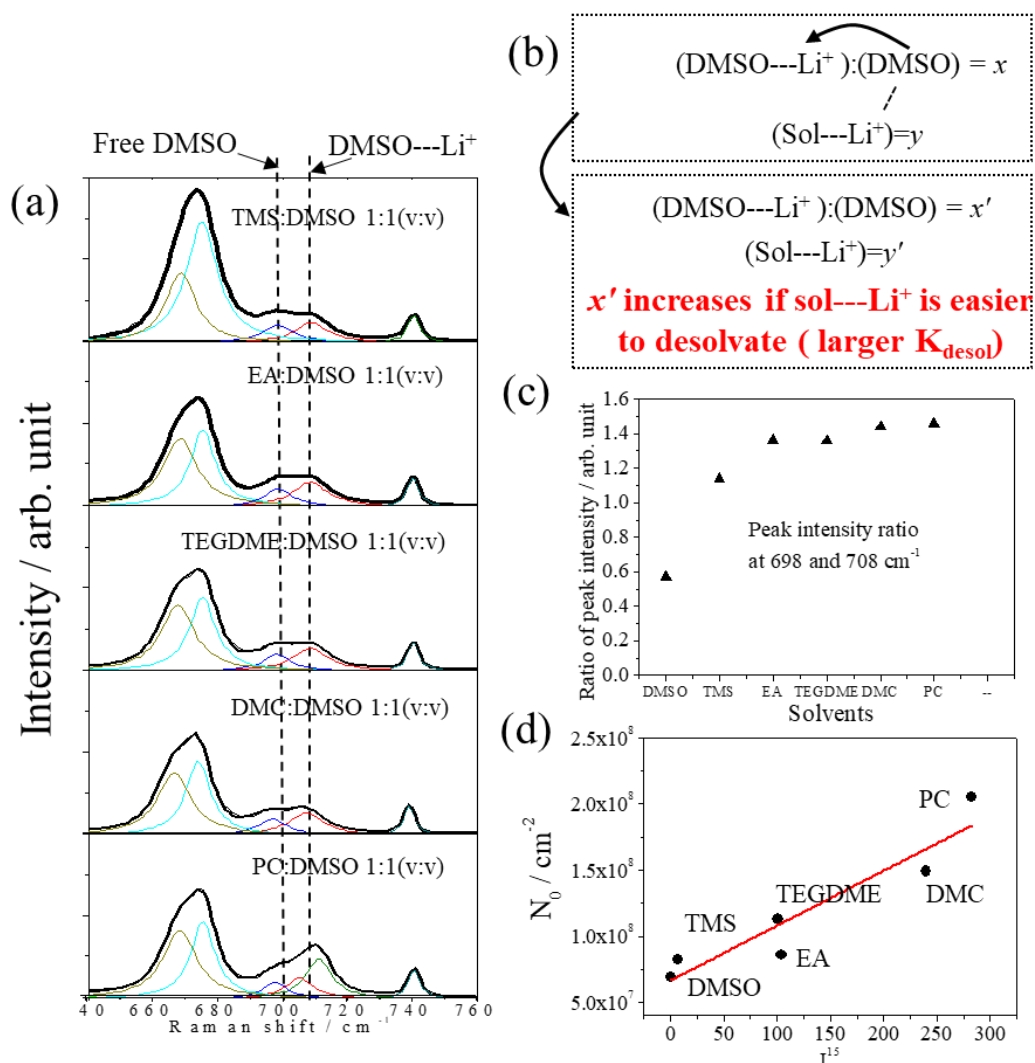


Figure 6-10 (a) Raman spectra of the electrolyte of 1 M LiPF₆ in DMSO mixed with equal volume of other solvents. The Raman shift range from 640 to 760 cm⁻¹. The solvents are TMS, EA, TEGDME, DMC, and PC. The intensity ratio of Raman peaks at 697 and 708 cm⁻¹ are used to determine the solvation strength of the solvents to Li⁺ ion. (b) Schematic to show the principle of the intensity ratio to determine the desolvation ability of the solvents to Li⁺ ion. (c) The intensity ratio of Raman peaks at 697 and 708 cm⁻¹ for the electrolyte of 1 M LiPF₆ in DMSO mixed with equal volume of other solvents. (d) The relationship between the pyramid nuclei number density

N_0 and the 15 power of the raman intensity ratio I^{15} . The number density N_0 was obtained from Figure 6-1, and the Raman intensity ratio I was obtained from Figure 6-10(c).

6.3 Conclusions

In this chapter, windowless EDS was used to study the Li distribution within the Li-Si alloys prepared in different solvents. The structures and components of the Li-Si alloys prepared in different solvents were studied by SEM and SXES, respectively. The lithiation charge density is $1000 \text{ mC}\cdot\text{cm}^{-2}$ for all the Li-Si alloys. The solvents are DMSO, TMS, TEGDEM, EA, DMC, and PC. The solvent effects on Si lithiation are determined and discussed.

It was found that the structure and composition of the Li-Si alloys depend on the solvents. When the solvents are changed, the thickness of the 1st c-Li₁₅Si₄ alloy layer decreased in the solvent order DMSO > TMS > EA > TEGDME > DMC > PC. However, the 2nd a-Li₁₃Si₄ alloy layer increased. It was also found the 3rd Li diffused Li_xSi alloy layer were independent on the solvents. According to the equation $N_0 \propto \exp\left(\frac{E^0F}{RT}\right) \cdot \exp\left(-\frac{EF}{RT}\right) \cdot K_{desol}$, the pyramid nuclei number density increases (pyramid size decreases) when the applied potential E goes negative ($70 \rightarrow 10 \text{ mV}$); the pyramid nuclei number density increases (pyramid size decreases) when the solvent is easier to desolvate the solvated Li ion (larger K_{desol} , DMSO \rightarrow TMS \rightarrow EA \rightarrow TEGDME \rightarrow DMC \rightarrow PC). The desolvation ability of the solvents to Li ion played a significant role on the nucleation of the alloy pyramid.

Reference

1. Nie, M. Y.; Abraham, D. P.; Chen, Y. J.; Bose, A.; Lucht, B. L., Silicon Solid Electrolyte Interphase (SEI) of Lithium Ion Battery Characterized by Microscopy and Spectroscopy. *J. Phys. Chem. C* **2013**, *117* (26), 13403-13412.
2. Ruffo, R.; Hong, S. S.; Chan, C. K.; Huggins, R. A.; Cui, Y., Impedance Analysis of Silicon Nanowire Lithium Ion Battery Anodes. *J. Phys. Chem. C* **2009**, *113* (26), 11390-11398.
3. Liu, X. H.; Zhong, L.; Huang, S.; Mao, S. X.; Zhu, T.; Huang, J. Y., Size-Dependent Fracture of Silicon Nanoparticles During Lithiation. *Acs Nano* **2012**, *6* (2), 1522-1531.
4. Yang, Y.; McDowell, M. T.; Jackson, A.; Cha, J. J.; Hong, S. S.; Cui, Y., New Nanostructured Li₂S/Silicon Rechargeable Battery with High Specific Energy. *Nano Lett* **2010**, *10* (4), 1486-1491.
5. Hassoun, J.; Jung, H. G.; Lee, D. J.; Park, J. B.; Amine, K.; Sun, Y. K.; Scrosati, B., A Metal-Free, Lithium-Ion Oxygen Battery: A Step Forward to Safety in Lithium-Air Batteries. *Nano Lett* **2012**, *12* (11), 5775-5779.
6. Elazari, R.; Salitra, G.; Gershinshy, G.; Garsuch, A.; Panchenko, A.; Aurbach, D., Rechargeable lithiated silicon-sulfur (SLS) battery prototypes. *Electrochem Commun* **2012**, *14* (1), 21-24.
7. Hassoun, J.; Kim, J.; Lee, D. J.; Jung, H. G.; Lee, S. M.; Sun, Y. K.; Scrosati, B., A contribution to the progress of high energy batteries: A metal-free, lithium-ion, silicon-sulfur battery. *J Power Sources* **2012**, *202*, 308-313.
8. Chan, C. K.; Peng, H.; Liu, G.; Mcllwraith, K.; Zhang, X. F.; Huggins, R. A.; Cui, Y., High-performance lithium battery anodes using silicon nanowires. *Nature Nanotechnology* **2008**, *3* (1), 31-35.
9. Holzapfel, M.; Buqa, H.; Hardwick, L. J.; Hahn, M.; Wuersig, A.; Scheifele, W.; Novak, P.; Koetz, R.; Veit, C.; Petrat, F.-M., Nano silicon for lithium-ion batteries. *Electrochim Acta* **2006**, *52* (3), 973-978.
10. Mostany, J.; Mozota, J.; Scharifker, B. R., 3-DIMENSIONAL NUCLEATION WITH DIFFUSION CONTROLLED GROWTH .2. THE NUCLEATION OF LEAD ON VITREOUS CARBON. *J Electroanal Chem* **1984**, *177* (1-2), 25-37.
11. Mostany, J.; Parra, J.; Scharifker, B. R., THE NUCLEATION OF LEAD FROM HALIDE-CONTAINING SOLUTIONS. *J Appl Electrochem* **1986**, *16* (3), 333-338.
12. Yamada, Y.; Takazawa, Y.; Miyazaki, K.; Abe, T., Electrochemical Lithium Intercalation into Graphite in Dimethyl Sulfoxide-Based Electrolytes: Effect of Solvation Structure of Lithium Ion. *J. Phys. Chem. C* **2010**, *114* (26), 11680-11685.

Chapter 7

General Conclusion and Future Prospects

7.1 General Conclusion

In the present thesis, SEM, SXES and windowless EDS were mainly used to determine the structures, compositions and Li distribution in the Li-Si alloys that were electrochemically prepared in organic solvents. The ion adsorption and solvent effects on the structures, compositions and Li distribution in the Li-Si alloys were comprehensively studied.

In chapter 3, windowless EDS was used to study the Li distribution within the Li-Si alloys prepared in 1.0 M LiPF₆ in DMC solvent combined with SXES. The lithiation charge density was 1000 mC·cm⁻² for the Li-Si alloys. The emission intensities of Li K_α and Si L_{2,3} of EDS spectra were obtained after deconvolution of the spectra. By monitoring the Li K_α, Si L_{2,3} and Si K_α emission intensity changes in windowless EDS spectra, the Li distribution in the Li-Si alloys were obtained. The Li concentrations in the Li-Si alloys determined by windowless EDS were consistent with the determined composition by SEXE, which revealed the 1st c-Li₁₅Si₄ layer, the 2nd a-Li₁₃Si₄ layer, and the 3rd lowly lithiated Li_xSi layer. In addition, the Li diffusion profile in the 3rd Li_xSi alloy layer was determined by monitoring the Si L_{2,3} intensity change of windowless EDS spectra. The thickness of each Li-Si layer could be also determined, especially for the 3rd layer which cannot be observed clearly by SEM.

In chapter 4, five Li-Si alloys were electrochemically prepared under potentiostatic charging at 10 mV vs. Li/Li⁺ in 1.0 LiPF₆ in DMC. The lithiation charge densities for the five Li-Si alloys were 20, 50, 120, 500 and 1000 mC·cm⁻². The structures and compositions of the five Li-Si alloys were investigated by using SEM, SXES and windowless EDS to study the single crystal Si(111) lithiation process. Under potentiostatic charging, the cathodic current density due to lithiation increased to a maximum value of -720 μA·cm⁻², and then decreased gradually to a constant value. SXES revealed that pyramid formed a-Li₁₃Si₄ phase at the initial lithiation, which then

transformed into c-Li₁₅Si₄ phase. SEM measurements had revealed the c-Li₁₅Si₄ alloy layer grew along with the Li diffused Li_xSi alloy layer until the lithiation current reached its maximum value. Then the a-Li₁₃Si₄ alloy layer began to grow after the lithiation current reached its maximum value. Windowless EDS determined the Li distribution change in each layer for the five Li-Si alloys. It was found Li distribution in the 3rd layer would not change after the lithiation current reached its maximum value. The thickness changes can be determined by monitoring the Li K_α, Si L_{2,3} and Si K_α intensity change for the five Li-Si alloys. In situ synchrotron XRD measurements had revealed the c-Li₁₅Si₄ formation and dissolution during the Si lithiation and delithiation. By studying the current as a function of time under different potential, the Si(111) lithiation process was clarified to be a diffusion controlled electrochemical process.

In Chapter 5, the effects of FEC and HF on the structures and compositions of the Li-Si alloys were studied. The HF were found to be adsorbed on the Si surface. F⁻ adsorption made the surface potential more negative and was expected to increase the Li⁺ ion concentration on the surface, resulting in more pyramid nuclei formation on the surface. More pyramid nuclei formation resulted in smaller pyramid that covered the Si surface, i.e., thinner crystalline Li₁₅Si₄ alloy layer. This explained the reason of FEC to improve the battery performance, since FEC can decompose to generate large amount of HF which can make the pyramid smaller.

In chapter 6, the effects of the solvents on the structures and compositions of the Li-Si alloys prepared therein were studied. It was found that the structures and compositions of the Li-Si alloys depend on the solvents. When the solvents are changed, the thickness of the 1st c-Li₁₅Si₄ alloy layer decreased in the solvent order DMSO > TMS > EA > TEGDME > DMC > PC. However, the 2nd a-Li₁₃Si₄ alloy layer increased. It was found the 3rd Li diffused Li_xSi alloy layer were independent on the solvents. Here it was considered the solvation strength of the solvents to Li⁺ ion played a significant role to change the nucleation overpotential η which can affect the pyramid nuclei number density N_0 . Weaker solvation strength to Li⁺ ion made Li⁺ ion easier to dissolve to alloy with Si, which resulted in more Li-Si pyramid nucleus formation under bigger overpotential η . More pyramid nucleus resulted in smaller pyramid. Therefore, the

structure and compositions of the Li-Si alloys changed when the solvents were changed and it determined that PC solvent can be the best solvent in which the Li-Si alloy has the least amount of c-Li₁₅Si₄

In this thesis, windowless EDS has been proved to be a strong technique for characterizing the Li distribution within the Li-Si alloys combined with SXES. It was used to study the single crystal Si lithiation process. It was also used to study the solvent effects on the Li distribution in the Li-Si alloys. Monitoring the Si L_{2,3} intensity change provided the Li concentration profile within the Li-Si alloys.

7.2 Future Prospects

In the present thesis, the studies focus on the lithiation of single crystal, which is not popular for practical use. The Si powder is popular to be used in practical batteries. Therefore, it is important to study and make clear the electrolyte addition and solvent effects on the structures and compositions of the Si powder in practical batteries in the future, such as the reason that why FEC can improve the battery performance.